

Heterogeneous catalyzed Copolymerization of Propylene Oxide and Carbon Dioxide

Process Control and Rheological Characterization

Doctoral Thesis

With the aim of achieving a doctoral degree

At the Faculty of Mathematics, Informatics and Natural Sciences

Department of Chemistry

University of Hamburg

Submitted by

Jakob Marbach

Hamburg, January 2020

The present thesis was prepared at the Institute of Technical and Macromolecular Chemistry of the University of Hamburg in the research group of Professor Dr. Gerrit A. Luinstra from January 2015 to August 2018 and at the University of British Columbia in the research group of Professor Parisa Mehrkhodavandi between March and August 2017.

Date of thesis defense: 06.12.2019

The following referees recommend the acceptance of this doctoral thesis:

1st referee: Professor Dr. Gerrit A. Luinstra

2nd referee: Privatdozent Dr. Christoph Wutz

LIST OF PUBLICATIONS

Original articles

1. J. Marbach, B. Nörnberg, A. F. Rahlf and G. A. Luinstra, *Zinc glutarate-mediated copolymerization of CO₂ and PO – parameter studies using design of experiments*, *Catal. Sci. Technol.*, **2017**, 7, 2897 – 2905.
2. J. Marbach, Th. Höfer, N. Bornholdt, G. A. Luinstra, *Catalytic Chain Transfer Copolymerization of Propylene Oxide and CO₂ using Zinc Glutarate Catalyst*, *ChemistryOpen*, **2019**, 8, 1-13.

Conference talks

3. J. Marbach, B. Szostak, B. Nörnberg, G. A. Luinstra, *Towards large scale applications of poly(propylene carbonate) – Process optimization and enhancement of thermal stability*, 12th International Workshop on Polymer Reaction Engineering, **17. – 20.05.2016**, Hamburg, Germany.
4. S.-F. Stahl, J. Marbach, G. A. Luinstra, *Preparation of tailored poly(propylene ether carbonates) with double metal cyanide and zinc glutarate as catalyst*, 13th International Workshop on Polymer Reaction Engineering, **11. – 14.06.2019**, Hamburg, Germany.

Conference posters

5. J. Marbach, B. Nörnberg, G. A. Luinstra, *Parameter mapping of the zinc glutarate-mediated PO/CO₂ copolymerization using design of experiments*, 49th Annual Meeting of the German Catalysis Society, **16. – 18.03.2016**, Weimar, Germany.
6. J. Marbach, Th. Höfer, G. A. Luinstra, *Synthesis of CO₂-based polyols using nanoscopic zinc glutarate catalysts*, *Macromolecular Colloquium*, **21. – 23.02.2018**, Freiburg, Germany.
7. J. Marbach, S.-F. Stahl, G. A. Luinstra, *Synthesis of novel double metal cyanide catalysts and polymerization of PO and CO₂*, *Polymer Reaction Engineering X*, **20. – 25.05.2018**, Punta Cana, Dominican Republic.
8. S.-F. Stahl, J. Marbach, G. A. Luinstra, *Characterizing Catalyst Performance of DMCs on PO Homopolymerisation*, *Polymer Reaction Engineering X*, **20. – 25.05.2018**, Punta Cana, Dominican Republic.

LIST OF ABBREVIATIONS

ANOVA	analysis of variances
Ar	argon
BPA	2,2-bis(4-hydroxyphenyl)propane, bisphenol A
BPAF	2,2-bis(4-hydroxyphenyl)hexafluoropropane, bisphenol AF
BPS	bis(4-hydroxyphenyl)sulfone, bisphenol S
CCTC	catalytic chain transfer copolymerization
CHO	cyclohexene oxide
CI	confidence interval (95 %)
CO₂	carbon dioxide
cPC	cyclic propylene carbonate
CTA	chain transfer agent
DMC	double metal cyanide
DOE	design of experiments
DSC	differential scanning calorimetry
EA	elemental analysis
ESI-MS	electron spray ionization mass spectrometry
FT	FOURIER transformation
HEBPA	hydroxyethyl-bisphenol A
HPBPA	hydroxypropyl-bisphenol A
HPLC	high performance liquid chromatography
IR	infra-red
LAOS	large amplitude oscillatory shear
MBDMP	4,4'-methylene bis(2,6-dimethylphenol)
N₂	nitrogen

NMR	nuclear magnetic resonance
ODA	octadecylamine
PAC	poly(alkylene carbonate)
PDI	polydispersity index
PI	prediction interval (95 %)
PO	propylene oxide
PET	poly(ethylene terephthalate)
PLS	partial-least-squares
PPC	poly(propylene carbonate)
PS	polystyrene
RI	refractive index
ROP	ring-opening polymerization
RMSE	root-mean squared error
SAOS	small amplitude oscillatory shear
SD	stress decomposition
SEC	size-exclusion chromatography
SEM	scanning electron microscopy
SNV	standard normal variate
THF	tetrahydrofurane
THTPM	4,4',4''-trihydroxytriphenylmethane
TMS	tetramethylsilane
TOF	turnover frequency
TON	turnover number
UV/Vis	ultraviolet/visible
XRD	X-ray diffraction
ZnGA	zinc glutarate

LIST OF SYMBOLS

α	level of the axial points in a central-composite design
γ	strain
γ_0	strain amplitude
$\dot{\gamma}$	strain rate
δ	phase angle
ϵ_{break}	elongation at break
η	viscosity
η'_1	first harmonic dynamic viscosity
η'_L	large-rate dynamic viscosity
η'_M	minimum-rate dynamic viscosity
η_0	zero-shear viscosity
η_∞	infinite-shear viscosity
λ	power-coefficient of BOX-COX transformation
ρ	density
σ_N	normalized stress
σ_s	tensile strength
ω	angular frequency
ΔH_f^0	standard enthalpy of formation
a_x	model coefficients of empirical prediction models
a_T	horizontal shift factor
$a(T)$	coefficient of the PENG-ROBINSON equation of state
b	coefficient of the PENG-ROBINSON equation of state
c_1	WILLIAM-LANDEL-FERRY constant
c_2	WILLIAM-LANDEL-FERRY constant

e_n	n-th elastic CHEBYSHEV coefficient
E_a	activation energy
f	functionality
f_{carb}	content of carbonate linkages in polymer backbone
f_{cPC}	content of cyclic propylene carbonate in the crude product
G'	storage modulus
G''	loss modulus
G'_L	large-strain elastic modulus
G'_M	minimum-strain elastic modulus
G'_n	n-th harmonic storage modulus
G''_n	n-th harmonic loss modulus
G_N^0	plateau modulus
G^*	complex modulus
$I_{n/1}$	intensity of normalized higher harmonics
M_c	critical molecular weight
M_e	entanglement molecular weight
M_n	number-average molecular weight
M_w	weight-average molecular weight
p	pressure
p'	packing length
R^2	coefficient of determination
S	strain-stiffening ratio
t	time
$t_{\text{induction}}$	induction time
t_R	reduced reaction time
$t_{\text{retardation}}$	retardation time

T	temperature, shear-thickening ratio
T_g	glass transition temperature
$T_{g,\infty}$	glass transition temperature at infinity molecular weight
T_n	n-th CHEBYSHEV polynom
T_{ref}	reference temperature
$T_{.5\%}$	decomposition temperature at 5% weight loss
v_n	n-th viscous CHEBYSHEV coefficient
V_m	molar volume
$V(\text{CO}_2)_{\text{reaction}}$	volume of CO_2 consumed during the reaction
$x(\text{CO}_2)$	molar fraction of CO_2
X_{PO}	conversion of PO

TABLE OF CONTENTS

1	SUMMARY.....	1
2	ZUSAMMENFASSUNG.....	3
3	INTRODUCTION AND THEORETICAL BACKGROUND	7
3.1	Copolymerization of epoxides and CO ₂	9
3.2	Catalysts for the CO ₂ /epoxide copolymerization.....	11
3.3	Material properties of poly(alkylene carbonates)	14
3.4	Rheology.....	16
4	SCOPE OF THESIS	21
5	RESULTS AND DISCUSSION.....	23
5.1	Reaction control and process optimization of PO/CO ₂ copolymerizations	23
5.1.1	Catalyst productivity	25
5.1.2	Polymer composition	29
5.1.3	Molecular weight.....	33
5.2	Enhancement of thermal stability of PPC.....	35
5.3	Catalytic chain transfer copolymerization of PO and CO ₂	39
5.3.1	Monofunctional chain transfer agents	40
5.3.2	Multifunctional chain transfer agents.....	46
5.4	Thermo-rheological properties of poly(propylene carbonate) melts.....	59
5.4.1	Small amplitude oscillatory shear conditions	59
5.4.2	Large amplitude oscillatory shear conditions	67
5.5	CO ₂ /epoxide cycloaddition using indium catalysts	75
5.6	Initially active double metal cyanide catalysts.....	79
5.6.1	Synthesis of amine-modified double metal cyanide catalysts	80
5.6.2	<i>Online</i> -reaction monitoring and kinetic studies of DMC catalysts.....	83
5.6.3	Homopolymerization of PO.....	87
5.6.4	Copolymerization with of PO and CO ₂	89
6	EXPERIMENTAL DETAILS	93
6.1	Materials.....	93
6.2	Synthesis of amine-modified DMC catalysts.....	93
6.3	Synthesis of indium complexes	94

6.4	Homopolymerization of PO.....	94
6.5	Copolymerization of PO and CO ₂	95
6.6	Cycloaddition of PO and CO ₂	96
6.7	Material characterization.....	97
7	BIBLIOGRAPHY.....	99
	APPENDIX.....	A1
A1	Hazardous Materials.....	A1
A2	Utilized CMR chemicals	A3
A3	Statutory of declaration	A4
A4	Declaration of my share in the included publications.....	A5

1 SUMMARY

Gaining a profound understanding of underlying processes of heterogeneous catalyzed homopolymerization of epoxides and their copolymerization with CO₂ is useful for improving catalysts performance and tailoring the material properties of the final products. Scope of this thesis, thus, was the analysis of the reaction of epoxides, in particular PO, and CO₂ under the action of several types of catalysts as well as the characterization of the resulting polymeric products.

The copolymerization of CO₂ with PO catalyzed by a nanoscopic ZnGA catalyst was analyzed comprehensively using a design of experiments approach. The influence of various reaction parameters on the catalyst's activity, the polymer composition and the molecular weight could be described by empirical prediction models (Chapter 5.1). The results indicate that the catalyst's performance is governed by the coverage of its surface, with PO and CO₂. The highest productivity and CO₂-selectivity is observed at molar fractions in the feed of $x(\text{CO}_2) \approx 0.3$. Copolymerization in bulk displays a pseudo-living behavior until reaching a threshold of $M_n \approx 80$ kg/mol. High PDI values > 10 at early reaction stages indicate that the initiation reaction is rate-determining. The feature that the selectivity of CO₂-incorporation can be tailored by varying the reaction conditions was utilized to prepare PPC with enhanced thermal stability (Chapter 5.2). (Growing) polymer chain ends could be capped with ether-rich segments by introducing a second reaction stage in a batch polymerization process with reduced CO₂-concentrations. This effectively prevents thermal depolymerization by backbiting, and thus inhibits the formation of volatile organic compounds.

In a further part of the thesis, the preparation of PPC-polyols by means of a catalytic chain transfer copolymerization of PO and CO₂ under the action of nanoscopic ZnGA catalysts is described (Chapter 5.3). The molecular weights of the products can be tuned to values below 2000 g/mol by adjusting the PO/CTA ratio or by controlling the total monomer conversion. The addition of small quantities of CTA leads to an increase in the catalysts TOF of approximately 20 %. *Online*-monitoring of the polymerization revealed that the CTA controlled copolymerization has an induction time, that results from a reversible catalyst deactivation by the CTA. Catalyst deactivation of the CTAs is released after the first monomer additions to them. The induction period scales with the CTA concentration and is dependent on the nucleophilicity of the CTA relative to those of the formed chain ends after PO addition. The chain transfer rate is a function of the carbonate content of the oligomeric products f_{carb} , most likely on account of differences in mobility (diffusion). As a consequence, products with lower f_{carb} show a more uniform chain growth resulting in narrow molecular weight distributions with minimum PDI ≈ 2 . By precisely controlling the reaction conditions, material properties can be tailored in a certain range, giving access to a new class of poly(ether carbonate) polyols.

Thermoplastic processing of PPC is significantly affected by the polymers molecular weight and composition. The thermo-rheological behavior of PPC melts was mapped as a function of their molecular weights ($M_w = 29 - 296$ kg/mol) and polymer compositions ($f_{\text{carb}} = 51 - 92$ mol%) (Chapter 5.4). Experiments were performed under SAOS and LAOS conditions. The experimental findings lead to the insight that incorporation of carbonate entities into the polymer backbone increases chain stiffness, resulting in higher glass transition temperatures T_g and flow activation energies E_a . Conversely, the entanglement molecular weight M_e decreases at higher f_{carb} from 6.4 to 4.2 kg/mol. The zero-shear viscosity η_0 correlates to M_w along a power law with exponents of $a \approx 5$, strongly suggesting the presence of intermolecular associations between polymer chain segments. These interactions have a large impact of the resulting material properties. LAOS experiments show a strain-induced softening of the melts. FOURIER transformation of the distorted sinusoidal stress response reveals higher intrinsic non-linearity for PPC with $f_{\text{carb}} = 80$ mol% compared to melts with higher carbonate contents. The non-linearity ratio $I_{3/1}$ increases with γ_0 , ω and M_w . Orthogonal stress decomposition of the material response reveals a complex non-linear behavior showing intracycle shear-thinning that is preceded by a shear-thickening at intermediate strains.

The reaction of epoxides with CO_2 is not only affected by the reaction conditions but also by the utilized catalyst. In Chapter 5.5 and Chapter 5.6, two different types of catalysts were prepared and tested for their activity in the coupling reaction of epoxides with CO_2 . Homogeneous indium-based complexes are firstly reported upon (Chapter 5.5). All utilized indium catalysts exhibit a high selectivity towards CO_2 incorporation, however, only yielding the cyclic products. Catalyst screening reveals, that the presence of both a LEWIS-acid catalyst and a co-catalyst is required for decent activities. The second type of catalyst that is described are amine-modified Zn/Co-double metal cyanide (DMC) catalysts, prepared by thermal activation of DMC-alkyl amine adducts (Chapter 5.6). These catalytic precursors are obtained by co-precipitation of Zn and Co-cyanide salts in the presence of n -alkyl amines. The chain length of the amine has an impact on the final complex crystallinity and as a result on the catalysts performance after activation. Elemental analysis and FTIR spectra indicate the formation of DMC-alkyl amine adducts with the general structural formula $\text{Zn}_3[\text{Co}(\text{CN})_6]_2 \cdot 8 \text{H}_2\text{N}(\text{CH}_2)_n\text{CH}_3 \cdot b \text{Zn}(\text{NO}_3)_2 \cdot c \text{H}_2\text{O}$. Thermal treatment of adducts results in the partial removal of the amine and gives an active propoxylation catalyst, one of the first initial active DMC complexes, *i.e.* a DMC compound that does not show an induction period. Residual amine moieties remaining in the activated catalyst are affecting the catalytic properties. The catalysts exhibit a high selectivity towards CO_2 incorporation giving access to PPC with an unusual high carbonate content ($f_{\text{carb}} = 88$ mol%) among the highest reported for DMC catalysts yet.

2 ZUSAMMENFASSUNG

Tiefgreifendes Verständnis der Mechanismen der heterogen-katalysierten Homopolymerisation von Epoxiden sowie der Copolymerisation mit CO_2 ist essentiell für die Verbesserung der Katalysatorleistung und die Steuerung der Materialeigenschaften der finalen Produkte. Ziel dieser Arbeit war daher die Untersuchung der Reaktion von Epoxiden, insbesondere PO, und CO_2 unter Einsatz verschiedener Katalysatortypen sowie die Charakterisierung der resultierenden polymeren Produkte.

Die Copolymerisation von CO_2 mit PO unter Verwendung eines nanoskopischen ZnGA Katalysators wurde systematisch mittels statistischer Versuchsplanung analysiert. Der Einfluss verschiedener Reaktionsparameter auf die Katalysatoraktivität, die Polymerzusammensetzung sowie das Molekulargewicht der Produkte kann mittels empirischer Vorhersagemodelle beschrieben werden (Kapitel 5.1). Die Ergebnisse zeigen, dass die Katalysatorleistung maßgeblich durch die Belegung der Katalysatoroberfläche bestimmt wird. Die höchste Produktivität und CO_2 -Selektivität wird bei einem Anteil von $x(\text{CO}_2) \approx 0.3$ im Reaktionsgemisch beobachtet. Die Copolymerisation in Masse zeigt anfänglich ein pseudo-lebendes Verhalten, bis zum Überschreiten eines Grenzwertes von $M_n \approx 80$ kg/mol. Hohe PDIs von > 10 in frühen Reaktionsstadien deuten darauf hin, dass die Initiierungsreaktion geschwindigkeitsbestimmend ist. Die Eigenschaft von Zinkglutaratkatalysatoren die Selektivität des CO_2 -Einbaus bei Variation der Reaktionsbedingungen zu verändern, wurde für die Synthese von PPC mit erhöhter thermischer Stabilität genutzt (Kapitel 5.2). (Aktive) Carbonat-reiche Ketten(enden) werden mit Ether-haltigen Segmenten gecapped durch Einführen einer zweiten Reaktionsphase während der Batchpolymerisation, gekennzeichnet durch verringerte CO_2 -Konzentrationen. Dies verhindert effektiv die thermische Depolymerisation durch *Backbiting* und damit einhergehend die Bildung flüchtiger organischer Komponenten.

In einem weiteren Teil der Arbeit wird die Herstellung von PPC-Polyolen mittels katalytischer Kettentransfer-Copolymerisation von PO und CO_2 unter Verwendung von nanoskopischen ZnGA-Katalysatoren beschrieben (Kapitel 5.3). Durch Anpassung des Verhältnisses von PO/CTA sowie Steuerung des Umsatzes kann das Molekulargewicht der Produkte auf Werte unterhalb von 2000 g/mol eingestellt werden. Die Zugabe von kleinen Mengen CTA führt zu einer Erhöhung der Katalysatorumsatzrate von ca. 20 %. *Online*-Reaktionsverfolgung zeigt, dass die CTA-regulierte Copolymerisation durch eine Induktionsphase gekennzeichnet ist, die aus einer reversiblen Katalysatordesaktivierung durch das CTA resultiert. Die Deaktivierung wird durch die ersten Monomeranlagerungen an das CTA aufgehoben. Die Induktionszeit skaliert mit der CTA-Konzentration und ist abhängig von der Nukleophilie des CTA relativ zu gebildeten Kettenenden nach PO-Addition. Die Geschwindigkeit der Kettentransferreaktion ist eine Funktion des Carbonatgehaltes f_{carb} aufgrund von Mobilitätsunterschieden der Polymere (Diffusion). Daraus ergibt sich, dass Produkte mit geringerem f_{carb} einheitlicheres Kettenwachstum zeigen, bedingt durch ihre höhere Kettenbeweglichkeit. Durch Kontrolle der

Reaktionsbedingungen können die resultierenden Materialeigenschaften in einem bestimmten Bereich maßgeschneidert werden. Die Steuerung der Produkteigenschaften erlaubt Zugang zu einer neuen Klasse von Poly(ethercarbonat)-Polyolen.

Die thermoplastische Prozessierung von PPC wird maßgeblich vom Molekulargewicht der Produkte sowie der Polymerzusammensetzung beeinflusst. Das thermo-rheologische Verhalten von PPC-Schmelzen mit Molekulargewichten zwischen $M_w = 29 - 296$ kg/mol und Polymerzusammensetzungen von $f_{\text{carb}} = 51 - 92$ mol% wurde untersucht (Kapitel 5.4). Experimente wurden unter SAOS und LAOS Bedingungen durchgeführt. Die experimentellen Ergebnisse zeigen, dass der Einbau von Carbonat-Einheiten in das Polymerrückgrad die Kettensteifigkeit erhöht. Daraus resultieren unter anderem höhere Werte für die Glasübergangstemperatur T_g sowie die Fließaktivierungsenergie E_a . Entgegen der erhöhten Steifigkeit nimmt das Verschlaufungsmolekulargewicht M_e mit höheren f_{carb} von 6.4 auf 4.2 kg/mol ab. Die Nullscher-viskosität η_0 korreliert mit M_w und folgt einem exponentiellen Zusammenhang mit Exponenten von $a \approx 5$, die stark auf die Anwesenheit von intermolekularen Wechselwirkungen zwischen Polymersegmenten hindeuten. Derartige Wechselwirkungen beeinflussen die resultierenden Materialeigenschaften. Experimente unter LAOS Bedingungen zeigen ein scher-induziertes Erweichen der Schmelzen. FOURIER-Transformationen der verzerrten sinusförmigen Spannungsantworten zeigen höhere intrinsische Nichtlinearitäten für PPC mit $f_{\text{carb}} = 80$ mol%, verglichen mit Proben mit höherem Carbonatgehalt. Das Nichtlinearitätsverhältnis $I_{3/1}$ erhöht sich mit γ_0 , ω und M_w . Orthogonale Spannungszerlegung der Materialantwort zeigt ein komplexes nicht-lineares Verhalten mit intrazyklischer Scherverdünnung, der eine Scherverdickung vorausgeht.

Die Reaktion von Epoxiden mit CO_2 wird nicht nur durch die gewählten Reaktionsbedingungen beeinflusst, sondern auch durch die Art des verwendeten Katalysators. In den Kapiteln 5.5 und 5.6 wurden zwei verschiedene Katalysatortypen hergestellt und auf ihre Aktivität für die Reaktion von Epoxiden mit CO_2 untersucht. Homogene Indium-basierte Komplexe wurden erstmalig als Katalysatoren für diese Reaktion berichtet (Kapitel 5.5). Alle verwendeten Indium-Katalysatoren zeichnen sich durch eine hohe CO_2 -Selektivität aus, liefern jedoch ausschließlich zyklische Produkte. Ein Katalysatorscreening zeigte, dass die Anwesenheit eines LEWIS-sauren Katalysators und eines Co-Katalysators für hohe Umsatzraten erforderlich ist. Neben den homogenen Systemen wurden Amin-modifizierte Zn/Co-Doppelmetallcyanid (DMC) Katalysatoren, hergestellt durch die thermische Zersetzung von DMC-Alkylamin-Addukten beschrieben (Kapitel 5.6). Die Katalysatorvorstufen wurden durch die Co-Fällung von Zink- und Cobalt(cyanido)salzen in Gegenwart von n -Alkylaminen erhalten. Die Kettenlänge der verwendeten Amine beeinflusst die Kristallinität der resultierenden Komplexe sowie die Katalysatorleistung nach ihrer Aktivierung. Elementaranalyse und FTIR-Spektren deuten auf die Bildung von DMC-Alkylamin-Addukten mit der allgemeinen Strukturformel $\text{Zn}_3[\text{Co}(\text{CN})_6]_2 \cdot 8 \text{H}_2\text{N}(\text{CH}_2)_n\text{CH}_3 \cdot b \text{Zn}(\text{NO}_3)_2 \cdot c \text{H}_2\text{O}$ hin. Thermische Behandlung der Addukte resultiert in der partiellen Entfernung des Amins und liefert aktive Propoxylierungskatalysatoren. Restliche im Katalysator verbleibende Aminfunktionalitäten beeinflussen die

katalytischen Eigenschaften. Die so erhaltenen Komplexe zählen zu den ersten Beispielen für initial-aktive DMC Katalysatoren, d.h. DMCs die keine Induktionsphase zeigen. Die Amin-modifizierten DMCs liefern die höchsten bisher bekannten Carbonatgehalte ($f_{\text{carb}} = 88 \text{ mol\%}$) für die DMC-katalysierte Copolymerisation von PO und CO_2 .

3 INTRODUCTION AND THEORETICAL BACKGROUND

The 20th century marks the onset of the age of plastics. Since the discovery of polymers, plastics became an indispensable part of today's daily life. The production of plastics has experienced a substantial growth over the last couple of decades, recently exceeding values of 300 Mt/a. In Europe, a major fraction of the annual plastic demand is resulting from packaging applications (Figure 3.1).¹

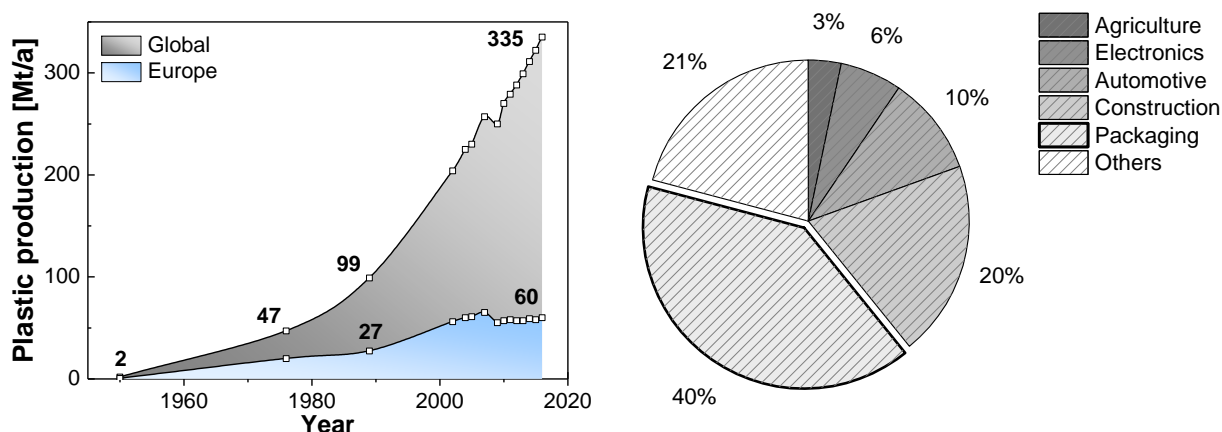


Figure 3.1 Left: Global and European annual plastic production over the last 60 years. Right: Annual demand of plastics in Europe in different application fields.¹

The main feedstock for most plastics is petroleum. The annual plastic production accounts for approximately 4 % of the global consumption of non-renewable fossil resources. The limited availability of fossil resources and perhaps more of importance the growing public awareness of the backlash of using these resources has driven the search for alternative and more sustainable raw materials. Examples for such are cellulose and lignin, but also carbon dioxide (CO₂). The use of CO₂ as a C₁ building block in chemical industry is of particular interest as it is a potentially abundant, non-toxic and renewable feedstock.² Table 3.1 lists the main sources of anthropogenic CO₂-emission.

Table 3.1 Point emission sources of CO₂ and the corresponding purity of the gas.^{3,4}

Emission source	CO ₂ emission [Mt/a]	CO ₂ purity [%]
Coal	14 200	12 – 15
Natural gas	6 320	3 – 5
Cement production	2 000	14 – 33
Iron and steel production	1 000	15
Refineries	850	3 – 13
Ethylene production	260	12
Ammonia production	150	100
Natural gas production	50	5 – 70

CO₂ is already utilized as a feedstock in a number of industrial processes (Figure 3.2).^{5,6} For instance, approximately 130 Mt CO₂ are consumed annually for chemical transformations, with urea as a main product (112 Mt/a CO₂ consumed).² However, considering the high energy input that is required to synthesize ammonia (Table 3.1), the production of urea is actually an emission source in net CO₂-balance. In addition, the urea is predominantly used as a fertilizer, *i.e.* slowly hydrolyzes into back ammonia and CO₂. When aiming at binding CO₂ and thus avoiding further emissions, it therefore is important to consider the required energy for the reaction and the production of the reactants as well as the lifecycle of the product.

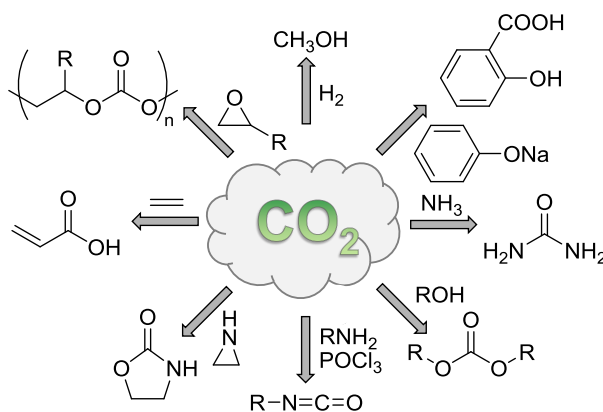


Figure 3.2 Examples of products derived from CO₂.

The environmental impact of littered plastics is one of the major problems of the world. The increasing global use of plastic materials combined with ineffective waste collection, unsolved disposal and control over trade with waste streams in combination with the lacking awareness of the consequences of their persistency against microbial degradation is becoming a serious threat to the global ecology. Approximately 8 Mt of plastic waste end up as marine debris every year, mostly in the Pacific Ocean.⁷ Most common plastics such as polyolefins and aromatic polyesters, *e.g.* PET, show a high resilience against bacterial degradation. The plastic waste may be broken down into smaller particles as the result of physical and chemical processes.⁸ The result is so-called microplastic, which is known to may contain some level of toxic pollutants such as halogenated and polyaromatic hydrocarbons and/or pesticides.⁹ These pollutants can be washed out over time and enter the food chain if microplastics are ingested by marine wildlife. The increasing accumulation of plastic waste in marine ecosystems results in a growing interest in biodegradable plastics derived from renewable resources.

Aliphatic polycarbonates (PACs) are a class of polymers that can meet the requirements of being biodegradable and being bio-based. Their non-aromatic backbone composed of carbonate-linkages enables the hydrolytic and enzymatic degradation by microorganism.¹⁰ Furthermore, PACs can be synthesized by the alternating copolymerization of CO₂ with epoxides. A useful epoxide in that regard seems propylene oxide (PO), a commodity chemical that is industrially produced by oxidation of propylene. However, research has shown alternative pathways for the preparation PO from renewable feedstocks such as glycerol, a side product of biodiesel manufacturing.¹¹

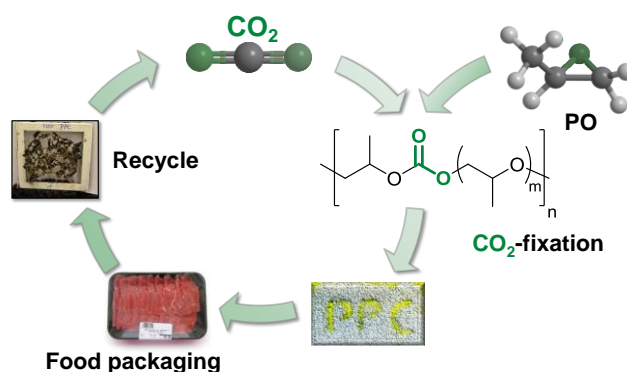


Figure 3.3 Chemical fixation of CO₂ and application of the transparent poly(propylene carbonate) (PPC) for short-term packaging applications. Images were taken from ^{12,13}.

PACs have, on account of their biocompatibility and biodegradability, potential for sustainable short-term applications such as food packaging.^{14–16} Poly(propylene carbonate) (PPC) is considered as one of the most promising PACs as it features excellent gas barrier properties as well as high resilience at high molecular weights.¹⁷ Furthermore, it can be combusted without leaving char residues which renders its industrial application as sacrificial binding material.¹⁸ Other possible fields of application are as polyol compound in polyurethane manufacturing^{19–21} and for biomedical implants^{22–24}.

3.1 Synthesis of polycarbonates

Polycarbonates can be prepared by various synthetic pathways utilizing different carbonyl sources (Figure 3.4). Aromatic polycarbonates are prepared on an industrial scale by polycondensation of phosgene or organic carbonates with diols.²⁵ A different procedure to synthesize polycarbonates is the ring-opening polymerization (ROP) of cyclic carbonates. Several studies report the polymerization of trimethylene carbonate and its derivatives with focus on functional materials, *e.g.* for medical applications.²⁶ However, a major drawback of these routes is the use of highly toxic phosgene or its derivatives as raw material.

In contrast, the use of CO₂ as carbonyl source for the formation of PACs is of particular interest as it represents a more sustainable feedstock. One approach is the direct copolymerization with diols. However, only low molecular weight products are achieved limiting the overall applicability of the resulting polymers.^{27,28} Similarly, the ring-opening copolymerization with oxetanes yields low molecular weight products.^{29,30} The alternating copolymerization of CO₂ with epoxides, however, allows the synthesis of high-molecular weight polycarbonates in excellent yields.¹³

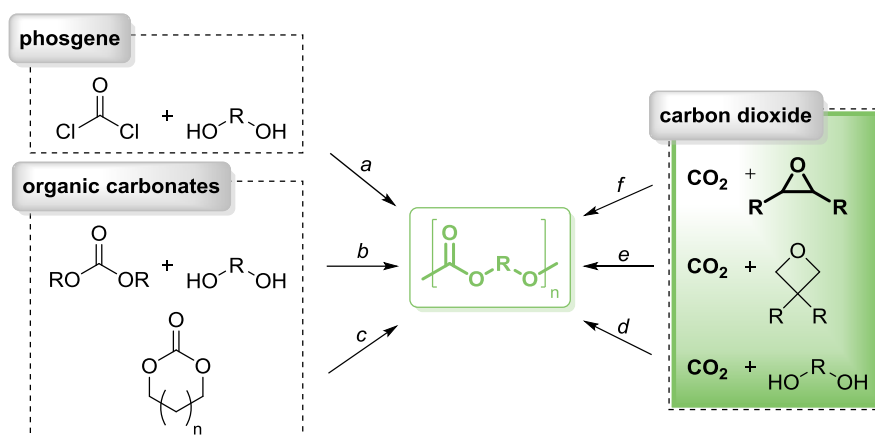


Figure 3.4 Synthesis of polycarbonates by polycondensation of phosgene with diols (a), organic carbonates with diols (b), ring-opening polymerization of cyclic carbonates (c), polycondensation of CO₂ with diols (d) and ring-opening copolymerization of CO₂ with oxetanes (e) or epoxides (f).

Mechanistically, the copolymerization of epoxides and CO₂ may proceed by a two-step mechanism. In a first step a pre-coordinated epoxide is ring-opened to form a metal-alkoxide. The ring-opening is then followed by the insertion of CO₂ (Figure 3.5).³¹ The consecutive insertion of PO units results in the formation of ether linkages. These are a typical feature of most heterogeneous catalysts for the CO₂/epoxide-copolymerization.

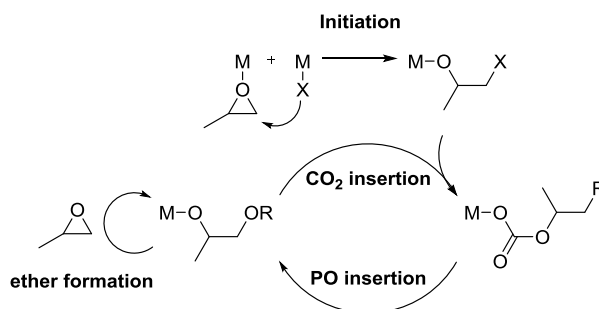


Figure 3.5 Proposed mechanism of the alternating copolymerization of CO₂ and PO.³²

A DFT-calculated energy profile for the alternating copolymerization of CO₂ and PO is displayed in Figure 3.6. The nucleophilic ring-opening of PO usually occurs at the sterically least hindered site. However, depending on the transition state the cleavage can also occur in β -position resulting in regio-irregular polymers.³¹ The consecutive insertion of two or more epoxide units results in ether linkages. The formation of “dicarbonate anhydride” units, in contrast, is thermodynamically disfavored and has not been reported upon.³¹ The selectivity of CO₂ vs epoxide incorporation is affected by the utilized catalytic system as well as the applied reaction conditions. A common side product of the CO₂/epoxide copolymerization is the five-membered cyclic carbonate that is formed by backbiting of alkoxide or carbonate chain ends.³³

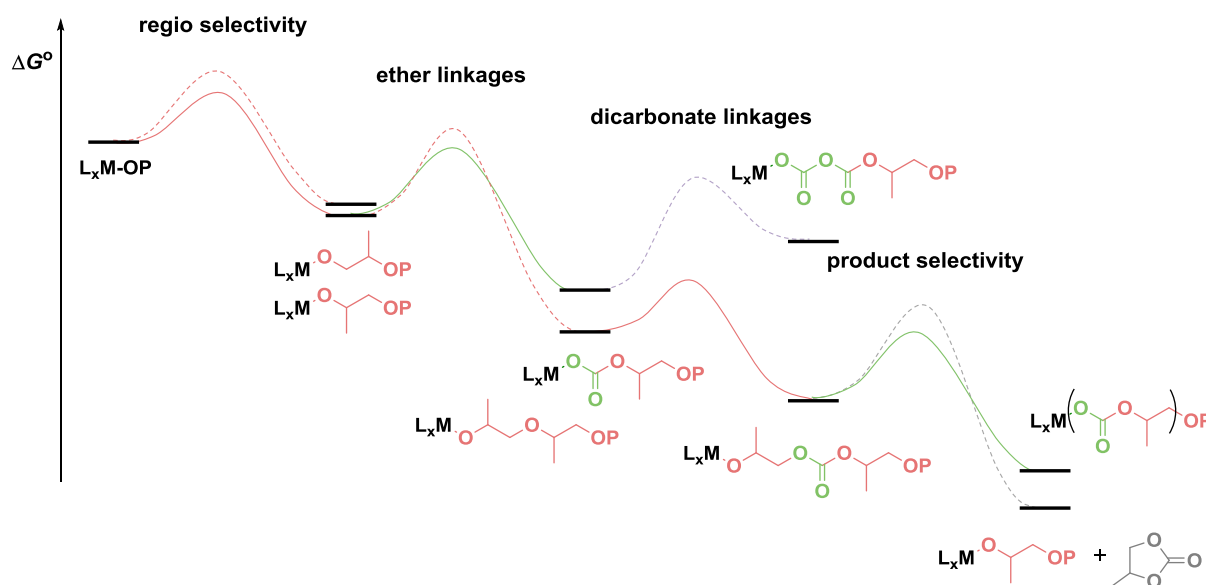


Figure 3.6 Qualitative free energy profile of the alternating copolymerization of PO and CO₂.³¹

3.2 Catalysts for the CO₂/epoxide copolymerization

The catalytic conversion of CO₂ to form polycarbonates was first reported by INOUE.³⁴ Since this early discovery, the development of new catalytic systems has been subject of numerous studies. Some common catalysts for the CO₂/epoxide copolymerization are given in Table 3.2.

Table 3.2 Catalysts for the copolymerization of epoxides with CO₂.¹⁵

Type	Catalyst	Features
<i>Homogeneous</i>	Metal-porphyrin	Discrete catalyst structure
	Metal-phenoxide	Catalyst removal difficult
	Metal-β-diiminat	High synthetic effort towards catalysts with high activity and selectivity
	Metal-salen or salan	Mainly used for bicyclic epoxides Products with tunable molecular weights
<i>Heterogeneous</i>	Diethyl zinc	Low activity
	Zinc dicarboxylate	Facile preparation from non-toxic precursors Moderate activity
	Double metal cyanide (DMC)	Facile preparation High activity Low level of CO ₂ incorporation
	Ternary rare-earth	Facile preparation Moderate activity

The first catalytic system that was utilized for the copolymerization of CO₂ and PO were mixtures of ZnEt₂ and protic compounds that showed only low activities.³⁴ The lack of in-depth

understanding of the polymerization pathway was frustrating the efforts for more active systems and finally led to the development of various homogeneous catalysts. The well-defined structure of those single-site catalysts allowed identifying structure/reactivity relationships. LUISTRA and RIEGER³⁵ showed – following insights reached by JACOBSEN^{36,37} on the kinetic resolution of epoxides and earlier work by INOUE³⁸ on immortal polymerizations with porphyrine systems – that an effective pathway exists in chromium salen systems when two centers cooperate, one holding the anionic chain end, one activating the epoxide. Studies by COATES lead to the hypothesis that the copolymerization possibly involves two metal centers in dimeric zinc diketimines.³⁹ It was thus suggested that the mechanism comprises a cooperative, bimetallic pathway with the pre-coordination of epoxide by one metal center and the subsequent ring-opening by a nucleophile coordinated to a second metal. As a consequence, synthetic efforts were directed towards the preparation of bimetallic catalysts with β -diiminate^{40–42}, anilido-aldimine^{43,44} and ROBSON-type ligands.^{45,46} The catalysts showed superior activities while displaying good to excellent selectivities. The most active catalyst for the CO₂/cyclohexene oxide copolymerization up to this date comprises a flexibility-tethered dinucleating backbone (Figure 3.7).^{47,48}

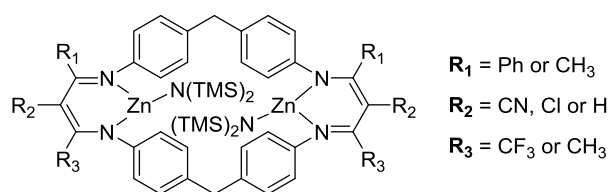


Figure 3.7 Flexibility-tethered Zn catalyst for the copolymerization of cyclohexane oxide (CHO) and CO₂ showing the highest initial activities reported (TOF = 155 000 h⁻¹).^{47,48}

A characteristic feature of many homogeneous catalysts for the CO₂/epoxide copolymerization is that the presence of a co-catalyst is generally required. Usually, nucleophiles like halides of quaternary ammonium salts, phosphines or *N*-heterocyclic amines are employed as co-catalysts.³² A successful approach by LEE and later followed by LU is to combine both, the catalyst and the co-catalyst in single complex.^{49,50} This was first reported by LEE, introducing cationic side chains with chloride and nitrate anions into a salen-framework resulting in the most active catalyst for the copolymerization of PO and CO₂ reported up to that date (Figure 3.8). In addition, the catalyst shows a remarkable selectivity towards CO₂ incorporation forming perfectly alternating PPC exclusively, without the formation of cyclic by-products.^{51,52}

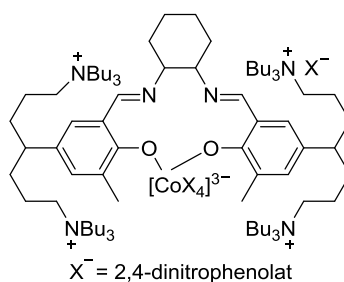


Figure 3.8 Co(salen) catalyst bearing cationic side chains. The cationic side chains are believed to electrostatically attract free polymer chains, thereby preventing the backbiting reaction to form cPC.

While homogeneous single-site catalysts show in part excellent catalytic activities and selectivities, their synthesis usually involves multiple synthetic and chromatographic purification steps. In addition, homogeneous catalysts are generally difficult to remove from the final products which as a consequence often display undesired coloration.¹⁵ In contrast, heterogeneous catalysts can easily be separated or even remain in the polymer. Latter case is referred to as leave-in catalyst and is of great interest as additional purification steps are accompanied by higher production costs of the final product. The industrially most viable catalysts are double metal cyanides (DMC) and zinc dicarboxylates, *e.g.* zinc glutarate (ZnGA), both featuring zinc as active site. They can be prepared by facile and scalable reactions.¹⁵ DMC catalysts were originally developed for the synthesis of poly(ether)-polyols but can also be adopted to copolymerize CO₂ with epoxides.⁵³ Generally, low CO₂ incorporations are achieved resulting in poly(ether carbonates) with larger contents of ether linkages in the polymer backbone.^{54–57} In addition, the most active DMCs contain cobalt as a central metal which is prohibitive for certain applications.⁵⁸

Zinc dicarboxylates show a high activity towards CO₂ incorporation and the catalyst can be prepared from exclusively non-toxic starting materials.⁵⁹ This enables the application of the obtained polycarbonates for instance for food-packaging. The activity of the catalyst depends on the utilized zinc precursors^{60,61}, the solvent and the temperature^{62,63} as well as the intermixing during the catalyst preparation.⁶⁴ The goal is in general to decrease the particle size and thereby to increase the specific surface area. Various studies show that the morphology and surface area of zinc dicarboxylates can be influenced by the addition of surfactants.⁶⁵ The most active ZnGA catalyst reported in the literature was prepared by utilizing non-ionic surfactants such as alkyl amines. ZnGA-amine adducts are formed that can be thermally decomposed to yield nanoscopic ZnGA (Figure 3.9).^{62,66} The crystal structure of the nanoscopic ZnGA is identical with the previously published structure.⁶⁷

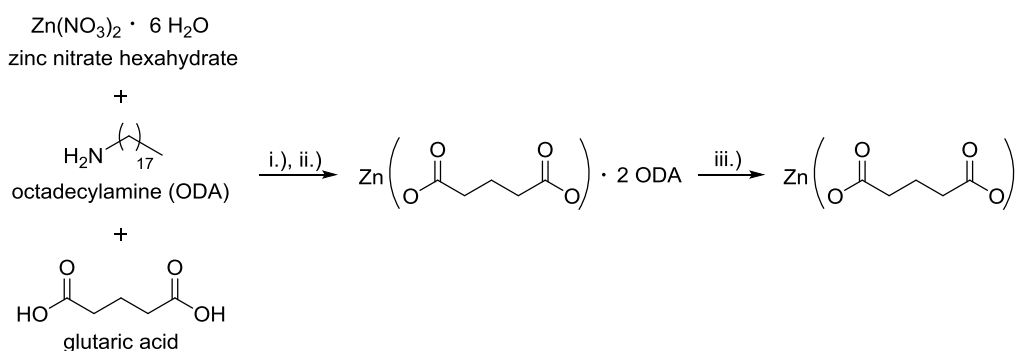


Figure 3.9 Synthesis of nanoscopic ZnGA using alkyl amines as surfactants. In the first step a ZnGA-ODA adduct is formed which is then thermally decomposed to yield the active ZnGA catalyst. i.) ethanol, rt, 24 h, ii.) centrifugation, iii.) activation, $T = 130 \text{ }^\circ\text{C}$, $p = 10^{-2} \text{ mbar}$.

Zinc dicarboxylates with C₅ to C₇-dicarboxylic acids show the highest catalytic activity for the CO₂/epoxide copolymerization. All homologues crystallize in the *P2/c* space group and exhibit the same structural motif in the *hkl*-plane [100] with four Zn atoms showing Zn-Zn distances of 4.6 – 4.8 Å.⁵⁹ The view at the *ac*-plane of single crystalline ZnGA is displayed in Figure 3.10.

All Zn^{2+} centers are coordinated by four carbonyl-oxygens in a tetrahedral geometry. Depending on the conformation of the glutarate ligands, two metallacycles are observed (Figure 3.10, A and B) that form a porous three-dimensional network. The pores, however, are inaccessible for monomer diffusion as they are almost entirely filled by the VAN-DER-WAALS volume of the glutarate ligands.⁶⁸

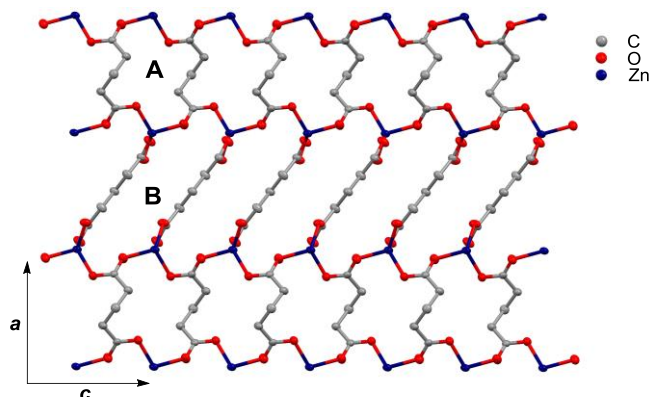


Figure 3.10 View at the *ac*-plane of single crystalline ZnGA. The atoms are distinguished as following: C, grey; O, red; Zn, blue.⁶⁸

3.3 Material properties of poly(alkylene carbonates)

PACs have been handled as promising alternatives to common petro-based materials on account of their biodegradability. The physical properties of the polycarbonates can be tuned in a certain range, *e.g.* in dependence on the nature of the corresponding epoxide.⁶⁹ Epoxides bearing linear alkyl-substituents result in polymers with relatively low glass transition temperatures (T_g) down to $-38\text{ }^\circ\text{C}$ for the copolymer of CO_2 and 1-dodecane oxide.⁷⁰ In contrast, epoxides with bulky alkyl and phenyl-substituents yield polymers with T_g up to $84\text{ }^\circ\text{C}$ (Figure 3.11).⁷⁰ Even higher T_g are observed for alicyclic polycarbonates. As a consequence, the physical properties of poly(cyclohexene carbonate) are similar to polystyrene. The highest glass transition for CO_2 -based polycarbonates is reported for a carbonate-functionalized poly(limonene carbonate) with $T_g = 180\text{ }^\circ\text{C}$, obtained by epoxidation and subsequent carbonatization of poly(limonene carbonate).⁷¹

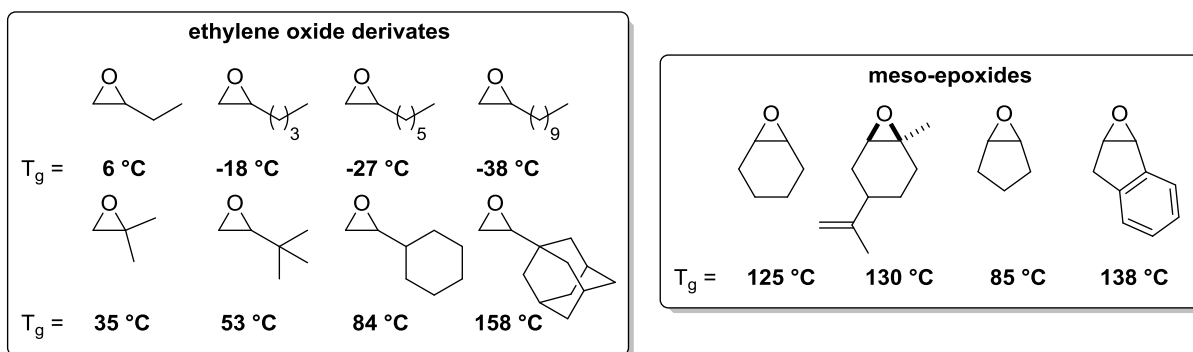


Figure 3.11 Mono- and di-substituted (left) and meso-epoxides (right) utilized for the copolymerization with CO_2 and T_g of the corresponding polycarbonates.⁷⁰⁻⁷⁶

Besides the nature of the epoxide monomer, the material properties are affected by the polymer composition with respect to carbonate vs ether linkages. Latter are formed by the consecutive insertion of one or more epoxide units and typically are observed for polycarbonates synthesized by DMC or zinc dicarboxylates as polymerization catalysts.¹⁵ The formation of ether linkages leads to a decrease in T_g and the elastic modulus of the polymers. However, it enhances the thermal stability of the polycarbonates as the backbiting reaction to form the five-membered cyclic carbonates necessarily ends at ether-linkages.^{17,77} One of the most attractive representatives of the PACs is PPC, as it can be easily obtained from commodity starting materials, PO and CO₂. PPC is a transparent, completely biodegradable and biocompatible thermoplastic material. Furthermore, it shows excellent adhesive and gas barrier properties.¹³ Alternating PPC contains about 43 wt.% CO₂. Table 3.3 summarizes the thermal and mechanical properties as well as the gas permeation behavior for PPC with different compositions.

Table 3.3 Material properties of PPC of various compositions ($M_n = 72 - 92$ kg/mol).¹⁷ $T_{-5\%}$ = temperature at 5% weight loss, σ_s = tensile strength, ϵ_{break} = elongation at break.

f_{carb} [mol%]	T_g [°C]	$T_{-5\%}$ [°C]	σ_s [MPa]	ϵ_{break} [%]	O ₂ [cm ³ /m ² / 24 h/0.1 MPa]	CO ₂ [cm ³ /m ² / 24 h/0.1 MPa]	N ₂ [cm ³ /m ² / 24 h/0.1 MPa]
99.4	45.2	218.6	55.4	8.5	14 ± 1	220 ± 3	11 ± 1
95.5	43.3	230.9	49.3	12.6	17 ± 1	253 ± 5	15 ± 1
88.7	43.7	240.1	27.5	21.2	22 ± 1	288 ± 7	19 ± 1
55.8	20.5	240.4	4.5	1306	88 ± 3	579 ± 11	79 ± 3

The thermal instability is one major drawback of PPC as it undergoes a rapid depolymerization at elevated temperatures. At temperatures below 200 °C the decomposition proceeds mainly by the backbiting reaction to form cyclic propylene carbonate (cPC). At even higher temperatures, random chain scission becomes the predominant depolymerization mechanism (Figure 3.12).^{77,78} The degradation behavior is further affected by the presence of nucleophiles⁷⁹ and catalyst residues.^{35,80}

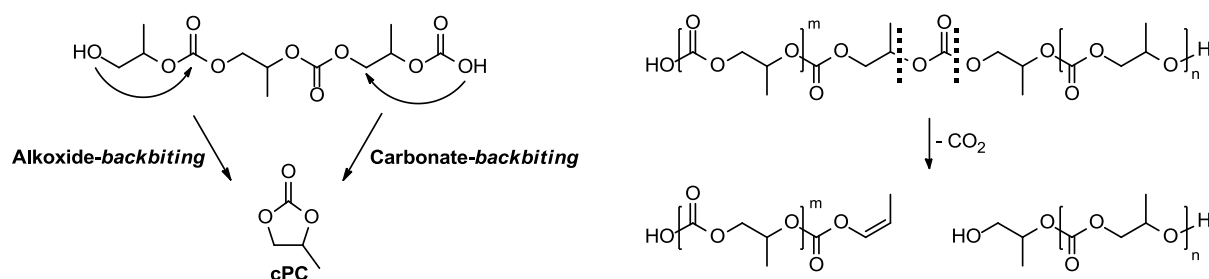


Figure 3.12 Predominant thermal decomposition mechanism for PPC at $T < 200$ °C (left) and $T > 200$ °C (right).

In order to overcome the thermal degradation via backbiting, a post-polymerization work-up of the crude polymer may help. There are several reports that focus on either removing catalyst residues⁷⁹ or preventing the unzipping by the means of end-capping. Possible capping agents include phosphoric esters⁸¹, silicates⁷⁸ and cyclic anhydrides^{81–83}. However, post-polymerization end-capping is an additional processing step and requires the addition of capping agents. Such treatment thus leads to higher production costs. Same holds true for other processing

steps, like the removal of catalyst residues⁸⁴. Another possibility to enhance the stability towards backbiting is the incorporation of additional monomers like epoxides^{85–91}, lactide^{92–94} and cyclic anhydrides^{95–99}. Modification of the polymer backbone can increase the thermal stability and prevent the unzipping reaction to some extent.

3.4 Rheology

Rheology is the science of flow of matter. Knowledge of the rheological behavior under specific deformations is crucial for polymer processing and applications. Different types of deformation may be distinguished: shear (linear or oscillatory) and extension.¹⁰⁰ Oscillatory shear experiments are widely applied for non-destructive probing of the flow behavior of polymer melts and solutions. The experiments are in that case performed under so-called small amplitude oscillatory shear (SAOS) conditions. Upon applying a sinusoidal deformation $\gamma(t) = \gamma_0 \cdot \sin \omega t$, a time-dependent stress-response $\sigma(t)$ is measured (Figure 3.13).

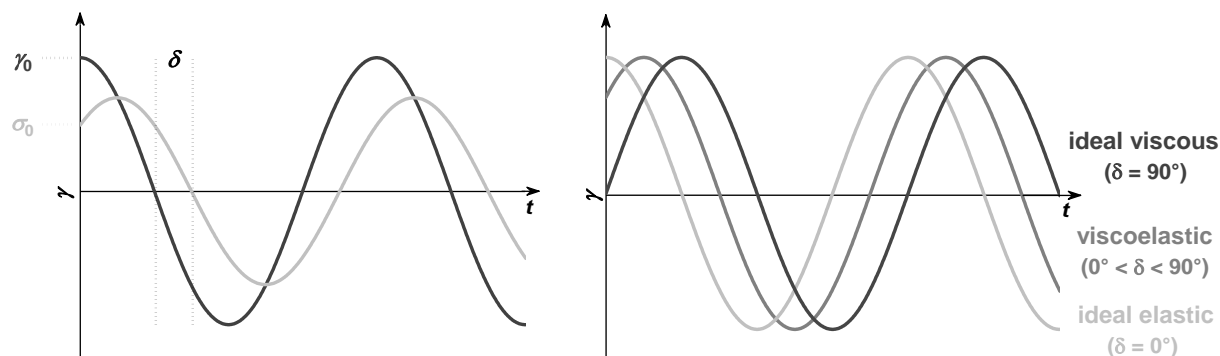


Figure 3.13 Illustration of an oscillatory shear experiment. Depending on the phase angle δ , ideal elastic, ideal viscous and viscoelastic materials are differentiated.

The material response may show a certain phase angle $\delta = 0 - 90^\circ$, depending on the nature of the sample. If the material behaves like an ideal elastic solid, it obeys HOOKE's law:

$$\sigma = G \cdot \gamma \quad (3.1)$$

with the elastic modulus G and is perfectly in phase with the applied strain ($\delta = 0^\circ$). In contrast, the stress response of an ideal viscous fluid is a function of the strain rate and, thus, shows a phase angle of $\delta = 90^\circ$. Ideal fluids follow NEWTON's law:

$$\sigma = \eta \cdot \dot{\gamma} \quad (3.2)$$

with the viscosity η and the strain-rate $\dot{\gamma}$. Polymer solutions and melts, however, may show both elastic and viscous behavior, *i.e.* they have intermediate phase angles. A complex modulus G^* may be defined as the complex combination of an elastic and a viscous contribution:

$$G^* = G' + i \cdot G'' \quad (3.3)$$

with the storage modulus G' and the loss modulus G'' . The total stress response hence is expressed by Equation 3.4

$$\sigma(t) = \gamma_0 (G' \cdot \sin \omega t + G'' \cdot \cos \omega t) \quad (3.4)$$

The storage modulus G' and loss modulus G'' represent the elastic and viscous contribution, respectively. G' and G'' are related by the loss factor $\tan \delta$:

$$\tan \delta = \frac{G''}{G'} \quad (3.5)$$

The value of $\tan \delta$ describes, whether the sample shows predominantly fluid-like ($\tan \delta > 1$) or elastic behavior ($\tan \delta < 1$). The frequency and strain dependence of a viscoelastic fluid can be displayed in the two-dimensional PIPKIN diagram.¹⁰¹

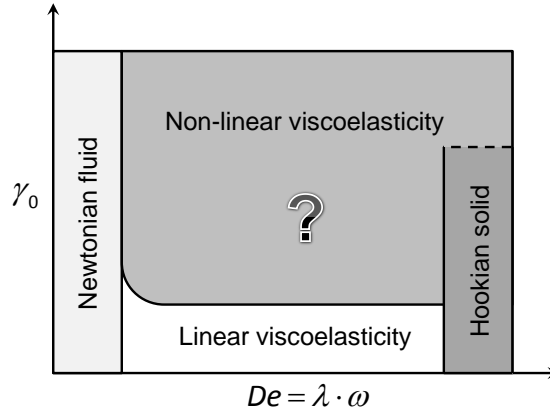


Figure 3.14 PIPKIN diagram representing different flow regions in dependence on the excitation frequency ω (here: DEBORAH number $De = \lambda \cdot \omega$ with the relaxation time λ) and the deformation amplitude γ_0 .

The material response may be classified into four areas, depending on the flow conditions. At low frequencies or short relaxation times ($De \rightarrow 0$) the material behaves like a NEWTONian fluid, whereas at high frequencies or long reaction times ($De \rightarrow \infty$) elastic behavior is observed. In the intermediate region, the material shows viscoelastic behavior, *i.e.* G' and G'' are strain independent. With increasing deformation, however, G' and G'' are becoming functions of the strain amplitude. As a result, a distorted non-sinusoidal stress response is observed. Concomitantly, the viscoelastic response differs from the linear regime under SAOS conditions. The non-linear stress response may be described using different approaches.¹⁰² HYUN found four general types of stress responses at large amplitude oscillatory shear (LAOS) conditions by plotting the linear moduli G' and G'' as a function of the deformation: strain-thinning (type I, G' and G'' decreasing), strain-hardening (type II, G' and G'' increasing), weak strain overshoot (type III, G' decreasing, G'' increasing and subsequently decreasing) and strong strain overshoot (type IV, G' and G'' increasing and subsequently decreasing).¹⁰³ Equations 3.1 – 3.5 are only valid in the linear-viscoelastic regime, *i.e.* G' and G'' don't have a physical meaning under LAOS conditions anymore.

To quantify the non-linear flow behavior, two complementary frameworks are being used. The FT-rheology comprises a time-domain representation whereas the orthogonal stress decomposition gives a deformation-domain insight. Latter was initially developed to overcome the lack of physical meaning of the linear moduli.¹⁰⁴ The total stress response may be separated into an elastic and a viscous contribution

$$\sigma(t, \omega, \gamma_0) = \sigma'(\gamma(t)) + \sigma''(\dot{\gamma}(t)) \quad (3.6)$$

EWOLDT expressed the viscoelastic response in form of CHEBYSHEV polynomials T_n

$$\sigma'(x) + \sigma''(y) = \gamma_0 \sum_{n, \text{odd}} e_n(\omega, \gamma_0) \cdot T_n(x) + \dot{\gamma}_0 \sum_{n, \text{odd}} v_n(\omega, \gamma_0) \cdot T_n(y) \quad (3.7)$$

with the elastic and viscous CHEBYSHEV coefficients e_n and v_n and $x = \gamma/\gamma_0$ and $y = \dot{\gamma}/\dot{\gamma}_0$ to provide the orthogonality. $\dot{\gamma}_0$ herein is defined as the imposed shear rate. Furthermore, new non-linear moduli G'_M and G'_L and viscosities η'_M and η'_L were introduced and are defined as¹⁰⁵

$$G'_M \equiv \left. \frac{d\sigma}{d\gamma} \right|_{\gamma=0} \approx e_1 - 3e_3 + 5e_5 - 7e_7 + \dots \quad (3.8)$$

and

$$G'_L \equiv \left. \frac{d\sigma}{d\gamma} \right|_{\gamma=\pm\gamma_0} \approx e_1 + e_3 + e_5 + \dots \quad (3.9)$$

The respective dynamic viscosities are obtained by

$$\eta'_M \equiv \left. \frac{d\sigma}{d\dot{\gamma}} \right|_{\dot{\gamma}=0} \approx v_1 - 3v_3 + 5v_5 - 7v_7 + \dots \quad (3.10)$$

and

$$\eta'_L \equiv \left. \frac{d\sigma}{d\dot{\gamma}} \right|_{\dot{\gamma}=\pm\dot{\gamma}_0} \approx v_1 + v_3 + v_5 + \dots \quad (3.11)$$

The non-linear stress response can also be depicted geometrically, *e.g.* by plotting the total stress response as function of the strain or of the strain rate, respectively. These so-called LIS-SAJOUS-BOWDITCH plots allow visualizing the non-linear moduli (Figure 3.15).

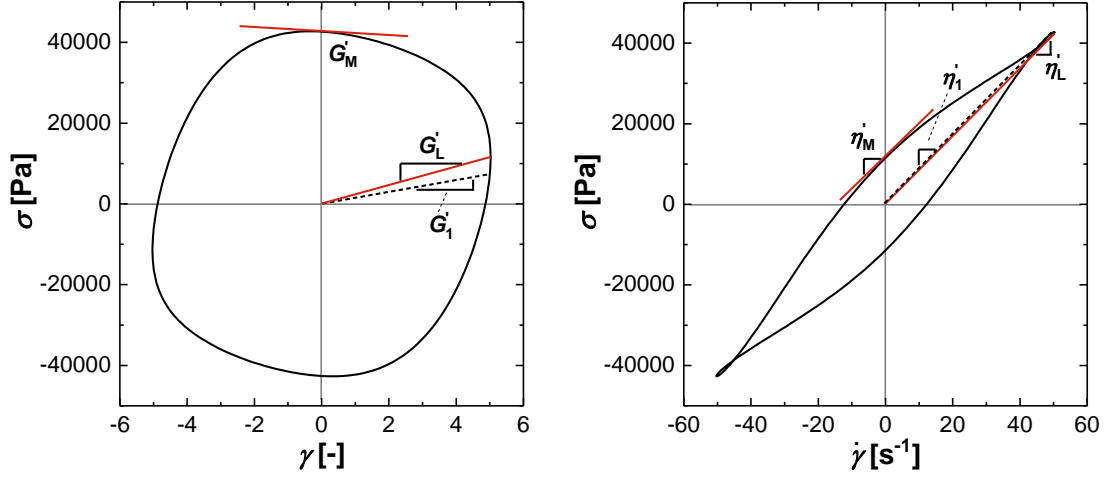


Figure 3.15 Geometric interpretation of the non-linear elastic moduli (left) G'_L and G'_M and the dynamic viscosities (right) η'_L and η'_M for a PPC melt at 140 °C ($f_{\text{carb}} = 92$ mol%, $M_w = 110$ kg/mol). G'_1 and η'_1 are defined as the first elastic modulus and the first dynamic viscosity.

The slope of the tangent at minimum strain ($\gamma = 0$) is defined as the minimum strain modulus G'_M and the minimum strain viscosity η'_{Mv} respectively. Analogously, the large strain modulus G'_L and the large strain viscosity η'_L can be obtained by the secant at maximum strain ($\gamma = \gamma_0$).¹⁰⁵ At small deformations the non-linear moduli converge to their linear counterparts.

An alternative analysis of the non-linear stress response relies on a FOURIER transformation of the response signal (FT rheology). By performing a FT, the non-sinusoidal stress response is transferred into a frequency dependent FT-spectrum showing intensities of the excitation angular frequency and higher order harmonics I_n (Figure 3.16). The stress response is thus expressed as a FOURIER series with the FOURIER coefficients G'_n and G''_n .

$$\sigma(t) = \gamma_0 \sum_{n, \text{odd}} G'_n (\sin n \cdot \omega t) + G''_n (\omega_1 \cdot \cos(n \cdot \omega t)) \quad (3.12)$$

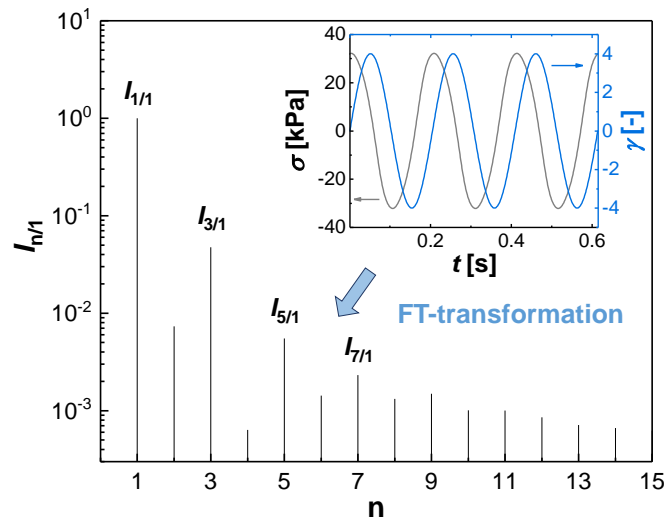


Figure 3.16 FT of the distorted wave function into a FOURIER spectrum showing the relative intensity $I_{n/1}$ of normalized harmonics ω/ω_1 . Excitation angular frequency $\omega_1 = 6.31$ rad/s, strain $\gamma_0 = 398$ %.

The intensities of the corresponding harmonics can be obtained from the FOURIER coefficients using Equation 3.13

$$I_n = \sqrt{G_n'^2 + G_n''^2} \quad (3.13)$$

As a measure for the non-linearity, the intensity normalized third harmonic $I_{3/1}$ was introduced.¹⁰⁶ Alternatively, a zero-shear non-linearity can be defined as

$${}^nQ_0 = \lim_{\dot{\gamma}_0 \rightarrow 0} {}^nQ \quad \text{with } {}^nQ = \frac{I_{n/1}}{\dot{\gamma}_0^{n-1}} \quad (3.14)$$

The intrinsic non-linearity 3Q_0 shows a characteristic frequency dependence which allows to identify branching.¹⁰⁷

Understanding of the non-linear rheological phenomena observed under LAOS conditions is crucial, as most thermoplastic processing operations, such as extrusion, injection molding, film blowing, etc. are performed under large strain amplitudes and/or high frequencies (Figure 3.17).

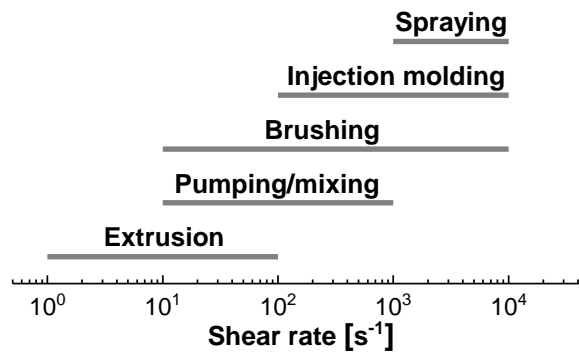


Figure 3.17 Typical shear rates of relevant processing operations.¹⁰⁸

4 SCOPE OF THESIS

The aim of this thesis was to extend the understanding of the heterogeneous-catalyzed copolymerization of PO and CO₂. Additionally, a process should be proposed that allows tailoring the final product properties. The first part of the reported results in this thesis concerns the polymerization process; it is characterized by identification of relevant process parameters in terms of catalyst and product performance (Chapter 5.1). Based on this knowledge, a polymerization procedure is developed that enhances the thermal stability of PPC (Chapter 5.2) and one that allows to tailor its thermal properties (Chapter 5.3). The rheological behavior of these products was studied under processing-relevant conditions, an account is given in Chapter 5.4.

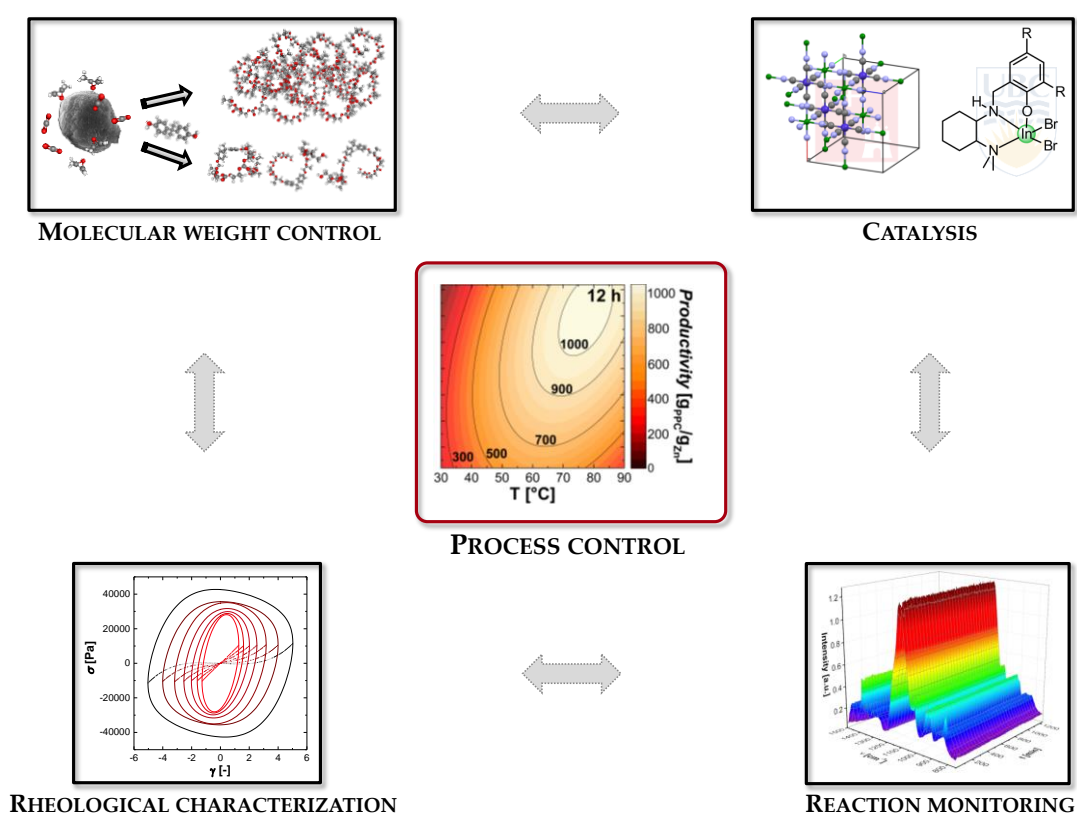


Figure 4.1 Schematic representation of the scope of this thesis.

The synthesis of two types of catalysts and their activity for the PO homopolymerization and copolymerization with CO₂ is reported in Chapter 5.5 and 5.6. The reactions are monitored *online* to derive kinetic parameter of the transformations.

5 RESULTS AND DISCUSSION

5.1 Reaction control and process optimization of PO/CO₂ copolymerizations

Parts of the results of the following chapter were published as original manuscript in *RSC Catalysis Science and Technology* (2017), 7, pp. 2897 – 2905. The online version can be found under <https://pubs.rsc.org/en/content/articlelanding/2017/cy/c7cy00383h> (last accessed 18.02.2019)

The thermal and mechanical properties of PPC depend significantly on its molecular weight as well as the composition of the polymer backbone with regard to carbonate vs ether linkages. The glass transition temperature may range from about 45 °C for the perfectly alternating copolymer to almost -70 °C for poly(propylene glycol).¹⁰⁹ The mechanical properties change accordingly.¹⁷ Therefore, a precise control of the polymerization process is necessary to obtain polymers with defined material properties. The nature of the utilized catalyst and the polymerization conditions, *i.e.* the reaction temperature, the pressure and the reaction time influence the resulting product distribution and the polymer composition as well as the catalyst's performance itself. Several research groups have investigated this influence regarding the polymer yield and the fraction of carbonate linkages in the polymer backbone. SOGA and TAN for instance studied the temperature dependence and the effect of the monomer composition for diethylzinc-based catalyst systems.^{110,111} Other groups reported on the temperature, pressure and time dependence as well as the impact of the catalyst concentration and solvents on the copolymerization catalyzed by zinc dicarboxylates.^{109,112–116} These reports follow the “one factor at a time” approach and, thus, find their limitations in the prediction of the polymer yield, its composition or the molecular weight distribution under arbitrary reaction conditions. In contrast, the design of experiments (DOE) approach allows obtaining highest informative gain with least possible experimental effort (Figure 5.1).

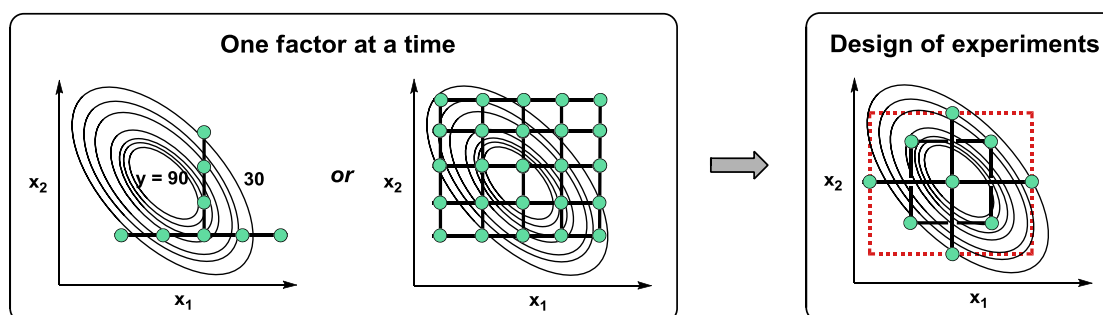


Figure 5.1 One factor at a time approach (left) versus design of experiments (DOE, right). DOE gives high informative output, while minimizing the number of experimental runs.

The following chapter represents a comprehensive study on the catalytic performance of nanoscopic ZnGA with regard to the catalyst's productivity (turnover number, TON), the polymer composition as well as the products molecular weight distribution as function of typical reaction parameters (T , p and t). With emphasis on a potential industrial-scale application of

zinc dicarboxylate catalysts, the copolymerization in solvents was not considered. Performing the PO/CO₂-copolymerization in bulk has the benefit that no organic solvents are utilized that need to be removed subsequently.

The catalyst's performance and the polymer composition were studied in a preset parameter space. The space comprises a low and high temperature (30 – 90 °C) and a low and high pressure (0.6 – 4.1 MPa) in a normal range, where the copolymerization is known to proceed and can be handled in standard pressure equipment. Virtually no polymer formation is observed at temperatures below 30 °C. At temperatures above 90 °C, the depolymerization to yield cPC is substantial. The data evaluation thus would lead to larger uncertainties. The axial points in the applied design were chosen as face centered meaning that "low" equals $-\alpha$ and "high" $+\alpha$. The resulting design matrix with the catalyst's productivity, the fraction of carbonate linkages (f_{carb}) and the number average and weight average molecular weight (M_n , M_w) is displayed in Table 5.1.

Table 5.1 Design matrix of experimental results utilized for model analysis. The repeated center points are highlighted.

Entry	T [°C]	p [MPa]	t [h]	TOF ^a [h ⁻¹]	TON ^b [-]	f_{carb} ^c [mol%]	M_n ^d [kg/mol]	M_w ^d [kg/mol]
1	30	0.6	2	25	51	57.7	11	61
2	90	0.6	2	70	140	24.4	17	117
3	30	4.1	2	0	0	46.6	n.d. ^e	n.d. ^e
4	90	4.1	2	277	555	82.0	70	195
5	60	2.35	2	217	435	88.4	72	367
6	60	0.6	7	56	391	75.3	51	229
7	30	2.35	7	19	133	84.4	24	221
8	60	2.35	7	99	693	89.8	96	370
9	60	2.35	7	101	710	89.3	89	372
10	60	2.35	7	101	709	90.2	92	364
11	60	2.35	7	96	674	90.2	100	362
12	90	2.35	7	96	671	75.8	58	109
13	60	4.1	7	105	734	91.6	95	401
14	30	0.6	12	23	282	90.7	44	171
15	90	0.6	12	20	240	27.0	27	108
16	30	4.1	12	71	872	79.9	7.2	235
17	90	4.1	12	7	82	83.2	55	153
18	60	2.35	12	71	847	90.4	99	357

Experiments were performed using the standard protocol for PO/CO₂ copolymerizations. Reaction conditions: V(PO) = 50 mL, m(ZnGA) = 137.5 mg. ^a in [g_{PPC}/(g_{Zn} · h)], ^b in [g_{PPC}/g_{Zn}], ^c Determined by ¹H-NMR spectroscopy, ^d determined by SEC in THF against PS-standards, ^e not determined.

The design of experiments, the calculation of empirical response surfaces as well as their evaluation were performed using Design Expert 9 (Stat-Easy, Inc.). By multiple regression analysis, correlations between input and output variables were empirically evaluated. The outcome enables the prediction of certain properties under set reaction conditions. An analysis of variances (ANOVA) was conducted to determine the statistical significance of the model

parameters. Parameters with p-values below 0.05 are considered as statistically significant. Initially, a 2-level-factorial design with 12 runs (4 center points) was chosen. However, evaluation of the results indicated a cross dependence of the individual parameters. It was therefore necessary to introduce higher terms in the model equation. To account for quadratic interactions, a central-composite design was applied (Table 5.1). This design was obtained by introducing axial points resulting in a total of 18 experimental runs including 4 center points. In addition, a series of experiments was conducted (Table 5.2) to evaluate the prediction accuracy of the calculated prediction models (Chapter 5.1.1 and 5.1.2).

Table 5.2 Experimental runs for model evaluation.

En-try	T [°C]	p [MPa]	TOF ^a [h ⁻¹]	TON ^b [-]	f_{carb} ^c [mol%]
1	60	2.35	135	540	90.1
2	90	4.1	179	715	82.7
3	90	0.6	42	169	14.6
4	60	0.6	82	328	74.5
5	60	4.1	149	595	92.6
6	90	2.35	145	578	77.5

Experiments were performed using the standard protocol for PO/CO₂ copolymerizations. Reaction conditions: V(PO) = 50 mL, m(ZnGA) = 137.5 mg, $t = 4$ h. ^a in [g_{Polymer}/(g_{Zn} · h)], ^b in [g_{PPC}/g_{Zn}], ^c Determined by ¹H-NMR spectroscopy.

For all model analyses a BOX-COX power transformation was performed (Equation 5.1) to minimize the residual sum of squares.

$$y' = \begin{cases} y^\lambda & , \lambda \neq 0 \\ \ln(y) & , \lambda = 0 \end{cases} \quad (5.1)$$

This data transformation is utilized to account for the results heteroscedasticity, *i.e.* the standard deviation is not constant but has the tendency to increase as the response values increase.

5.1.1 Catalyst productivity

The catalyst productivity (TON) is expressed as the amount of polymer obtained per gram of zinc ions. Evaluation of the data using the BOX-COX power transformation (Figure 5.2) yields 0.59 as the best value for λ . Therefore, a square root transformation was applied for model analysis. Further evaluation of the obtained results gives a quadratic response surface model, *i.e.* a model containing single and quadratic terms based on the reaction time and a cross dependence of temperature and pressure (Equation 5.2).

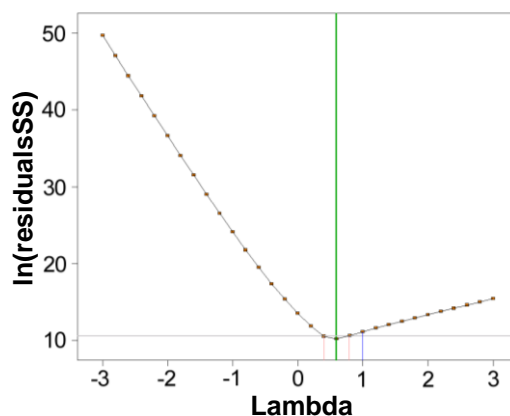


Figure 5.2 Box-Cox plot for the empirical model for the catalyst's productivity. An ideal value for λ of 0.59 is determined.

$$\sqrt{\text{TON}} = a_0 + a_1 \cdot T + a_2 \cdot p + a_3 \cdot t + a_4 \cdot T \cdot p + a_5 \cdot T^2 + a_6 \cdot p^2 \quad (5.2)$$

Terms $a_{0 \rightarrow 6}$ in the resulting empirical prediction model for the productivity show probability values (p-values) of 0.05 or less (Table 5.3) and are thus considered to be of statistical significance. The model coefficients are displayed for normalized values (from [-1] to [+1]; coded), and for the corresponding physical values. The coded form allows comparing the relative impact (negative and positive) of factors on the response surface, *e.g.* the TON. The largest impact on the catalyst's TON is resulting from the reaction temperature T . The quadratic interactions and the cross term of T and p may be correlated to the molar ratio of CO_2 in the feed $x(\text{CO}_2)$ being a function of both.¹¹⁷ The model accuracy can be displayed by plotting the actual vs predicted values (Figure 5.3).

Table 5.3 Probability values (p-values) for the statistically significant terms and model coefficients in the coded [-1/+1] and actual form for the description of the catalyst's productivity.

Parameter	p-value	Coefficient	Coded	Physical
Model	< 0.0001	a_0	26.1	-19.5
T	< 0.0001	a_1 [$^{\circ}\text{C}^{-1}$]	6.13	1.08
p	0.0036	a_2 [MPa^{-1}]	1.87	0.73
t	< 0.0001	a_3 [h^{-1}]	3.61	0.72
$T \cdot p$	< 0.0001	a_4 [$^{\circ}\text{C}^{-1} \cdot \text{MPa}^{-1}$]	5.02	0.10
T^2	< 0.0001	a_5 [$^{\circ}\text{C}^{-2}$]	-8.24	0.01
p^2	0.0027	a_6 [MPa^{-2}]	-3.52	-1.15
$R^2 = 0.98$				

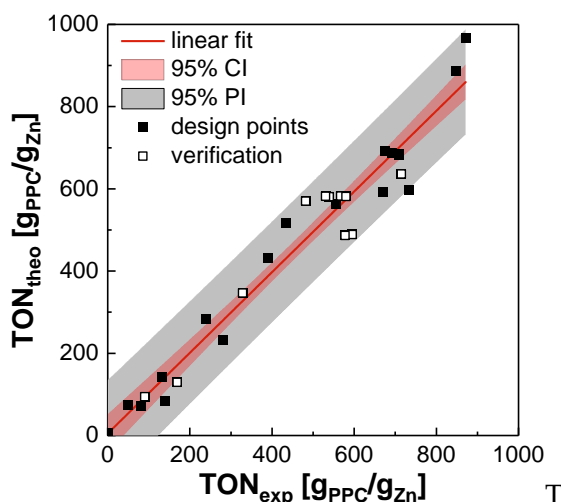


Figure 5.3 Actual vs predicted catalyst TON. The red and the grey band correspond to the 95 % confidence (CI) and prediction interval (PI).

The catalyst productivity can be displayed as a hyperbolic response surface as function of p and T at various reaction times t (Figure 5.4). The contour plots show that maximum TON are observed at temperatures between 70 – 80 °C and pressures between 3.5 and 4.1 MPa, in agreement with previous studies.^{112,114} This observation is valid regardless of the reaction time.

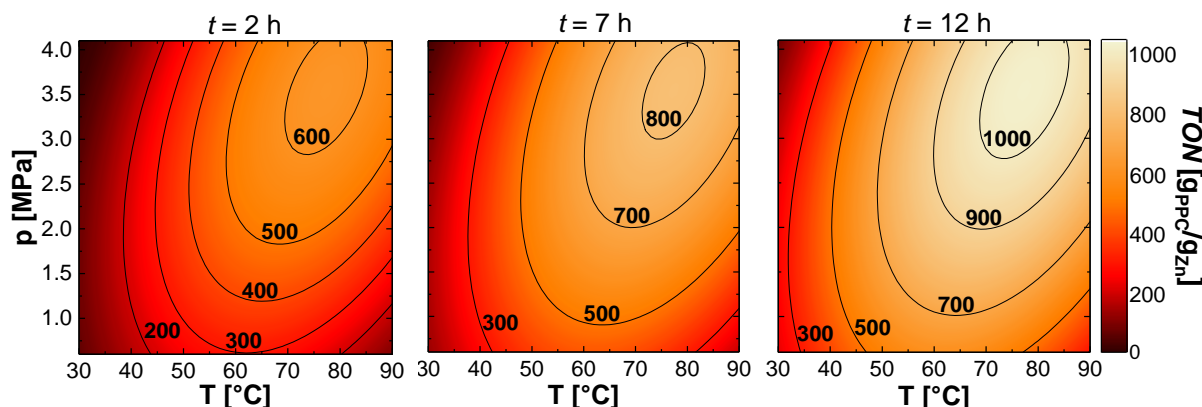


Figure 5.4 Contour plots for the productivity of the ZnGA catalyzed CO₂/PO-copolymerization in dependence on the reaction temperature, the pressure after 2 h, 7 h and 12 h (from left to right).

PO and CO₂ are competing for binding at the surface, thus indicating that simultaneous adsorption of both monomers on the catalysts surface is of relevance for chain growth. Higher CO₂-contents in the feed, *e.g.* at lower reaction temperatures and/or higher pressures, impede the adsorption of PO and consequently result in lower polymer yields. For the same reason, the polymer yield also drops rapidly at high temperatures and low pressures.

It may also be concluded from Figure 5.4 that the catalyst's activity, *i.e.* the turnover frequency (TOF), decreases with the time of reaction. The yield increases less than linear with the reaction time. This also correlates to the PO conversion. The decrease in polymerization rate over time can be taken from the rate of CO₂ consumption (Figure 5.5). For instance, a significant drop in the CO₂-uptake rate is found after approximately 3 hours of reaction time ($T = 60$ °C, $p = 2.35$ MPa), corresponding to a PO conversion of ~35 %. From there on, the rate of CO₂

conversion proceeds again linearly with a reduced slope, *i.e.* a declined polymerization rate. Latter rate remains unchanged leading to PO conversions of about 60 % after 12 h. The decrease in TOF is interpreted in terms of the monomers experiencing a relevant diffusion barrier to reach the surface. The initial CO₂ uptake (≈ 1200 mL) corresponds to the saturation of the PO liquid phase and the reactor gas phase. It is noteworthy that the measured values for the CO₂ uptake do not directly represent the rate of polymerization. The consumption of PO leads to a decrease of the liquid phase and as a result liberation of CO₂ from the liquid phase.¹¹⁸

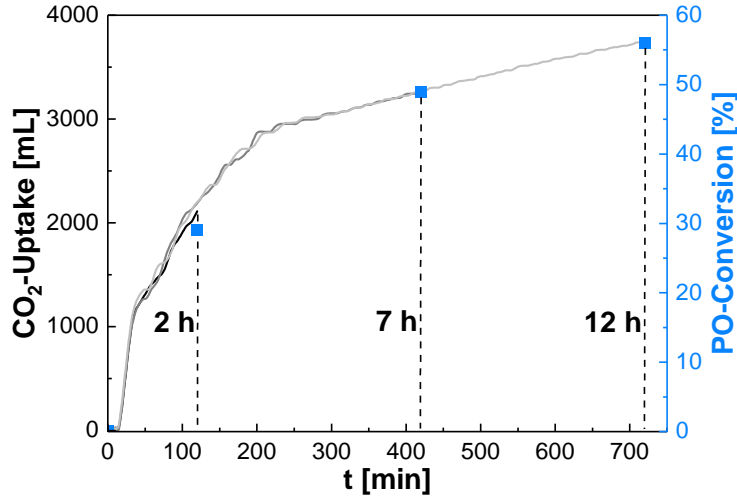


Figure 5.5 Total CO₂-uptake and conversion of PO in dependence of the reaction time (Table 5.1 entries 5, 10, 18). Reactions conditions: $T = 60$ °C, $p = 2.35$ MPa.

Partial differentiation of the TON (Equation 5.2) with respect to the reaction pressure p at constant reaction temperatures T and times t leads to an expression that is time-independent (Equation 5.3).

$$\left(\frac{\partial \sqrt{\text{TON}}}{\partial p} \right)_{T,t} = a_2 + a_4 \cdot T + 2a_6 \cdot p \quad (5.3)$$

The maximum polymerization rate, *i.e.* where the derivative is zero, is a linear function of T and p . The pressure at the maximum TON correlates linearly with the reaction temperature. To gain further insights, the molar composition of the liquid phase $x(\text{CO}_2)$ was calculated from the solubility data of CO₂ in PO¹¹⁷ using the PENG-ROBINSON equation of state (Equation 5.4),

$$p = \frac{RT}{V_m - b} - \frac{a(T)}{V_m(V_m - b) + b(V_m - b)} \quad (5.4)$$

with V_m representing the molar volume of the mixture, and, $a(T)$ and b being constants derived from the critical properties of the reactants (Figure 5.6).¹¹⁹

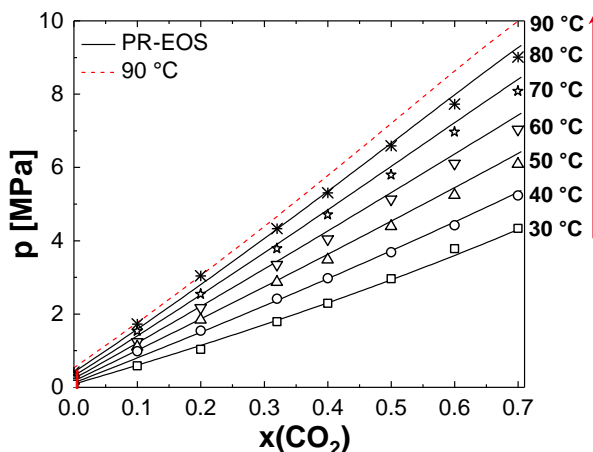


Figure 5.6 CO₂-solubility data in PO at temperatures between 30 and 80 °C.¹¹⁷ The red dots display the vapor pressure of neat PO, *i.e.* the pressure at $x(\text{CO}_2) = 0$.¹²⁰ The mole fraction of CO₂ under the specific reaction conditions was obtained solving the PENG-ROBINSON equation of state (PR-EOS). The dotted red line displays the extrapolated $x(\text{CO}_2)$ at 90 °C.

When plotting $x(\text{CO}_2)$ at maximum productivity, the highest TON are observed at $x(\text{CO}_2) = 0.27 (\pm 0.01)$ regardless of T (Figure 5.7). This indicates that at a ratio of CO₂ to PO of about 1 to 3 in the feed, the catalyst's surface contains the optimum concentrations of both reactants for copolymer formation by an almost alternating insertion. Neither the insertion of PO, nor of CO₂ into a growing chain end appear to be dominantly rate-limiting under these conditions.⁴⁷ It can be concluded that the ring-opening of PO has a higher activation energy than the insertion of CO₂.⁶¹

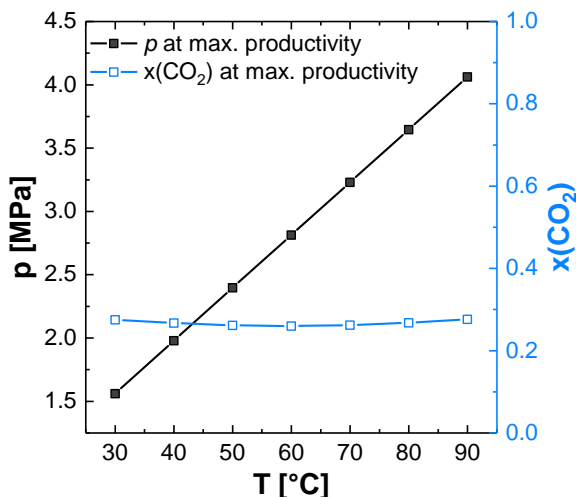


Figure 5.7 Total pressure and mole fraction of CO₂ of maximum productivity calculated using Equation 5.3. The molar fraction of CO₂ in the liquid phase $x(\text{CO}_2)$ is determined using Equation 5.4.

5.1.2 Polymer composition

The polymer composition was analyzed in analogy to the catalyst's productivity using the same type of multiple linear regression. The copolymer composition is expressed in terms of the content of carbonate linkages f_{carb} . The composition is limited from $f_{\text{carb}} = 0$ for the PO

homopolymer to $f_{\text{carb}} = 100$ for perfectly alternating PPC. These constraints enable the application of a logit-transformation for model calculation (Equation 5.5).

$$\text{Logit}(f_{\text{carb}}) = \ln\left(\frac{f_{\text{carb}} + \text{lower}}{\text{upper} - f_{\text{carb}}}\right) = \beta \quad (5.5)$$

The terms “lower” and “upper” correspond to the lowest (0) and highest possible carbonate content (100), respectively. A quadratic regression model was applied to account for quadratic interaction terms. The ANOVA gives access to the significant factors that were utilized for the final model generation. Table 5.4 displays the results of the variance analysis, *i.e.* p-values of the specific factors as well as the corresponding model coefficients $a_{0 \rightarrow 7}$. The results show, that the composition strongly depends on the pressure p and, thus, on the CO₂-concentration in solution.^{109,113,114,116} The carbonate content f_{carb} of PPC synthesized using nanoscopic ZnGA as a catalyst can be expressed by Equation 5.6

$$f_{\text{carb}} = \frac{100 \cdot e^{\beta}}{1 + e^{\beta}} \quad (5.6)$$

with

$$\beta = a_0 + a_1 \cdot T + a_2 \cdot p + a_3 \cdot t + a_4 \cdot T \cdot p + a_5 \cdot T \cdot t + a_6 \cdot T^2 + a_7 \cdot p^2 \quad (5.7)$$

and the coefficients $a_{0 \rightarrow 7}$ listed in Table 5.4.

Table 5.4 Probability values for the statistically significant terms and model coefficients in the coded [-1/+1] and actual form for the description of the carbonate content.

Parameter	p-value	Coefficient	Coded	Physical
Model	< 0.0001	a_0	2.22	-2.23
T	0.0005	a_1 [°C ⁻¹]	-0.34	0.10
p	< 0.0001	a_2 [MPa ⁻¹]	0.52	0.30
t	0.0002	a_3 [h ⁻¹]	0.39	0.24
$T \cdot p$	< 0.0001	a_4 [°C ⁻¹ · MPa ⁻¹]	0.82	0.02
$T \cdot t$	0.0003	a_5 [°C ⁻¹ · h ⁻¹]	-0.41	-0.003
T^2	< 0.0001	a_6 [°C ⁻²]	-0.96	-0.001
p^2	0.0004	a_7 [MPa ⁻²]	-0.65	-0.20
$R^2 = 0.98$				

The time and temperature dependence of f_{carb} at various reaction pressures is displayed in Figure 5.8. The amount of CO₂ incorporated depends linearly on T and p and in terms of their cross and quadratic interaction contributions for the same reasons as stated in Chapter 5.1.1.¹¹⁷ The contour plots indicate that the catalyst’s selectivity can be tailored to yield PPC with a preset composition (along Equation 5.7).

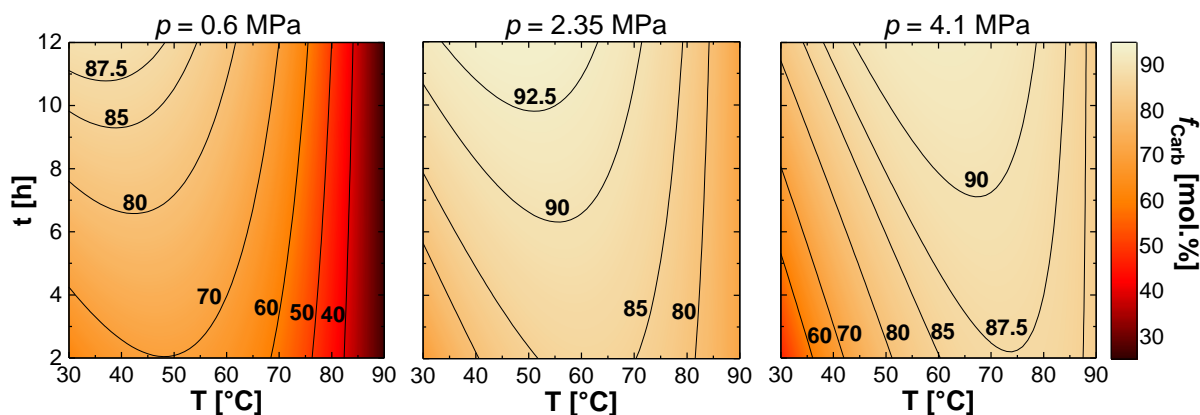


Figure 5.8 Contour plots for the carbonate content f_{carb} of PPC synthesized by the ZnGA mediated CO_2/PO -copolymerization in dependence on the reaction temperature and time as well as the pressure. The carbonate content is expressed in mol% of the linkages between PO entities.

Setting of the reaction conditions enables to tune the polymer composition between 25 and 93 mol% carbonate linkages. Changing the polymer composition has an impact on the resulting material properties, *e.g.* the glass transition temperature T_g . Table 5.5 displays the T_g of PPC with various carbonate contents, synthesized in this study.

Table 5.5 Thermal properties of PPC with various carbonate contents (f_{carb}).

f_{carb} [mol%] ^a	T_g [°C] ^b
24.4	-63.6
75.3	20.8
91.6	35.1

^a Determined by $^1\text{H-NMR}$, ^b determined by DSC.

The presence of ether-blocks in the ZnGA mediated copolymerization leads to a substantial decrease in T_g . This enables to tailor the resulting material properties.²¹ The highest observed carbonate content in the investigated parameter space ($f_{\text{carb}} = 93$ mol%) is obtained at moderate temperatures of approximately 60 °C and pressures between 3.0 and 4.0 MPa. Carbonate fractions down to 25 mol% are observed at low concentrations of CO_2 in PO solution, *i.e.* at high temperatures and/or low pressures. The low carbonate content may result from the competitive PO insertion into intermediate zinc alkoxide chain ends. However, the reaction mechanism of the ZnGA catalyzed copolymerization remains unknown.

The highest carbonate content at a given temperature is obtained at $x(\text{CO}_2) = 0.30 (\pm 0.02)$, similar to the catalyst's productivity. Partial differentiation of β (Equation 5.7) at constant reaction temperatures and times allows to determine the pressures at which maximum content of carbonate linkages is achieved (Figure 5.9).

$$\left(\frac{\partial \text{Logit}(\beta)}{\partial p} \right)_{T,t} = a_2 + a_4 \cdot T + 2a_7 \cdot p \quad (5.8)$$

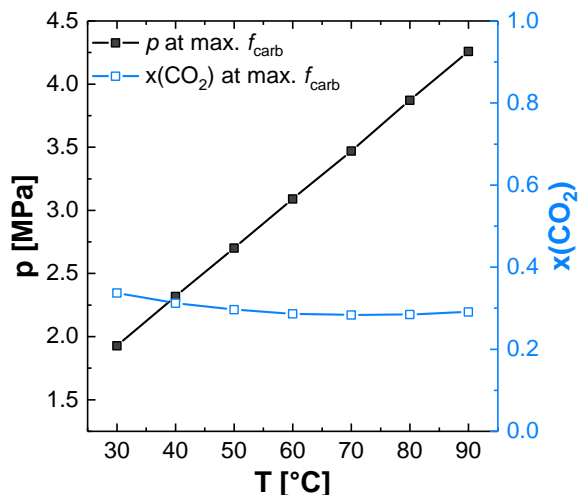


Figure 5.9 Total p and $x(\text{CO}_2)$ for maximum carbonate contents at a specific reaction temperature. Maxima were determined using the first deviation of Equation 5.7.

Increasing or decreasing the PO/CO₂ ratio results in reduced polymerization rates and carbonate contents. This again is consistent with a heterogeneous catalytic system, wherein the rates are proportional to the surface coverage.¹²¹ Lower CO₂-concentrations lead to lower concentrations of the most reactive, *i.e.* the carbonate chain end. Higher concentrations of CO₂ in contrast lead to lower concentrations of PO on the surface and consequently lower overall rates. This implies a change in a pre-equilibrium on the catalyst's surface.

To evaluate the accuracy of the obtained empirical model, the theoretical values for f_{carb} were compared with the experimentally determined values (Figure 5.10). The plot shows an excellent prediction accuracy over the entire composition range.

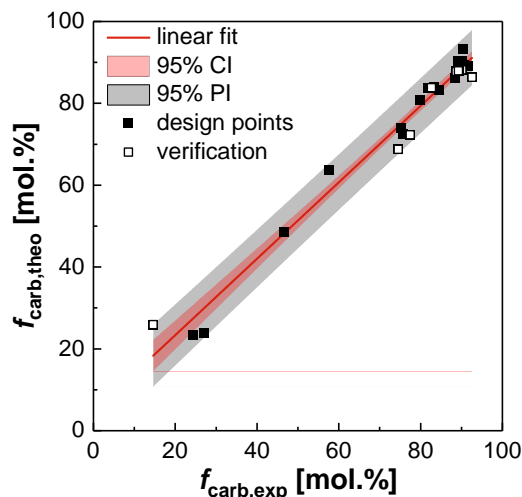


Figure 5.10 Experimentally determined vs predicted f_{carb} . The red and the grey band correspond to the 95 % confidence (CI) and prediction interval (PI).

Knowledge based on empirical prediction models allows the determination of a process window wherein certain requirements are likely to be fulfilled. Figure 5.11 displays an example of such a process window where the polymerization process is stable in the sense that the

minimum target TOF of $180 \text{ g}_{\text{PPC}}/\text{g}_{\text{Zn}} \cdot \text{h}$ and the minimum f_{carb} of 90 mol% are achieved even upon smaller deviation in the process conditions (yellow area).

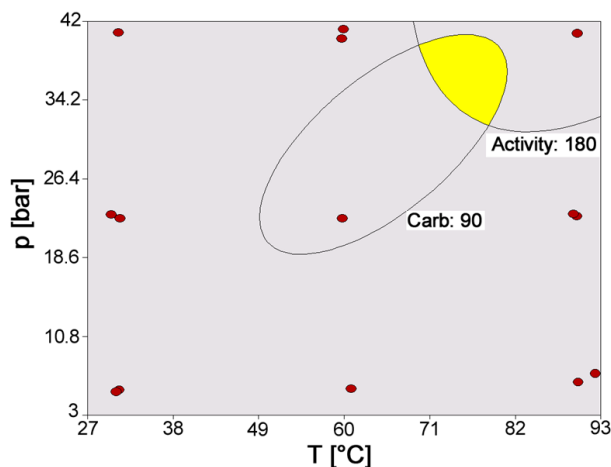


Figure 5.11 Exemplary process window for the ZnGA-mediated PO/CO₂-copolymerization. Within the yellow area, carbonate contents higher than 90 mol% and catalytic activities above $180 \text{ g}_{\text{PPC}}/\text{g}_{\text{Zn}} \cdot \text{h}$ are achieved.

5.1.3 Molecular weight

The copolymerization of PO and CO₂ mediated by ZnGA initially proceeds in a pseudo-living way, in the sense that the molecular weight increases steadily with PO conversion. Latter is revealed by plotting the number average molecular weight M_n of the product against the PO-conversion (Figure 5.12). This feature is well-known for the PO/CO₂-copolymerization using metallo-porphyrins^{38,122} or salen^{50,123,124} complexes, however remained unnoticed for ZnGA catalysts, yet.⁵⁹ The polydispersity index (PDI) has values above 6 at low conversions and approaches a value of approximately 2 towards complete monomer consumption. The higher PDI at early reaction stages indicates a slow initiation reaction relative to the chain growth. This feature displays the complex mechanism of heterogeneous catalysts for the CO₂/PO-copolymerization possibly involving multiple active sites.

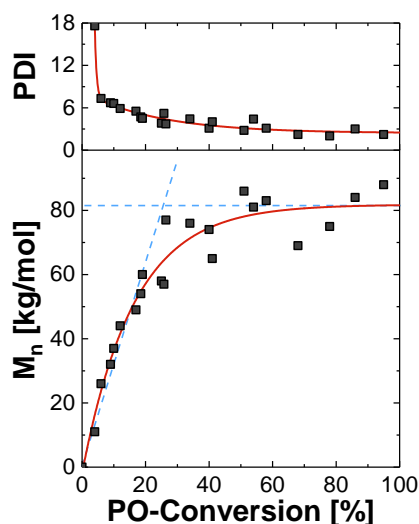


Figure 5.12 Polydispersity indices (PDI) and number average molecular weight M_n in dependence on the PO-conversion at 60 °C and 3.1 MPa. Linear correlation between M_n and the monomer conversion and the threshold in the molecular weight at higher conversions > 25 % are indicated by dashed lines. The experiments were performed in collaboration with RAHLF and NÖRNBERG.^{63,67}

The molecular mass increases linearly with the PO conversion to about 20 – 25 % to a value of $M_n = 80$ kg/mol. Concomitantly, the PDI decreases to a value of about 2. The molecular mass does not increase after reaching that state of conversion. Latter can be rationalized by assuming that the dynamic of active chain ends becomes restrained. PO and CO₂-conversion from here on seems to proceed with an additional barrier leading to a decrease in polymerization rate as was observed. The molecular mass of the products that are formed at this stage again reach the level of about 80 kg/mol before growth subsides. These products seem to result from an additional chain starter that is either formed from an inactive chain end (by reactions with impurities in the system or from an elimination reaction) or from the catalyst surface after fractionation of the catalyst particles leading to accessible sites. The catalyst does not seem to deactivate over time in that regard.

5.2 Enhancement of thermal stability of PPC

Despite some benefits of PPC, its application has been limited to niche markets.^{15,20} One of the main reasons for this is its poor thermal performance, *i.e.* the rapid degradation at elevated temperatures accompanied with the formation of volatile decomposition products such as cPC. The cyclic carbonate may be considered as volatile, despite its high boiling point of 240 °C, because it can migrate to the polymers surface and thereby may get into contact with end users. The extent of decomposition depends on the temperature and duration of the treatment as well as on net shear forces.¹²⁵ In addition, the presence of impurities and catalyst residues affects the stability.⁷⁹ Moreover, the constitution of the sample itself, *i.e.* the carbonate content and the molecular weight have an impact on the decomposition. For instance, it was shown, that the thermal stability can be enhanced by incorporation of ether-linkages into the polymer backbone.¹⁷

In this chapter an advanced processing strategy is presented that allows transferring unstable chain ends of PPC to ether-rich blocks that inhibit the backbiting reaction to cPC. This comprises a process intensification as there is no need for a post-polymerization modification, also excluding the addition of capping agents. A prerequisite for the formation of ether-rich blocks is the possibility to tune the catalysts selectivity regarding CO₂ incorporation. State of the art Co(salen) catalysts are ineligible for this task as they yield almost perfectly alternating PPC even at low CO₂ pressures.¹²⁶ In contrast, ZnGA and DMC catalysts allow to change the selectivity for PO over CO₂ as function of the reaction conditions (Chapter 5.1 and 5.6).¹²⁷ The use of zinc dicarboxylate catalysts is preferred in this context as they combine high activities with a simple preparation from inexpensive and non-toxic components.^{13,15,66,128}

To enhance the thermal stability of PPC, an *in-situ* ether-capping was performed. The ether-capping is achieved by introduction of a second reaction stage at higher temperatures and/or lower partial pressures of CO₂. In a first polymerization step PPC is produced using a standard reaction protocol ($T = 60\text{ °C}$, $p = 30\text{ bar}$, $t = 4\text{ h}$). By reducing the CO₂-concentration in the second polymerization stage, the surface coverage of ZnGA with monomers changes, which results in a change in catalyst selectivity with respect to PO incorporation (Figure 5.13). The living nature of the ZnGA-mediated copolymerization implies that all chains continue growing.¹²⁷ As a result, the newly formed chain end segments have a different composition than the main chain with respect to carbonate vs ether linkages. Depending on the initiating species, BAB and/or AB block-polymers are obtained (B: ether-rich; A: carbonate-rich).

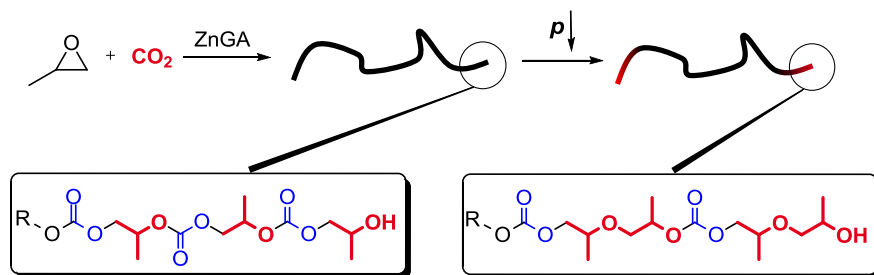


Figure 5.13 Schematic pathway of the *in-situ* capping of unstable carbonate-rich chain ends with ether-rich blocks by introduction of a second polymerization stage.

The change of the chain composition is difficult to monitor directly as the chain end itself only makes up a small part. A small NMR signature is detectable in comparison with a reference sample: the ^1H -NMR of “PO-capped” PPC shows increased signals for carb-ether, ether-carb and ether-ether spin systems (Figure 5.14). This increase is attributed to the enhanced incorporation of PO leading to the formation of more ether-linkages in the second polymerization step.

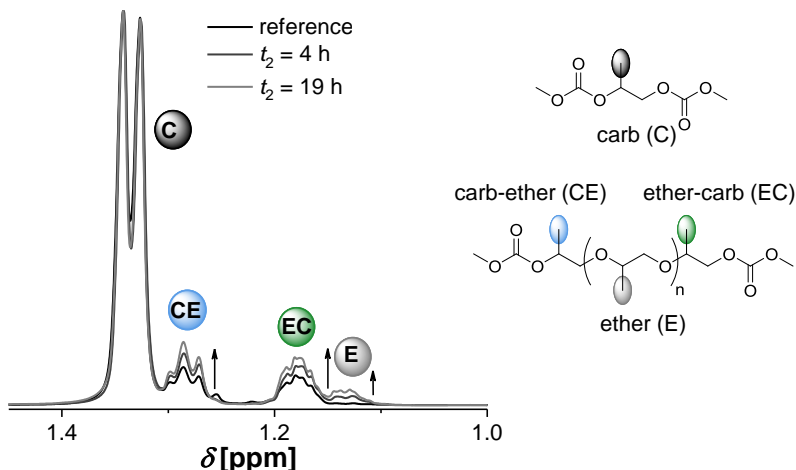


Figure 5.14 ^1H -NMR spectra of untreated PPC and ether-capped samples. Reaction conditions: $T_2 = 60\text{ }^\circ\text{C}$, $p_2 = 5\text{ bar}$. The signal at 1.33 ppm corresponds to the carbonate linkage (carb, C). Signals at 1.28, 1.18 and 1.12 ppm are assigned to carb-ether (CE), ether-carb (EC) and ether (E) repetition units, respectively.

The on-going product formation in the second polymerization stage is displayed by increased yields compared to the reference copolymerization without the additional capping step (Table 5.6, entry 1). Assuming that no termination reactions occur, this means that the active chain ends are capped with newly formed (ether-enriched) segments. However, the detailed mechanism of the ZnGA mediated PO/ CO_2 copolymerization remains unknown, *i.e.* the product yield would also increase in case of new chain initiation. In latter case, the thermal stability of the already formed chains would remain unaffected.

Lower CO_2 -concentration results in an increased formation of cPC during the second polymerization stage. This observation is in agreement with previous literature.¹¹⁶ For Cr(salen) complexes it was proposed that lower CO_2 pressures extend the lifetime of alkoxide intermediates that can either directly undergo a backbiting reaction or may be protonated and subsequently

form the cyclic carbonate.^{129,130} This hypothesis requires further elucidation in case of the heterogeneously catalyzed copolymerization.

Table 5.6 *in-situ* ether capping of PPC by introducing a second polymerization stage.

En-try	p_2 [bar]	T_2 [°C]	t_2 [h]	yield [g]	$f_{\text{carb. total}}^a$ [mol%]	$w_{\text{cPC. crude}}^a$ [wt.%]	M_n/M_w^b [kg/mol]	PDI [-]	Thermal stress test 180 °C, 60 min	
									Δw_{cPC}^a [wt.%]	$\Delta M_n/\Delta M_w^b$ [%]
1	-	-	-	25.4	90.8	6.2	25/98	3.9	5.5	20/40
2	2.5	60	4	27.9	86.1	10.4	23/87	3.9	2.7	n.d.
3	2.5	60	19	30.5	82.6	13.5	22/64	2.8	8.0	8.3/19
4	5	60	4	30.6	88.2	8.4	22/92	4.1	0.9	6.2/33
5	5	60	19	36.8	86.6	12.0	25/79	3.1	2.4	7.7/21
6	10	60	4	34.3	89.2	7.8	24/105	4.4	1.3	13/31
7	10	60	19	39.6	89.1	10.0	28/97	3.5	1.8	20/30
8	5	80	4	28.3	82.7	15.2	21/54	2.6	1.4	18/20
9	5	80	19	31.4	65.3	43.6	18/27	1.5	1.7	9.4/9.4
10	10	80	4	28.6	84.8	14.8	22/59	2.6	2.3	19/21
11	10	80	19	36.5	75.5	40.0	20/33	1.6	1.6	11/9.1
12	10	100	2	27.9	78.1	27.8	17/33	2.0	4.0	7.2/10

Experiments were performed using the two-stage reaction protocol for PO/CO₂ copolymerizations. Reaction conditions: $T_1 = 60$ °C, $p_1 = 30$ bar, $t_1 = 4$ h, $V(\text{PO}) = 50$ mL, $m(\text{ZnGA}) = 100$ mg. ^a determined from ¹H-NMR spectra, ^b determined by SEC in THF against PS-standards.

The backbiting also leads to a higher ether content in the B-block to some extent as it proceeds until an ether linkage is reached. Chain ends bearing ether linkages are considered stable as they do not readily undergo backbiting reactions. The formation of cPC during the polymerization is more pronounced at higher T_2 and prolonged reaction times t_2 (Table 5.6).

To determine the thermal stability, CPC-free samples (obtained by precipitation from methanol) were subjected a thermal stress test at 180 °C for 5 – 60 min. The test was performed under argon atmosphere to prevent oxidative degradation. While attempts to continuously monitor the degradation by means of *in-situ* FTIR failed, the thermally aged samples can be analyzed by ¹H-NMR and SEC. The backbiting is observed as the formation of cPC over time, whereas random chain scission results in drastic changes in the molecular weight distribution which can be observed by SEC. As a measure of the thermal stability the difference of the cPC-content prior and after the 60 minutes stress test Δw_{cPC} is determined (Table 5.6).

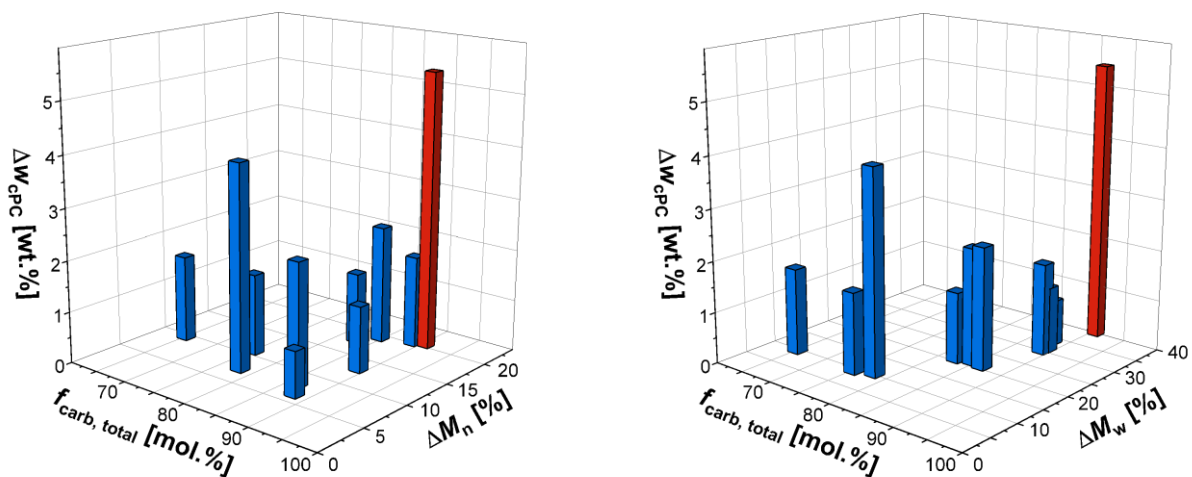


Figure 5.15 Change in w_{cPC} and M_n (left) and M_w (right) after the thermal stress test at 180 °C for 60 min for crude PPC (red) and the products obtained by the two-stage polymerization (blue).

The reference shows an increase in cPC-content of 5.5 wt.% after 60 min at 180 °C: The increase in cPC content in the reference proceeds – most likely – until stable ether chain ends are reached. This process of course also takes place during the second polymerization phase with a lower CO₂ pressure. The extent has not been determined. It is worth noting, that even though the introduction of the second reaction stage results in an increased cPC formation during the reaction, the enhanced thermal stability of the final product (Fig 5.15) is highly desired to prevent potential emission issues caused by cPC. Indeed, a rather similar process is already applied on an industrial scale.¹³¹ Here a low molecular weight poly(ether carbonate) polyol is thermally aged to force cPC formation until all chain ends reach an ether-linkage.

Taking into account the amount of cPC that is formed during the copolymerization, pressures of $p_2 = 5 - 10$ bar and a temperature of $T_2 = 60$ °C (Table 5.6, entries 4 and 6) are considered as optimum reaction conditions for the ether-capping. The so obtained *in-situ* capped PPC possess ether-enriched segments at the chain ends that effectively slow down the thermal depolymerization by backbiting significantly. This allows a thermal processing at elevated temperatures up to 180 °C without the formation of significant amounts of undesired side products.

5.3 Catalytic chain transfer copolymerization of PO and CO₂

The results of the following chapter were published as original manuscript in *ChemistryOpen* (2019), 8, pp. 1 – 13. The online version can be found under <https://onlinelibrary.wiley.com/doi/abs/10.1002/open.201900135> (last accessed 28.06.2019)

The ZnGA-mediated CO₂-epoxide copolymerization gives access to high-molecular weight poly(alkylene carbonates) in excellent yields. However, control over molecular weight may be desirable for certain applications, such as water-based dispersions^{132,133} or as polyol compound in polyurethane manufacturing.^{19–21,134} Regulation of the molecular weight can be reached by the treatment of high-molecular weight products with acids¹³⁵ or alcohols^{135,136} resulting in a controlled polymer degradation. However, such procedures may not be considered industrially viable on account of the need of additional processing steps. The requirement of extensive purification from low-molecular weight products and catalyst residues results in additional manufacturing costs. Alternatively, low-molecular weight polymers can be obtained directly by utilization of chain transfer agents (CTA) during the polymerization reaction. This so-called immortal polymerization is a living-type polymerization that involves a reversible proton-exchange with CTAs to form dormant chains.¹³⁷ Consequently, the overall number of chains increases by the number of CTA-molecules (Figure 5.16). The chain transfer reaction ideally occurs faster than the chain propagation step. The total number of chains formed thus exceeds the amount of initiator as dormant chain ends R–OH may be reactivated by the proton exchange. Adjusting the monomer/CTA ratio allows to tailor the molecular weight of the final products.^{137–139} On account of the rapid chain transfer, narrow molecular weight distributions are typically achieved.

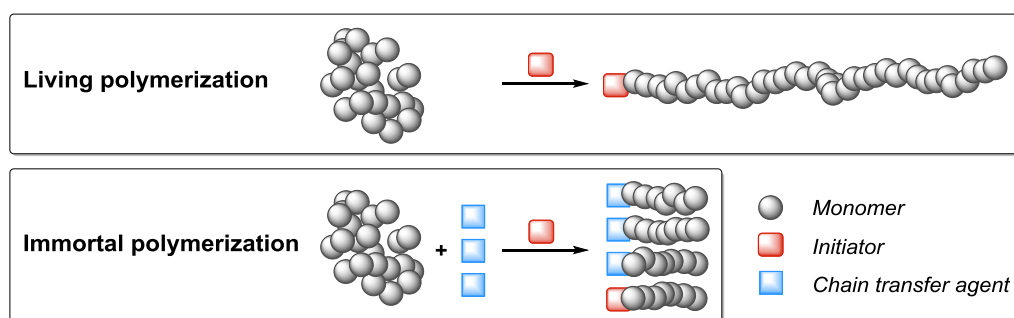


Figure 5.16 Schematic depiction of a living and an immortal polymerization. For living polymerizations, the total number of chains equals the number of initiating species. For immortal polymerizations, the number of chains basically equals the number of CTAs.

The immortal polymerization has been reported upon for the alternating copolymerization of propylene oxide (PO) and CO₂ catalyzed by homogeneous salen-complexes^{140–142} and for the preparation of poly(ether carbonate) diols under the action of DMC catalysts.^{56,143–149} In contrast, reports on the molecular weight control using zinc dicarboxylates as polymerization catalysts are limited to an older patent.¹⁵⁰ Zinc dicarboxylates have an attractiveness of mediating the PO/CO₂ copolymerization as they are easy to synthesize and handle, are environmentally benign and can have a high productivity.⁶⁶ Additionally and perhaps of more importance, the

composition of the copolymer in terms of PO respectively of the CO₂-content can be tuned by the reaction temperature and pressure as displayed in Chapter 5.1.¹²⁷ The products are thus ranging from poly(ether carbonates) to almost alternating polycarbonates. This sets the products of the herein described catalytic chain transfer copolymerization (CTCC) apart from products obtained under the action of homogeneous complexes. The polymer composition does not only affect the chain rigidity and thermal stability⁷⁷, but also properties such as gas permeability^{17,151}, and is hence a key factor in the synthesis of tailored materials (Figure 5.17).

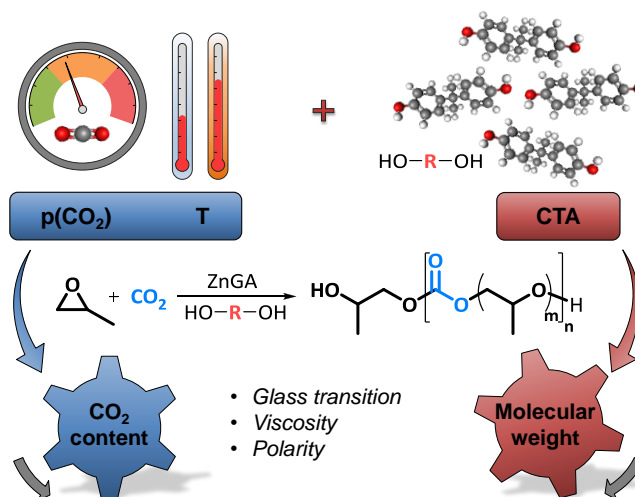


Figure 5.17 Control over reaction conditions of the ZnGA-mediated chain transfer copolymerization of PO and CO₂ allows the manipulation of the material properties by changing the CO₂-content and the molecular weight of the final products.

This chapter displays a comprehensive report of the synthesis of CO₂-based polyols using heterogeneous zinc dicarboxylate catalysts. The CCTC using a nanoscopic ZnGA in the presence of various chain transfer agents has been studied in detail with respect to control over molecular weight and product composition. The copolymerization process was monitored and insight into reaction kinetics and catalyst activity in dependence of CTA structure and concentration was gained. CO₂-based polyether carbonate diols are obtained with tunable material properties, *i.e.* within a certain range of glass temperatures and viscosities. The material properties of the resulting polymers are presented as a function of their molecular weight and composition.

5.3.1 Monofunctional chain transfer agents

Immortal polymerization is a versatile method that allows the direct synthesis of end-functionalized polymers with tunable chain lengths and has the option of increasing catalyst productivity (TON). The nanoscopic ZnGA catalyst system can be used to synthesize low-molecular weight oligo(propylene carbonate) in a CCTC with all the characteristics of an immortal copolymerization.^{138,137} Initially, 2-phenoxyethanol was employed as a model CTA to study the reaction mechanism (Table 5.7).

Table 5.7 CCTC using 2-phenoxyethanol as CTA.

En-try	PO/CTA [mol/mol]	TON ^a [-]	f_{carb}^b [mol%]	f_{cPC}^b [mol%]	$M_{n,\text{NMR}}^c$ [kg/mol]	$M_{n,\text{SEC}}/M_{w,\text{SEC}}^d$ [kg/mol]	PDI [-]
1	∞	988	91.7 ± 0.6	3.2 ± 0.5	-	66/296	4.5
2	930	1155	91.5	3.9	39	36/129	3.6
3	470	1073	91.5	4.5	25	26/87	3.4
4	140	1040	90.6	7.4	6.3	8.3/53	6.4
5	100	970	90.8	8.5	6.1	6.1/28	4.7
6	50	274	85.1	18.8	0.9	1.0/8.0	8.0

Experiments were performed using the standard protocol for PO/CO₂ copolymerizations. Reaction conditions: $T = 60$ °C, $p = 30$ bar, $t = 4$ h, $V(\text{PO}) = 50$ mL, $m(\text{ZnGA}) = 100$ mg. ^a in [g_{PPC}/g_{Zn}], ^b determined from ¹H-NMR spectra, ^c absolute molecular weights were calculated by the equation $M_{n,\text{NMR}} = M_{\text{RU}} (A_{1.39-1.03}/3) \cdot (A_{7.35-7.25}/2)^{-1}$ with the average molecular weight of a repetition unit M_{RU} , ^d determined by SEC in THF against PS standards using RI detector mode.

The presence of an aromatic entity in the otherwise aliphatic polymer backbone as the result of a successful chain transfer is readily detected in ¹H-NMR spectra. Analysis of the latter shows a low field shift of the signal of the CH₂-group adjacent to the phenoxy-end group as well as comparable changes in the signals of the aromatic system (Figure 5.18).

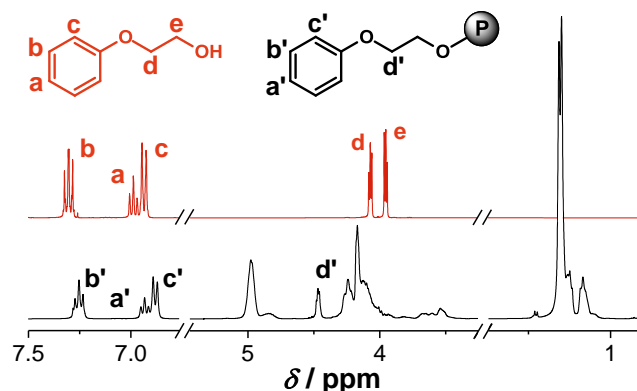


Figure 5.18 NMR spectra of low molecular weight PPC ($M_n \approx 0.9$ kg/mol; black) and 2-phenoxyethanol (red). The protons of the second methylene group (e) cannot be assigned clearly in the polymer spectrum.

Incorporation of the CTA into the polymer is further indicated in the ESI-MS spectrum (Figure 5.19). 2-Phenoxyethoxy-terminated chains of $M_n \approx 0.9$ kg/mol contain between zero and two ether linkages per chain. Interestingly, chains carrying two OH-end groups were also detected, indicating that the copolymerization may also have been initiated by traces of water or OH moieties originally bound on the ZnGA-surface. The existence of such functional groups on the catalytic surface of ZnGA has been proposed previously, however the detection of such entities has remained difficult.^{59,152,153} Mass spectrometry on higher molecular mass PPC is not readily achieved and has rarely been reported upon.¹⁵⁴

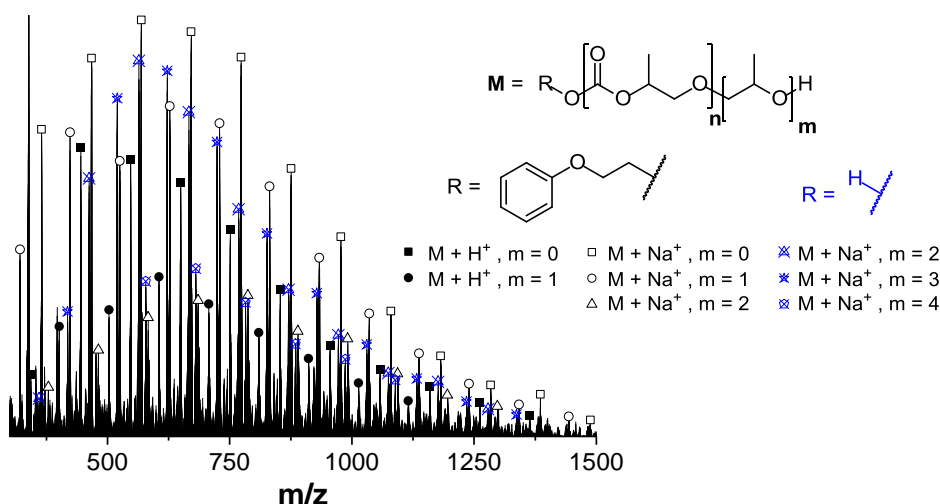


Figure 5.19 ESI mass spectrum of oligo(propylene carbonate) of $M_n \approx 0.9$ kg/mol (Table 5.7, entry 6).

The molecular weight of the oligo(propylene carbonate) products can be adjusted according to the ratio between PO and 2-phenoxyethanol as CTA (Table 5.7; Figure 5.20). The molecular weight is relative to polystyrene standards: as the hydrodynamic volume of the poly(propylene carbonate ether)s is a function of the composition, a transformation using a universal approach seemed not more accurate.¹⁵⁵ The experimental results show that the molecular weights of the obtained polymers correlate linearly with the PO/CTA ratio, *i.e.* the chain length can easily be tuned by varying the amount of CTA relative to PO. Thus, poly(ether carbonates) with number average molecular masses between 0.9 and 66 kg/mol were prepared. The fact that the PDI does not significantly change upon addition of a CTA indicates that the chain exchange reaction occurs rapidly relative to the propagation reaction. Only at high CTA-concentrations a somewhat higher PDI is observed.

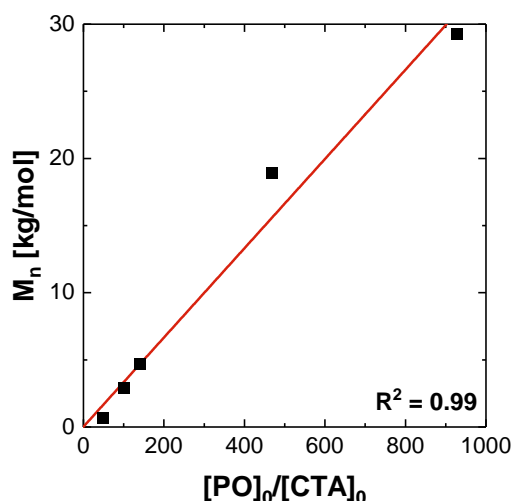


Figure 5.20 SEC-based relative M_n of the crude PPC vs. initial PO/CTA. 2-Phenoxyethanol is used as CTA (Table 5.7, entries 2 – 6).

The PDI values of the products are higher than one, contrasting to those of alternating PPC synthesized using discrete metal complexes.¹⁵⁵ This is taken as a consequence of the heterogeneous composition of the product chains with respect to ether and carbonate linkages, and the

backbiting reactions of intermediately formed chain ends. A broader monomodal distribution with a PDI of 3-5 may thus be explained. The heterogeneous nature of ZnGA catalyst alone cannot have a major impact on the PDI as the chains would grow on several centers in the CCTC.¹⁴¹ Rather the presence of various end groups in form of 1- and 2-alkoxy and corresponding carboxylate entities leads to a distribution of propagation rates, broadening the POISSON distribution of a perfect living and regioselective alternating polymerization. PDIs larger than 6 are resulting from bimodal distributions, typically containing small amounts of high molecular products (Chapter 5.3.2).

The polymer composition is virtually independent on the employed CTA concentration (Figure 5.21). The carbonate content is marginally lower at higher initial CTA concentrations. This may be related to the lower yields of copolymer under those conditions, which is accompanied by a higher fraction of cPC in the crude product. The backbiting reaction proceeds under such conditions with higher relative rates as a direct consequence of the increased concentration of chain ends.¹⁵⁶ Backbiting occurs until an ether linkage within the chain is reached (ether linkages are formed by two consecutive PO insertions and constitute stable chain ends).¹⁵⁷ Consequently, the backbiting lowers the carbonate content in the remaining product.^{33,156}

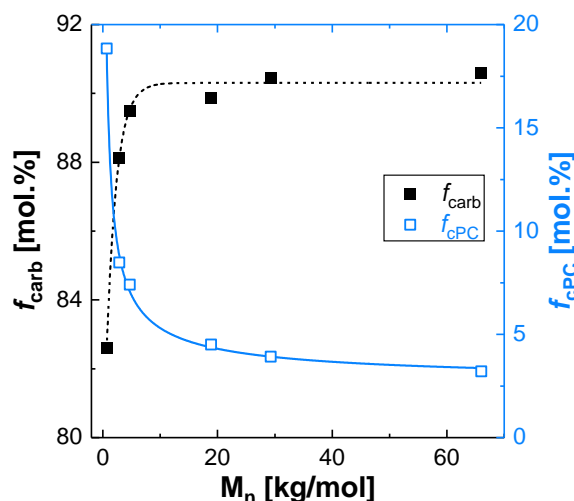


Figure 5.21 Content of carbonate linkages f_{carb} in the polymer and amount of cyclic by-product f_{cPC} as a function of the molecular weight, *i.e.* the concentration of end groups (Table 5.7).

The diols, *i.e.* chains formed from water or OH-entities in the catalyst, consequently, tend to have a higher content of ether linkages than comparable monols (Figure 5.22). The 2-phenoxyethoxy-initiated chains have only one chain end that can undergo a backbiting reaction to form cPC, whereas in case of water (or Zn-OH)-initiated chains, the backbiting may proceed from both sides. The ether content of the diol-terminated chains accordingly is higher ($f_{\text{carb}} = 63.4$ vs 88.5 mol%).

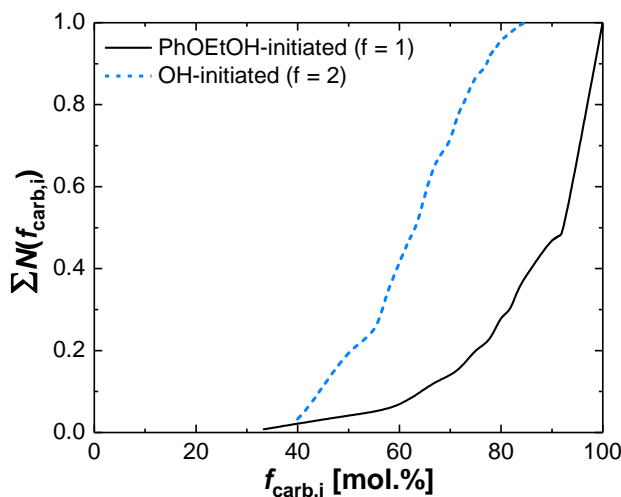


Figure 5.22 Cumulative distribution of the composition of mono- and bifunctional oligomers with $M_n \approx 0.9$ kg/mol (Table 5.7, entry 6). The distribution is obtained from the ESI mass spectrum (Figure 5.19).

The regio-selectivity of the CCTC products remains unchanged to the copolymerization without a CTA (Figure 5.23) yielding oligo(ether carbonates) with approximately 66 % head-to-tail-linkages (Table 5.8, entry 10).

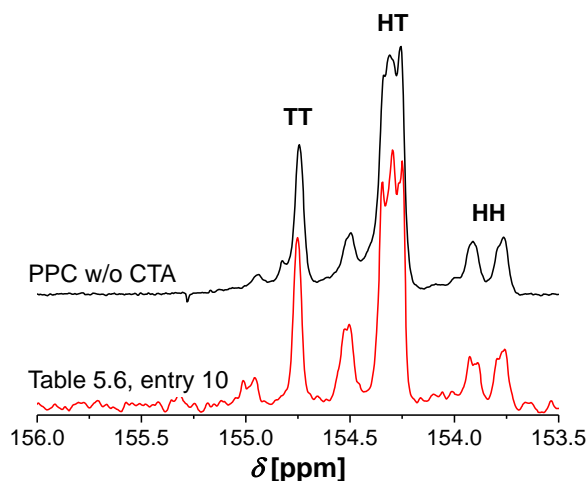


Figure 5.23 Carbonyl region of ^{13}C -IGATED-NMR spectra of high molecular weight PPC prepared without the use of CTA (top, black) and oligo(propylene carbonate) (Table 5.8, entry 10; bottom, red) obtained by CCTC using ZnGA. TT, HT and HH signals of carbonate linkages are assigned.

The presence of 2-phenoxyethanol as CTA leads to a marginal higher yield of polymer at low CTA concentrations (Table 5.7). The catalysts average turnover frequency (TOF) increases by about 20 % ($\sim 290 \text{ h}^{-1}$) compared to experiments without the use of a CTA ($\sim 250 \text{ h}^{-1}$). This may be related to a higher concentration of nucleophiles (at a minor loss of the amount of coordinated PO), and/or a better accessibility of the catalyst surface for smaller chains.¹²⁷ Higher concentrations of 2-phenoxyethanol, *i.e.* at PO/CTA ratios < 100 , decrease the activity significantly. Latter is tentatively caused by an increasing CTA absorption on the ZnGA surface, which hampers PO monomer coordination. Similar observations were made before, *e.g.* for the higher concentration of CO_2 at higher pressures; the surface coverage with PO is determining the ZnGA performance.¹²⁷ The coordination of a CTA will reduce the concentration of activated

PO-monomer, thus reducing the catalysts activity. These observations are reminiscent of the behavior of Zn-Co-DMC catalysts, which are also showing an induction time.^{145,158,159} The induction period in these catalysts may be related to coordination of some entity on the surface; indeed CTAs of low molecular weight, like glycerol, may fully deactivate DMCs.¹⁶⁰

The elementary reaction steps of the ZnGA-mediated PO/CO₂-copolymerization are not known with certainty, but usually formulated with an anionic chain end binding to the catalyst surface. In that context it is generally accepted that PO is activated for ring-opening by coordination to the catalyst surface. The reaction rate of copolymerization is most likely proportional to the amount of activated PO entities.¹²⁷ The coordination of PO stands in competition to that of CO₂ and also of CTAs in case of CCTC. The ring-opening leading to chain growth is affected by a nucleophilic chain end in most reports by the alkoxide/carboxylate coordinated to the surface (Figure 5.24). The propagating anionic chain ends in this mechanistic description can undergo an internal or additional protonation by the CTA, followed by a decoordination of R'OH/R'OC(O)OH. When this effective chain transfer is rapid relative to the insertion reactions, the result is a uniform propagation reaction. Alternatively, as formulated for DMC catalysis, an hydroxyl entity of an external reagent ROH may directly attack the surface activated PO.¹⁶⁰ Observations described in this chapter seem more compatible with an external nucleophilic attack of an OH entity, as proposed for the “catch-up” kinetics of DMC catalyzed propoxylations. Carbonate entities arise when insertion of CO₂ into an intermediate metal alkoxide bond is competitive to decoordination. Ether linkages result from the consecutive addition of two or more PO units to the propagating chain end. The formation of cPC may be observed as the result of a backbiting reaction of a corresponding alcohol chain end.

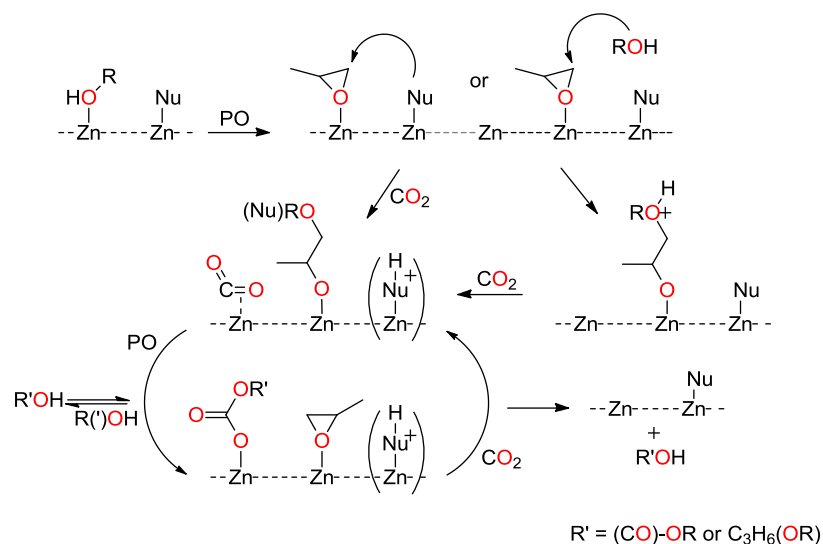


Figure 5.24 Reaction pathways for the CCTC of CO₂ and PO with alcohols under the action of ZnGA.¹⁴¹

5.3.2 Multifunctional chain transfer agents

The CCTC was extended to bi- and trifunctional bisphenol-derived CTAs in order to synthesize tunable poly(propylene ether carbonate) PPEC-polyols (Figure 5.25). The maiden CTAs contain both phenolic and aliphatic hydroxyl moieties. Other aliphatic CTAs were previously found effective.⁶² The use of CTAs with more than two OH-groups gives access to star-shaped polyols. Incorporation of these compounds into the polymeric product is also readily detected via NMR and SEC (UV/Vis detection mode). PPEC-polyols could be obtained for all derivatives except for higher concentrations of bisphenol S (BPS; Table 5.8, entry 3). A severe retardation of the catalyst underlies the observation (*vide infra*).

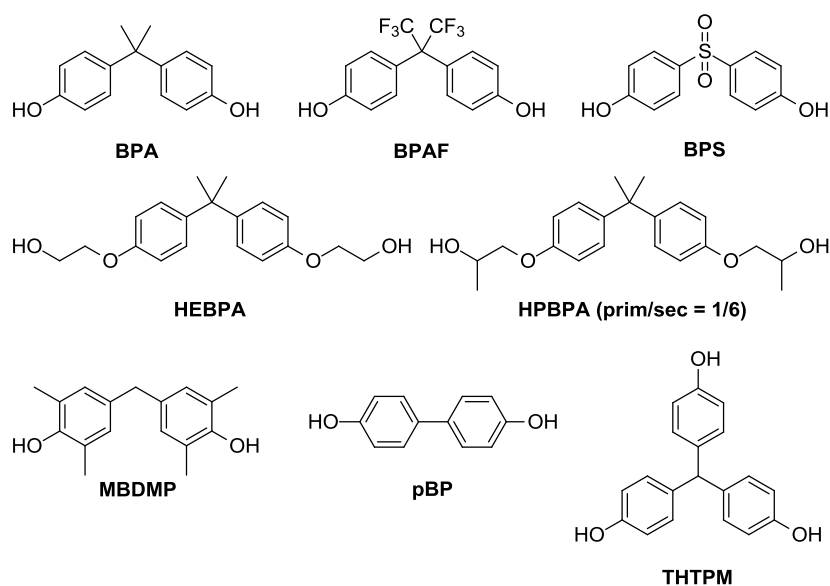


Figure 5.25 Utilized CTAs.

The catalysts selectivity (regarding carbonate vs ether linkages) remains unchanged, independent on the utilized CTA. Higher concentrations however decrease the catalysts productivity (Table 5.7). At the same time, the formation of cPC is more pronounced as a consequence of the reduced molecular weights. For the low molecular weight products ($M_n < 50$ kg/mol) GPC-measured M_n is in reasonable agreement with the absolute values determined by ¹H-NMR (Table 5.8).

Table 5.8 CCTC of PO/CO₂ with various CTAs.

Entry	CTA	PO/CTA [mol/mol]	TOF ^a [h ⁻¹]	$f_{\text{carb}}^{\text{b}}$ [mol%]	$f_{\text{cPC}}^{\text{b}}$ [mol%]	$M_{\text{n,NMR}}^{\text{c}}$ [kg/mol]	$M_{\text{n,SEC}}/M_{\text{w,SEC}}^{\text{d}}$ [kg/mol]	PDI [-]
1	BPAF	250	124	92.3	3.3	11	11/60	5.3
2	BPS	1000	33	86.2	2.8	4.7	2.6/27	10.4
3	BPS	250	2	-	-	-	n.d. ^e	-
4	MBDMP	250	182	88.9	5.2	6.5	5.0/39	7.8
5 ^f	HPBPA	250	108	92.8	3.0	12	9.5/33	3.4
6 ^g	THTPM	250	52	92.9	6.1	28	24/84	3.5
7	BPA	1000	274	92.0	3.3	56	37/144	3.9
8	BPA	500	241	91.5	2.8	23	23/107	4.6
9	BPA	250	167	91.6	2.4	9.4	8.9/55	6.1
10 ^h	BPA	50	87	88.2	14.4	3.6 ⁱ	3.9/17 ⁱ	4.4
11 ^h	BPA	25	38	78.6	12.9	0.8 ⁱ	0.9/7.3 ⁱ	7.7
12	HEBPA	1000	279	91.5	4.3	46	36/131	3.6
13	HEBPA	500	252	91.5	4.5	19	19/77	4.2
14	HEBPA	250	150	92.2	5.4	9.5	9.4/53	5.6

Experiments were performed using the standard protocol for PO/CO₂ copolymerizations. Reaction conditions: $T = 60$ °C, $p = 30$ bar, $t = 4$ h, $V(\text{PO}) = 50$ mL, $m(\text{ZnGA}) = 100$ mg, PO/CTA = 250. ^a in $[\text{g}_{\text{PPC}}/(\text{g}_{\text{Zn}} \cdot \text{h})]$, ^b determined from ¹H-NMR spectra, ^c absolute molecular weights were calculated by the equation $M_{\text{n,NMR}} = M_{\text{RU}} (A_{1.39-1.03}/3) * (A_{7.35-7.25}/4)^{-1}$ with the average molecular weight of a repetition unit M_{RU} , ^d determined by SEC in THF against PS standards using RI detector mode, ^e not determined, ^f primary/secondary OH $\approx 1/6$ as determined by ¹H-NMR, ^g $m(\text{ZnGA}) = 200$ mg, $t = 24$ h, ^h $m(\text{ZnGA}) = 400$ mg, $t = 7$ h, ⁱ determined from the crude reaction mixture.

Further insights into the CCTC were obtained by monitoring the copolymerization. The concentration of PO was measured *online* using an IR-sensor (Figure 5.26), and the uptake of CO₂ was registered by means of a mass flow controller (Figure 5.27). Note that the concentration of PO during the copolymerization is dependent on its consumption and the associated dilution by the soluble copolymer. The corresponding uptake of CO₂ is modified by the release of CO₂ from the solution. PO is a much better solvent for CO₂ than the copolymer, and with conversion some CO₂ is also liberated from the solution.¹⁶¹ The evaluation of the data thus would be elaborate, rate constants were not extracted although this is fundamentally possible.¹¹⁸

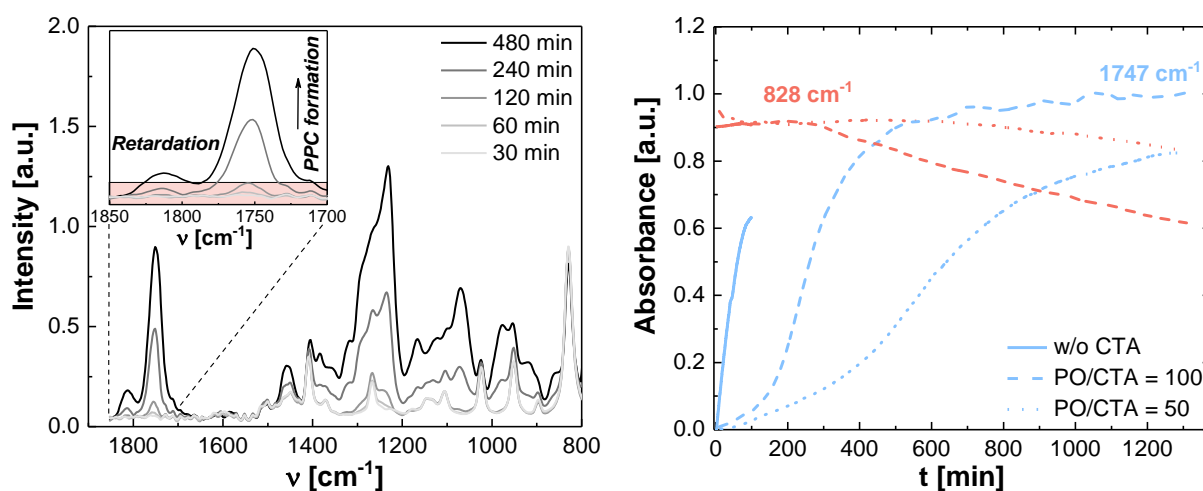


Figure 5.26 Left: *in-situ* FT-IR spectra of the PO/ CO_2 copolymerization using BPA as CTA (Reaction conditions: $T = 60^\circ\text{C}$, $p = 30$ bar, $m(\text{ZnGA}) = 1200$ mg, $V(\text{PO}) = 500$ mL, $\text{PO}/\text{BPA} = 100$). Right: Absorbance of the C=O-stretching vibration of PPC (1747 cm^{-1}) and the ring vibration of PO (828 cm^{-1}) in time for different ratios of PO/CTA (Reaction conditions: $T = 60^\circ\text{C}$, $p = 30$ bar, $m(\text{ZnGA}) = 1200$ mg, $V(\text{PO}) = 500$ mL).

Data from both methods of reaction-monitoring indicate an initial period of little or no monomer conversion upon addition of a CTA. The propagation rate increases substantially after this phase of inactivity. Larger concentrations of CTA prolong the initial period of retardation (Figure 5.26 and 5.27). The retardation period is observed for all utilized CTAs. In contrast, no retardation period is observed for the PO/ CO_2 copolymerization in the absence of a CTA.

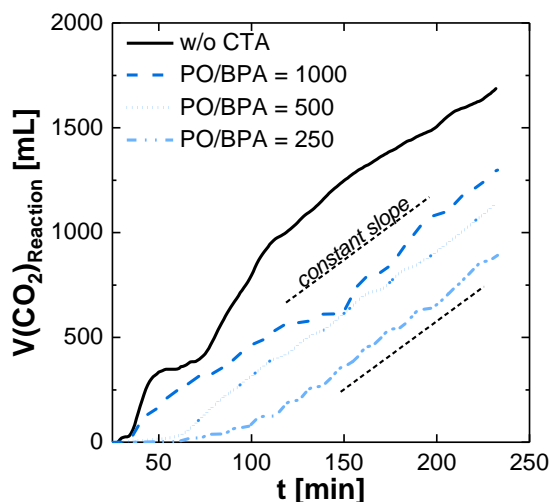


Figure 5.27 CO_2 uptake in dependence of the BPA concentration. $V(\text{CO}_2)_{\text{Reaction}}$ refers to the uncorrected amount of CO_2 consumed.

The induction time increases about exponentially with the concentration of CTA (Figure 5.28), illustrating the expected more than linear dependence of the rate of propoxylation on the concentration of CTA, blocking the surface and inhibiting its own conversion

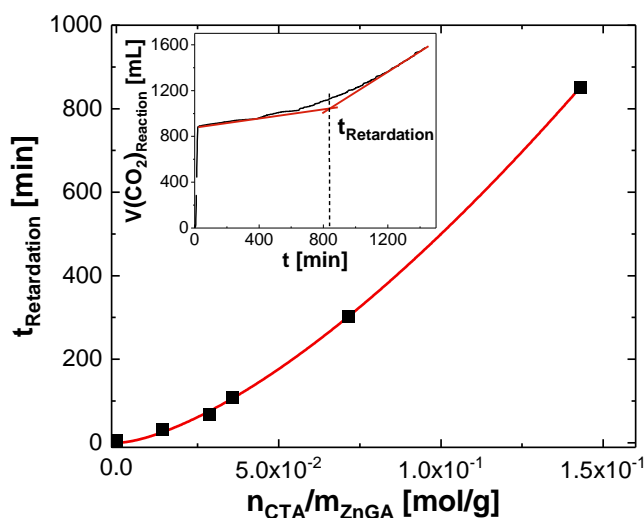


Figure 5.28 Length of the retardation period $t_{\text{Retardation}}$ for various BPA/catalyst ratios. The retardation period is determined empirically from the intersection of the slope in early reaction stages after saturation with CO_2 and the constant slope after initial increase of the CO_2 consumption rate (inset). $V(\text{CO}_2)_{\text{Reaction}}$ refers to the uncorrected amount of CO_2 consumed.

The activity of the catalytic system after various amounts of CTA are consumed is the same within experimental error. A skew competition between reaction of the maiden CTAs and the products of the first PO/ CO_2 additions of catalyst coordinated monomer leads to conversion of most of the CTAs and consequently to an increase in catalyst activity. The nature of the CTA and the primary products with respect to their nucleophilicity is a major factor in that.¹⁶² The first PO/ CO_2 addition(s) to the CTAs tend to majorly transform the primary alcohol or phenols into secondary hydroxyl entities, which are less readily reacting with activated PO (Figure 5.29).^{163,164} Same holds for BPAF and MDMBP that also give a similar rate of monomer conversion (Figure 5.30) after the induction period has passed in which the catalyst surface is blocked for PO coordination.

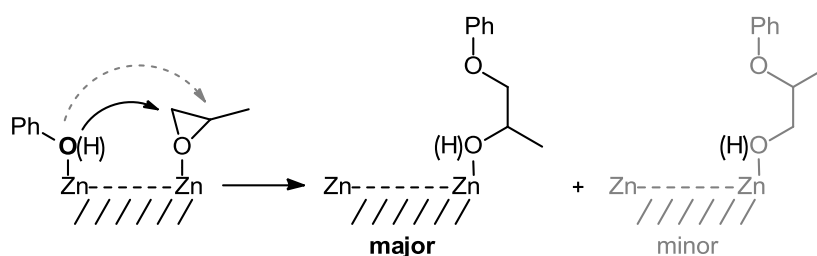


Figure 5.29 Propoxylation of maiden CTA predominantly results in the formation of secondary alkoxyates/alcohols.

BPA or HEBPA (ethoxylated BPA) as CTA show no significant differences in impact on the catalyst performance. The timespan necessary for activation of the catalyst is comparable at similar concentrations of BPA or HEBPA. The resulting rate of copolymerization after the initial phase is the same within experimental variance (Table 5.8). The formal ethoxylation of BPA to HEBPA, which is associated with the change from an aryloxy- to an alkoxy-type CTA, does not seem to fundamentally affect the chain regulation nor the catalysts performance (Figure 5.30). This is taken as evidence that the CTAs are preferentially consumed and that after

consumption the catalyst inhibition by the CTA is released. The coordination of these CTAs to the ZnGA catalytic surface is apparently reversible. The combination of alkoxylation and carboxylation of the original CTAs yields compounds with a higher molecular mass. The coordination strength of the CTA decreases effectively in the process. The first propoxylation/carboxylation steps of the phenolic CTAs thus appear rate-limiting for the catalyst activity. BPA and HEBPA are preferentially consumed in the inhibition phase, *i.e.* are more reactive towards activated PO than the first alkoxylation products. In contrast, application of HPBPA - propoxylated BPA - as CTA results in overall reduced conversion rates. The reached maximum copolymerization rate is much lower in the case of the propoxylated derivate after the same time of experiment with BPA or HEBPA. It obviously keeps on increasing over a much longer period and is thus slower to tentatively reach a similar maximum (Figure 5.30). Concomitantly, less of the CTA is incorporated into the copolymer, and the blocking of the catalyst surface partly sustains. This impact of HPBPA is as expected and consistent with the lower nucleophilicity of its predominantly secondary OH-groups relative to those of most of the primary alcohols and phenols in Figure 5.25. The same appears to be the case for pBP and apparently in a more extreme form for BPS. A low initial concentration of BPS could only be tolerated for achieving an active catalyst system within a reasonable time. A lower rate of the starting reaction resulting from either a higher concentration of the CTA or less nucleophilic CTA also tends to broaden the distribution of the molecular weight (Table 5.8). The observations with regard to induction time/polymerization rate as function of time - in reversion - thus also allow ranking the CTAs in coordination strength with respect to ZnGA.

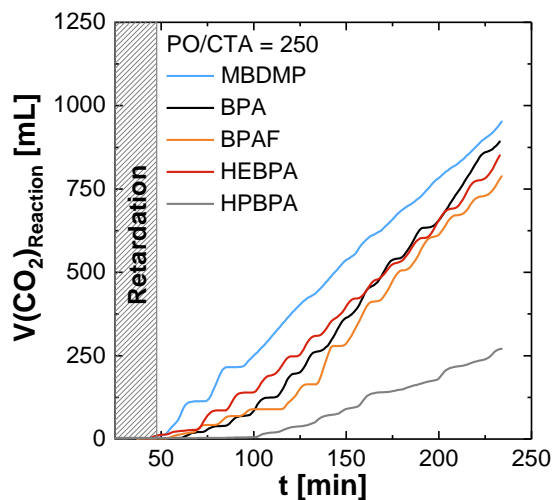


Figure 5.30 CO_2 consumption during the copolymerization with different CTAs (Table 5.8). $V(\text{CO}_2)_{\text{Reaction}}$ refers to the uncorrected amount of CO_2 consumed.

The initial high activity of the ZnGA catalyst typically decreases with conversion in several almost linear steps.¹²⁷ Similar behavior is observed for the activity of the system under CCTC conditions after the induction time has passed. The monomer depletion does not appear to significantly influence the TOF at conversions lower than a critical value, similar to what was found in previous studies of nanoscopic ZnGA catalysts.¹¹⁸ Deactivation of the catalyst was not of importance in that regard, and as it now turns out, inherent changes in the medium

influence the rate of copolymerization. It is found that the TOF in the first phase generally remains longer at the higher initial level, corresponding to a higher PO conversion upon addition of BPA. The first phase of the copolymerization is prolonged to a PO conversion in the range of $\approx 40\%$, which exceeds that of the unmodified copolymerization at $\approx 30\%$ (Figure 5.31). The initial rates are comparable (Table 5.9).

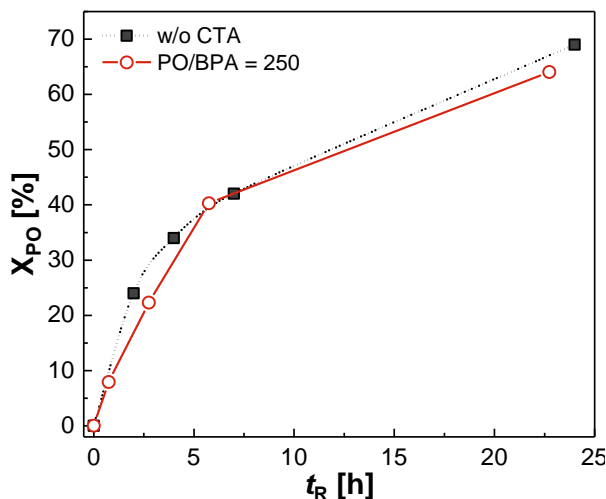


Figure 5.31 PO-conversion over time for the CCTC using BPA (red) and the copolymerization without the use of a CTA (black). t_R is the reduced reaction time, *i.e.* time of experiment without induction period.

When exceeding conversions of $X_{PO} \approx 30 - 40\%$, the TOF decreases significantly, entering the second phase of almost linear rates.¹²⁷ The system of PO/CO₂/copolymer at $X_{PO} > 40\%$ (molecular weight dependent) may be considered to become organo-gel-like, with a partly separated PO phase. The rate of propagation now also depends on the diffusion in the system and not so much on the catalyst itself. The polymer inhibits its own formation after exceeding this “critical conversion”. The mobility of the chains and associated with that the mobility of chain ends decreases with the increasing polymer concentration and molecular weight. This is more compatible with a copolymerization scheme with an external nucleophilic attack of an OH-moiety (Figure 5.24). These mechanistic aspects will, however, need further attention in future studies. Attempts to restore conditions of the initial phase by dilution with PO-monomer after 7 hours ($\approx 40\%$ PO conversion) do not allow to regain the catalysts performance in that regard (Table 5.9, entry 9). The dilution or time to dissolve the gel apparently is not sufficient to restore the initial conditions.

Table 5.9 CCTC rate using BPA and HEBPA as CTA.

Entry	CTA	PO/CTA [mol/mol]	t [h]	TOF ^a [h ⁻¹]	TON ^b [-]	X _{PO} ^c [%]	f _{carb} ^d [mol%]	M _{n,NMR} ^{d,e} [kg/mol]	M _{n,SEC} /M _{w,SEC} ^f [kg/mol]	PDI [-]
1	-	-	2	376	752	24	90.4	-	67/314	4.7
2	-	-	4	247	986	34	91.7	-	66/296	4.5
3	-	-	7	188	1315	42	90.0	-	91/327	3.6
4	-	-	24	84	2012	69	92.3	-	97/219	2.2
5	BPA	250	2	106	211	8	86.9	6.3	7.5/48	6.4
6	BPA	250	4	167	667	22	91.6	9.4	8.9/55	6.1
7	BPA	250	7	176	1232	40	91.3	15	15/85	5.7
8	BPA	250	24	81	1945	64	91.2	18	16/52	3.3
9 ^g	BPA	250	24	82	1967	66	90.9	15	15/88	5.9
10	BPA	100	4	31	126	7	70.7	0.7	- ^h	-
11	BPA	100	8	96	769	29	87.9	3.5	- ^h	-
12	BPA	100	12	80	939	34	87.3	4.1	- ^h	-
13	BPA	100	24	59	1407	49	87.9	5.8	- ^h	-
14	BPA	100	48	37	1782	62	89.9	7.6	6.9/34	5.0
15	HEBPA	250	2	110	221	9	91.2	3.9	6.7/26	3.8
16	HEBPA	250	4	150	600	21	92.2	9.5	9.4/53	5.6
17	HEBPA	250	7	152	1062	35	91.3	11	10/48	4.7
18	HEBPA	250	24	69	1647	54	91.0	14	13/42	3.3

Experiments were performed using the standard protocol for PO/CO₂ copolymerizations. Reaction conditions $T = 60$ °C, $p = 30$ bar, $V(\text{PO}) = 50$ mL, $m(\text{ZnGA}) = 100$ mg. ^a in [g_{PPC}/(g_{Zn} · h)], ^b in [g_{PPC}/g_{Zn}], ^c determined from the yield in/of the crude product, ^d determined from 1H-NMR spectra, ^e absolute molecular weights were calculated using the equation $M_{n,NMR} = M_{RU} (A_{1.39-1.03}/3) \cdot (A_{7.35-7.25}/4)^{-1}$ with the average molecular weight of a repetition unit M_{RU} , ^f determined by SEC in THF and referenced against PS standards using RI detector, ^g Addition of 25 mL PO after 7 h, ^h could not be analyzed due to superimposing retention times for the product and cPC.

As mentioned above, smaller amounts of high molecular weight polymers may form during the CCTC reactions, leading to bimodal distributions. The high molecular weight tails show up in the RI signal but are not readily detected by the UV-detector, illustrating the low concentration of the CTA chromophore in the high-molecular weight fraction (Figure 5.32). This was particularly observed in cases of higher CO₂ pressures ($p = 30$ bar) leading to products with a carbonate content f_{carb} of ± 90 mol% and is most likely to occur in the early phases. The occurrence is chaotic as the (initial) products of lower molecular weight obtained at 30 bars randomly show PDIs between about 3 and 10 (Figure 5.33). This type of observations has also been made in DMC catalyzed alkoxylation.¹⁶⁰

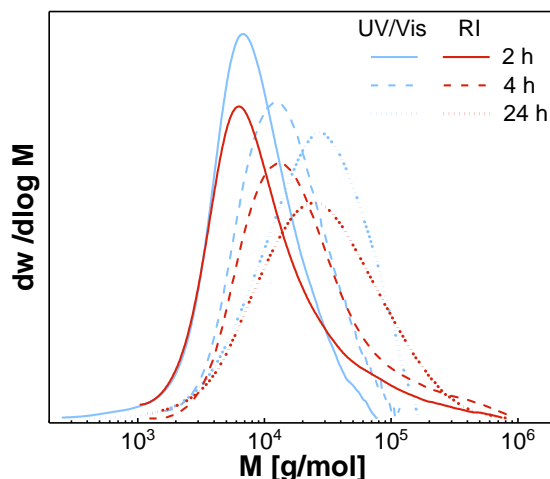


Figure 5.32 Molecular weight distributions of PPC-polyols with BPA as CTA at various conversions (Table 5.9, entries 4, 5 and 8) using RI (red) and UV/Vis (blue) detector mode.

The high molecular weight tails are tentatively formed as a consequence of the initial irregular conditions in the reactor. This is a typical result of insufficient mixing, where chain growth resulting from monomer diffusion is faster than chain transfer, *i.e.* chain diffusion. The erratic formation possibly is the result of challenges of suspending the small amount of catalyst in PO. The high molecular product seems to be generated in a CTA independent reaction channel that becomes of importance at higher CO₂ pressures. It is alike the product generated in the ZnGA-mediated copolymerization of PO and CO₂ without the aid of a CTA. These products reach a maximum molecular weight of $M_w = 200$ kg/mol, before catalytic activity is subsiding (Chapter 5.1). The direct copolymerization of PO and CO₂ has the highest rate at pressures of about 30 bar (and $T = 60$ °C). This may be the reason why such products are formed under these conditions, whereas the CCTC is more competitive at lower pressures. The initial higher PDIs of the products obtained at 30 bars of CO₂ pressure decrease with conversion (Figure 5.33). This is as explained above to be expected for a substantially living (/an immortal) copolymerization.

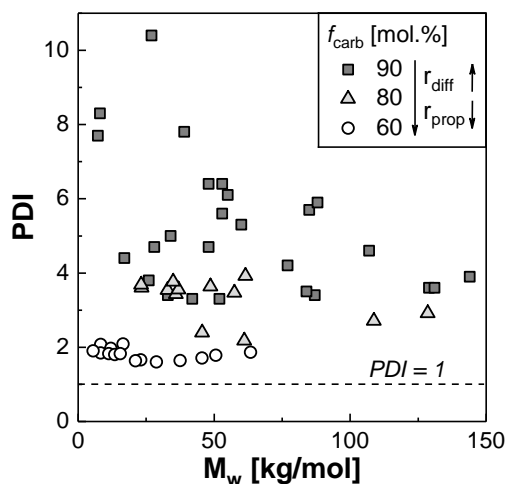


Figure 5.33 PDI of poly(propylene ether carbonate)-polyols of different compositions.

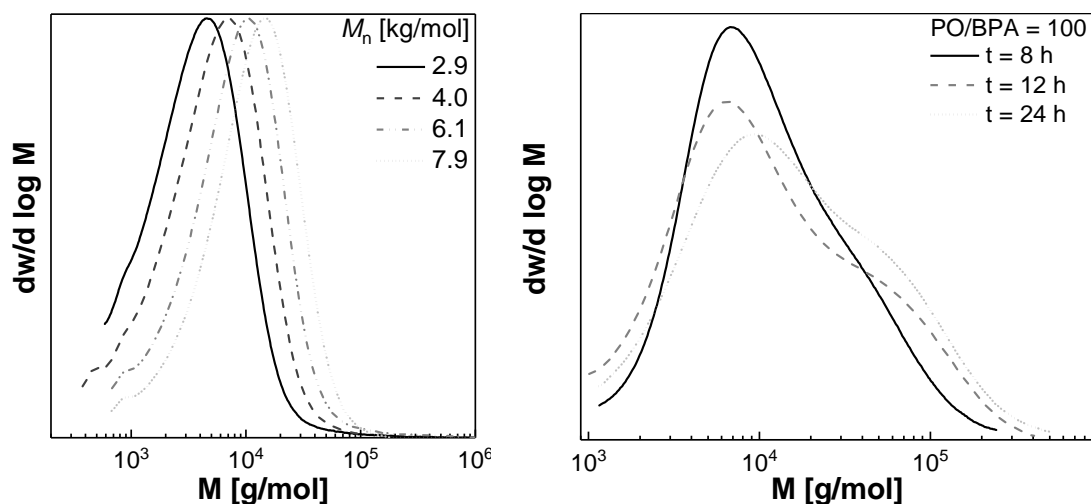


Figure 5.34 Left: molecular weight distributions for PPC-polyols with $f_{\text{carb}} = 60$ mol% (determined by SEC using RI detector mode). Right: Time dependent molecular weight distributions for a PO/BPA CCTO at 30 bars of CO_2 pressure ($f_{\text{carb}} = 90$ mol%; RI detector).

Consistently, products with a lower carbonate content do not show such a large variation in PDI and the high molecular weight tails are not formed (Figure 5.34, left). The PDIs of initial formed products are generally lower at lower pressures and are not so much dependent on conversion. Indeed, it is observed when performing the CCTC at 10 bar pressure of CO_2 (and $T = 80$ °C), leading to products with f_{carb} of 60 mol%, that the PDI is at a constant level of about 1.8. Similar holds for experiments leading to products with a f_{carb} of 80 mol%, but with larger PDIs. Note that the CCTC at 30 bars of CO_2 pressure still is the major process, and its dominance increases once the high molecular polymer reaches the “ceiling” molecular weight (Figure 5.34, right). Thus, the maximum of the initial product distribution is shifted towards higher masses, whereas the high molecular tail remains more or less unchanged and is more and more overlapped by the CTA based product mass. This feature is more readily detected using higher concentrations of CTA, where the main product remains lower in mass, and the formation of a bimodal distribution is indicated (Figure 5.35, right). The concentration of the high molecular weight tail does not increase substantially, its mass increases to the value of about 200 kg/mol.

The molecular weights M_n of the obtained polymers correlate directly with the PO-conversion (X_{PO}), confirming the pseudo-living nature of the ZnGA catalyzed PO/ CO_2 CCTC (Chapter 5.1). Catalysis at 30 bars of CO_2 pressure gives essentially uniform oligo(ether carbonates) independent of conversion with f_{carb} of ± 90 mol% (Figure 5.35). This holds true even up to PO conversions above 50 %.

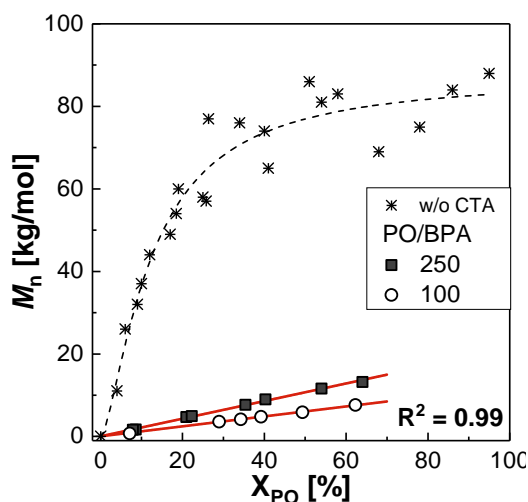


Figure 5.35 M_n (of the crude products) vs PO-conversion (X_{PO}) using BPA or HEBPA as CTA (Table 5.9, entries 5 – 18) in comparison with copolymerization without the use of a CTA ($T = 60$ °C, $p = 30$ bar; $f_{carb} = 90$ mol%).

The formation of a second distribution seems to be the consequence of a lower exchange rate of larger growing chains (once formed) near the catalyst with chains in the bulk, *i.e.* relative to the propagation rate. These larger chains of lower mobility consequently grow at a higher rate as long the ceiling molecular weight is not reached, contrary to the catch-up kinetics observed for alkoxylation/carboxylation of lower molecular weight. The balance between chain (segment) mobility and rate of copolymerization may be determining the product distribution. Both are dependent on the reaction conditions, which thus determine the constitution of the product being formed. The rate of diffusion of the polymers, resp. their viscosity, is a function of the composition.¹⁶⁵ Chain mobility obviously is an important issue in the generation of poly(ether carbonate) diols, both with respect to conversion and chain regulation. It was thus decided to determine the melt viscosities of a series of products as function of molecular weight and composition. Melt viscosities can be taken as measure for the chain mobility: a melt resembles a theta solution of the polymer, which would be an acceptable model for the situation in the reaction medium of PO/CO₂ and in the organogel formed at higher conversions.

Poly(propylene ether carbonates) with various compositions are accessible by adjusting the reaction parameter p and T (Table 5.10) (Chapter 5.1) It was found possible to prepare OH-terminated polycarbonates with controllable molecular weight and compositions between $f_{carb} \approx 60$ and 90 mol%. These products are closing the gap between poly(ether carbonates) obtainable by DMC catalysis⁵⁶ and the perfectly alternating poly(carbonates) obtained by *e.g.* Co-salen catalysis^{126,166}, *i.e.* when using a single catalyst.

Table 5.10 Results for copolymerization experiments under varying reaction conditions (T and p).

Entry	CTA	PO/CTA [mol/mol]	T [°C]	p [bar]	TON ^a [-]	f_{carb} ^b [mol%]	$M_{n,\text{SEC}}/M_{w,\text{SEC}}$ ^c [kg/mol]	PDI [-]
1	BPA	250	60	30	667	91.6	8.9/55	6.1
2	BPA	250	60	15	675	84.9	14/42	2.9
3	BPA	250	60	5	406	73.7	3.5/13	3.6
4	BPA	250	80	5	183	60.2	8.5/64	7.6
5 ^d	2-phenoxy- ethanol	250	80	10	897	58.1	7.5/14	1.8
6 ^d	2-phenoxy- ethanol	200	80	10	842	58.0	6.2/11	1.8
7 ^d	2-phenoxy- ethanol	150	80	10	765	57.0	4.5/8.3	1.8
8 ^d	2-phenoxy- ethanol	100	80	10	1011	52.3	2.9/5.5	1.9

Experiments were performed using the standard protocol for PO/CO₂ copolymerizations. Reaction conditions $t = 4$ h, $V(\text{PO}) = 50$ mL, $m(\text{ZnGA}) = 100$ mg, PO/BPA = 250. ^a in [g_{PPC}/g_{Zn}], ^b determined from ¹H-NMR spectra, ^c determined by SEC in THF, referenced against PS standards, ^d $t = 48$ h.

Poly(propylene ether carbonates) with lower carbonate contents have substantial lower melt viscosities (Figure 5.36; Table 5.11). The complex zero-shear viscosity $|\eta_0^*|$ of the polymer melts at 50 °C is approximately one order of magnitude lower for polymers with f_{carb} of 80 mol% than for those with f_{carb} of 90 mol%. The larger scattering of samples with f_{carb} of 90 mol% in the expected linear double logarithmic presentation of zero-shear viscosity versus weight average molecular mass is resulting from the individual distributions of the samples. These vary much more than those of f_{carb} of 60 or 80 mol% (Figure 5.34). The higher probability for random formation of a second distribution at higher CO₂ pressure is thus coincident with the relative lower mobility of the corresponding products. Consistently, the polymers with lower f_{carb} show more uniform and narrow molecular weight distributions even at high CTA-concentrations. It is therefore concluded that decreasing mobility of the chain segments can explain the occurrence of the second phase in the copolymerization and the formation of high molecular fraction at insufficient intermixing.

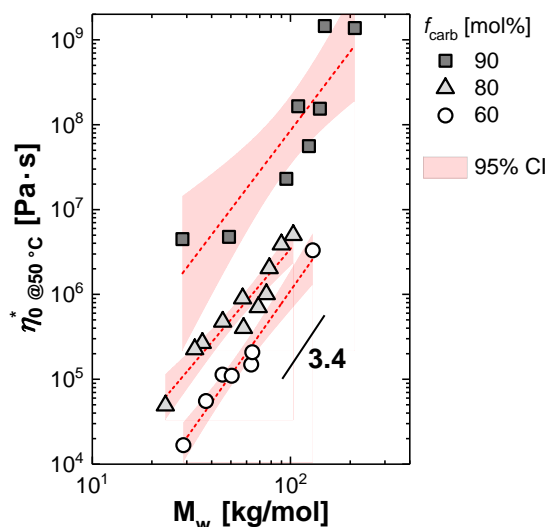
Table 5.11 Zero-shear viscosities at 50 °C for poly(propylene ether carbonates) with different M_w and f_{carb} .

f_{carb} [mol%]	M_w [kg/mol]	η_0 @ 50 °C [MPa · s]	f_{carb} [mol%]	M_w [kg/mol]	η_0 @ 50 °C [MPa · s]	f_{carb} [mol%]	M_w [kg/mol]	η_0 @ 50 °C [MPa · s]
92.7	211	1370	80.2	104	5.0	60.2	130	3.3
92.3	149	1450	79.8	90	3.9	60.2	64	0.21
85.4	141	150	75.1	78	2.0	65.7	63	0.15
87.3	124	56	79.1	76	1.0	58.0	51	0.11
89.6	110	160	78.0	69	0.70	62.7	46	0.11
91.5	95	23	79.3	58	0.40	62.9	38	0.06
91.2	49	4.7	77.0	58	0.89	63.0	29	0.02
90.8	29	4.5	75.2	46	0.47			
			75.7	35	0.27			
			76.0	33	0.22			
			79.3	23	0.05			

Table 5.12 Slope a of the double-logarithmic plot of M_w vs η_0 @ 50 °C for poly(propylene ether carbonates) with different compositions and coefficient of determination of the corresponding fits according to Eq. 5.17.

f_{carb} [mol%]	a	R^2
90	3.1 ± 0.6	0.80
80	2.8 ± 0.3	0.91
60	3.3 ± 0.3	0.97

Controlling the viscosities of the products anyway is crucial regarding the processability of the material, *e.g.* during polyurethane manufacturing when mixing/demixing of chain extender, soft and hard phase components is proceeding. The molecular weight dependence of η_0^* displays the importance of preventing the formation of high-molecular weight tails to maintain low product viscosities. The formation of such high-molecular weight side products is also commonly observed during polyether-polyol synthesis using DMC catalysts.¹⁶⁷


Figure 5.36 Zero-shear-viscosity η_0^* at 50 °C for poly(propylene ether carbonates) of different carbonate contents and molecular weights. 2-Phenoxyethanol and BPA were used as CTA (Table 5.10)

The polymer composition is determining the final material properties in extension to the molecular weight, which was found adjustable over the amount and type of CTA. This is of particular relevance to the glass transition temperature⁷⁷, an important parameter when considering the poly(ether carbonate) polyols as polyurethane soft phase components. The glass transition temperature T_g as a function of molecular weight and composition follows the FOX-FLOORY equation in good approximation.¹⁶⁸ T_g becomes more or less independent of the molecular weight M_n in between 15 and 25 kg/mol (Figure 5.37). Latter is an acceptable range for the broader distributed products, the entanglement molecular weight is expected in that range too.⁷⁷ Below the critical molecular weight of $M_c \approx 10$ kg/mol, T_g drops rapidly.

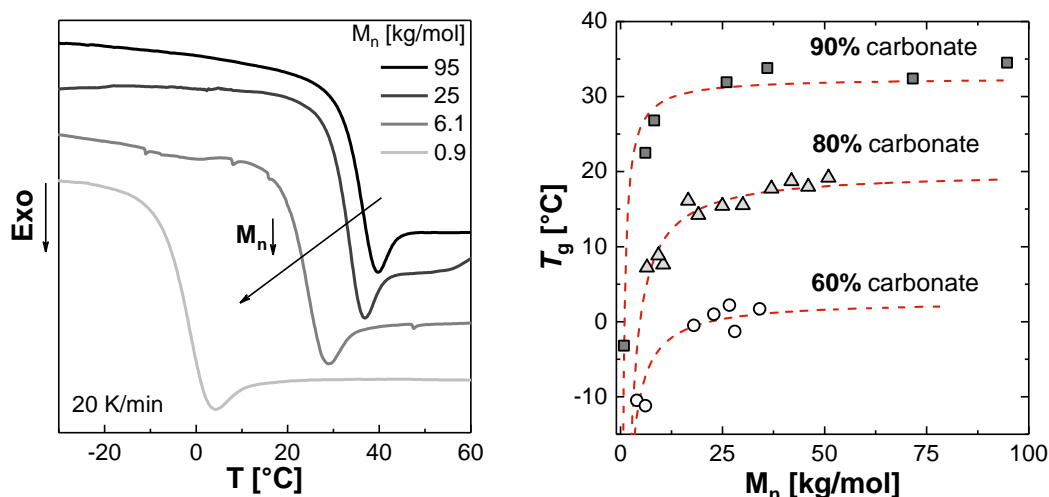


Figure 5.37 Left: DSC traces of PPC with different molecular weights (SEC-based). Right: T_g of PPC with compositions of $f_{\text{carb}} = 60 - 90$ mol% as a function of their molecular weight. The dashed lines represent a fit along the FOX-FLOORY equation $T_g = T_{g,\infty} - K / M_n$. The values for M_n are absolute determined by $^1\text{H-NMR}$.

5.4 Thermo-rheological properties of poly(propylene carbonate) melts

Poly(propylene carbonate) (PPC) is considered one of the most promising PACs for packaging applications substituting non-biodegradable plastics, as it features excellent gas barrier properties and a high resilience.¹⁷ The thermal and mechanical properties of PPC are well known.^{14,169} With regard to processing operations, the thermo-rheological behavior of PPC melts is also of importance. Several studies have focused on the rheological characterization of neat PPC^{77,155,170,171}, end-capped PPC⁸², PPC blends^{172–175} as well as poly(ether carbonate) polyols.¹⁶⁵ Small amplitude oscillatory shear (SAOS) experiments are routinely carried out to probe the viscoelastic properties of polymer melts. However, the thermoplastic processing of such materials usually is performed under large and more rapid deformation. The viscoelastic behavior under SAOS, thus, is an insufficient description as non-linear effects may be determining the behavior during typical processing.¹⁷⁶ It is therefore of importance to understand and predict the flow behavior in the non-NEWTONian regime to identify appropriate processing conditions.

In Chapter 5.1, it was shown that nanoscopic ZnGA catalysts enable the synthesis of PPC with tunable chain compositions.¹²⁷ In this chapter, the thermo-rheological behavior of PPC melts with varying carbonate contents between $f_{\text{carb}} = 51 - 92$ mol% is investigated, with an emphasis on the response to large amplitude oscillatory shear (LAOS).

5.4.1 Small amplitude oscillatory shear conditions

PPC samples with different molecular weights and compositions ranging from $f_{\text{carb}} = 51 - 92$ mol% were prepared by using a nanoscopic ZnGA catalyst and 2-phenoxyethanol as CTA. Precise control over the reaction conditions allows to tailor the molecular weight and the polymer composition, according to the previous chapters. The viscoelastic behavior of these PPC melts was first determined under SAOS conditions (Table 5.13).

Table 5.13 Data on PPC samples.

$f_{\text{carb}}^{\text{a}}$ [mol%]	M_w^{b} [kg/mol]	PDI [-]	$\eta_0 @ 110\text{ }^\circ\text{C}$ [kPa · s]	T_g^{c} [°C]
92.9	296	4.1	11600	32.4
93.5	247	3.9	4500	33.4
93.2	211	3.3	560	n.d.
91.4	192	3.0	1100	n.d.
93.2	149	2.4	700	33.3
91.0	110	2.6	80	n.d.
91.5	95	3.1	37	33.8
76.8	198	2.8	380	20.5
76.6	163	2.7	240	24.1
79.5	136	2.9	160	25.6
80.6	129	2.9	100	21.7
81.5	110	2.7	74	23.5
78.7	79	1.9	15	18.7
77.0	58	3.5	2.6	16.1
75.2	46	2.4	0.9	14.2
60.2	130	5.1	26	-1.3
65.8	63	1.9	1.4	6.3
59.1	51	1.8	0.6	1.0
62.3	46	1.7	0.4	2.2
63.0	38	1.6	0.2	1.3
63.1	29	1.6	0.1	1.5
51.2	42	1.6	0.2	-8.2
50.9	36	1.9	0.01	-11.1

^a Determined by ¹H-NMR, ^b determined by SEC in THF, reported against PS standards, ^c determined using DSC.

The frequency-dependence of the viscosity was determined in a temperature range between 30 and 150 °C (Figure 5.39), except for the highest molecular weight sample with $f_{\text{carb}} = 92$ mol%, which was analyzed up to 190 °C. The thermal stability of the melts under the applied conditions was confirmed by time sweeps at $T = 150$ °C (Figure 5.38). Samples with $f_{\text{carb}} = 51$ and 62 mol% could not be measured at temperatures above 110 °C respectively above 130 °C on account of their too low viscosity. These samples are considered stable at the applied measurement temperatures and were not analyzed by time sweeps.

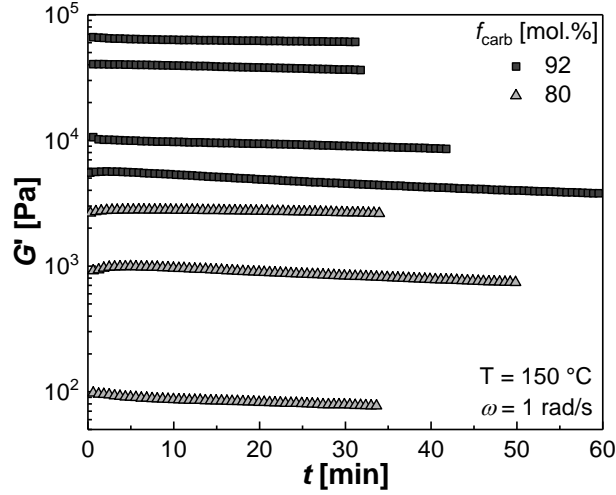


Figure 5.38 Time sweeps of PPC melts at $T = 150\text{ °C}$.

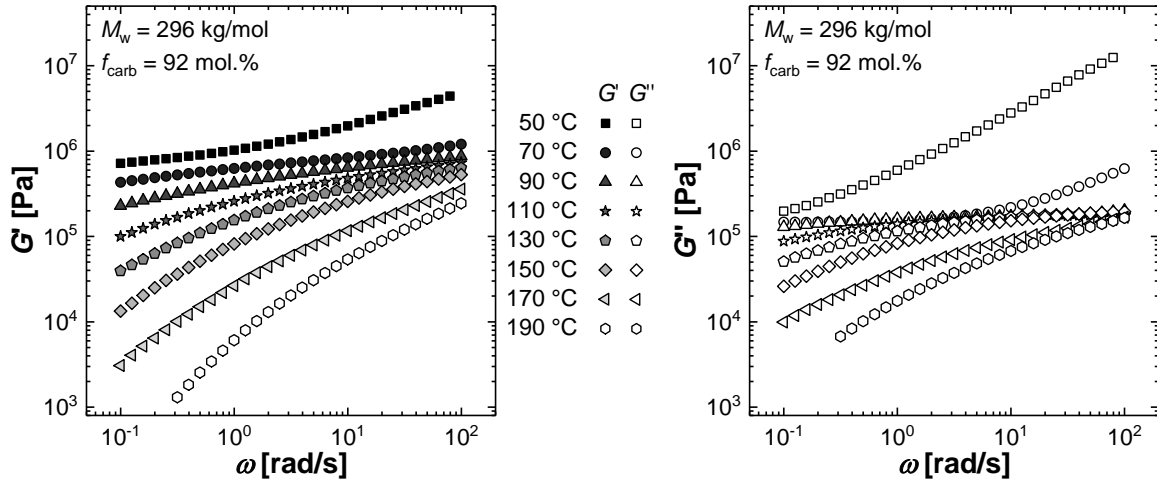


Figure 5.39 Frequency dependence of the storage modulus G' (left) and the loss modulus G'' (right) at $T = 50 - 190\text{ °C}$ for high-molecular weight PPC ($M_w = 296\text{ kg/mol}$, $f_{\text{carb}} = 92\text{ mol.}\%$).

The time-temperature-superposition (TTS) method, allows to align frequency sweeps at different temperatures to build a master curve with a larger frequency domain (Figure 5.40). A horizontal shift-factor a_T is defined as the ratio of the relaxation times λ at a certain temperature T and a reference temperature T_{ref} which here was set at 110 °C (Equation 5.9)

$$a_T = \frac{\lambda(T)}{\lambda(T_{\text{ref}})} \quad (5.9)$$

For thermoplastic polymers in the temperature region $T_g < T < T_g + 100\text{ K}$ the WILLIAMS-LANDEL-FERRY (WLF) equation (Equation 5.10) is used¹⁷⁷

$$\log a_T = \frac{-c_1 \cdot (T - T_{\text{ref}})}{c_2 + T - T_{\text{ref}}} \quad (5.10)$$

with material specific constants c_1 and c_2 .

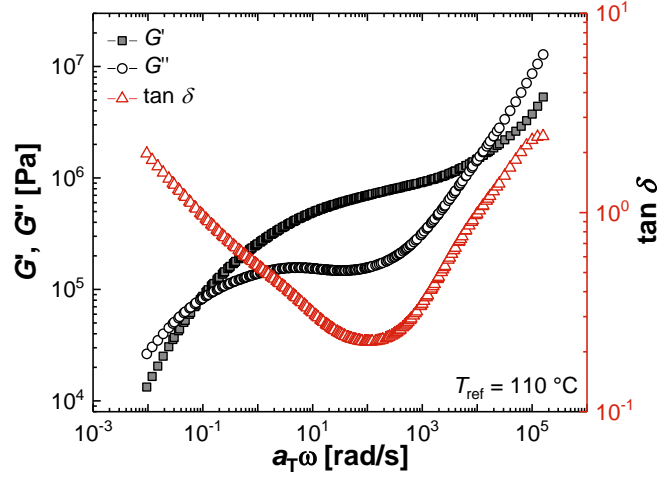


Figure 5.40 Master curve of the storage G' , loss modulus G'' and loss factor $\tan \delta$ of high-molecular weight PPC ($M_w = 296$ kg/mol, $f_{\text{carb}} = 92$ mol%) under small deformations ($\gamma_0 = 10\%$) at $T_{\text{ref}} = 110$ °C.

High-molecular weight PPC melts show an ideal viscoelastic behavior at low deformations over the entire frequency range. The melts show predominantly viscous behavior at low frequencies (or high temperatures) with G' and G'' having slopes close to 2 and 1, respectively. At higher frequencies, G' tends towards a rubber-elastic plateau. The rubbery plateau is indicated as a shoulder; the length of this shoulder increases with the molecular weight. Such a behavior is typical for polydisperse samples. Figure 5.41 exemplifies this feature for PPC melts with $f_{\text{carb}} = 92$ mol%. Similar observations were made for samples with different carbonate contents.

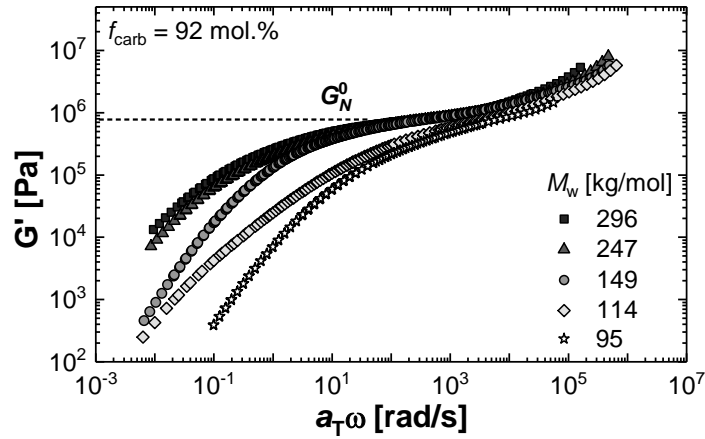


Figure 5.41 Storage modulus G' for PPC with different M_w ($f_{\text{carb}} = 92$ mol%) at $T_{\text{ref}} = 110$ °C. The sample with $M_w = 114$ kg/mol deviates on account of its broader MWD. Therefore, the slope of G' does not reach 2 even under terminal flow conditions.

The temperature dependence of relaxation processes can be expressed by means of the apparent activation energy of flow E_a . The apparent activation energy of flow E_a equals

$$E_a = 2.3R \frac{c_1 \cdot c_2 \cdot T^2}{(c_2 + T - T_{\text{ref}})^2} \quad (5.11)$$

with R as the ideal gas constant. The values of E_a for PPC melts with carbonate contents of $f_{\text{carb}} = 51 - 92$ mol% are displayed in Table 5.14. The activation energy of flow is a function of the polymer composition (Figure 5.42). E_a decreases significantly with decreasing f_{carb} , *i.e.* with a lower chain rigidity. The activation energy at 50 °C from 221 to 99 kJ/mol for PPC melts with 92 mol% and 51 mol% carbonate linkages. The effects become smaller at higher temperatures where the free volume is higher. No significant impact of the molecular weight on E_a was observed between $M_w = 45$ and 296 kg/mol, regardless of the polymer composition.

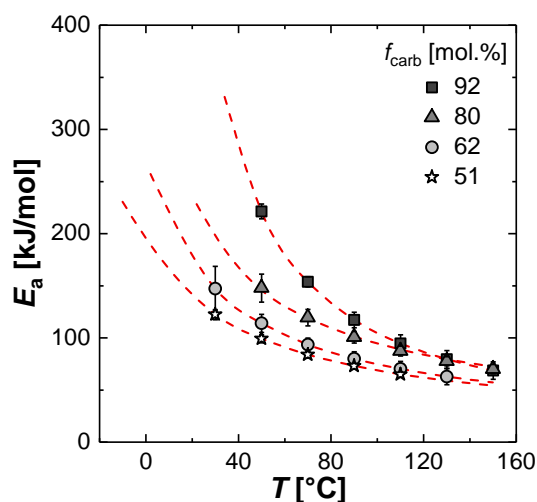


Figure 5.42 Experimental flow activation energy E_a in dependence on the temperature for PPC melts with various compositions. The dashed lines correspond to Equation 5.11.

Table 5.14 Activation energy of flow E_a for PPC melts with various compositions.

T [°C]	E_a [kJ/mol]			
	92 mol%	80 mol%	62 mol%	51 mol%
30	-	-	147 ± 21	122 ± 5
50	221 ± 7	149 ± 17	114 ± 9	99 ± 4
70	154 ± 5	120 ± 10	94 ± 6	84 ± 3
90	117 ± 7	100 ± 7	80 ± 7	73 ± 3
110	94 ± 8	87 ± 6	70 ± 7	65 ± 2
130	79 ± 9	77 ± 5	63 ± 8	-
150	69 ± 8	69 ± 5	-	-

The master curves further allow to estimate the average molecular weight between two temporary network points. This so-called entanglement molecular weight M_e may be calculated according to Equation 5.12

$$M_e = \frac{\rho RT}{G_N^0} \quad (5.12)$$

with the polymer density ρ and the plateau modulus G_N^0 . The densities ρ of the polymer melts were measured volumetrically (Chapter 6.7). The broad molecular weight distributions (PDI = 1.5 – 5.1) makes the determination of the plateau modulus rather inaccurate. The

plateau modulus instead is taken from the storage modulus at the global minimum of $\tan \delta$, *i.e.* the point of highest elasticity.¹⁷⁸

$$G_N^0 = G'(\omega)_{\tan \delta_{\min}} \quad (5.13)$$

M_e can further be used to determine a characteristic packing length p' (Equation 5.14)

$$p' = \sqrt[3]{\frac{M_e}{n_t^2 \cdot N_A \cdot \rho}} \quad (5.14)$$

with the temperature-insensitive coefficient $n_t = 21.3$ and the AVOGADRO number N_A .¹⁷⁹ Based on p' a critical molecular weight M_c is calculated that correlates to the onset of the entangled state

$$M_c = M_e \cdot \left(\frac{p^*}{p'} \right)^{0.65} \quad (5.15)$$

in which $p^* = 9.2 \text{ \AA}$. At $M > M_c$ the chains effectively form temporary networks resulting in a change of the slope of the viscosity $\eta(M)$ (Figure 5.44). The values for M_e , p and M_c are displayed in Table 5.15.

Table 5.15 Plateau modulus G_N^0 , entanglement and critical molecular weight M_e resp. M_c and packing length p' for PPC melts with various compositions at 25 °C.

f_{carb} [mol%]	G_N^0 [kPa]	ρ [kg/m ³]	M_e [kg/mol]	M_c [kg/mol]	p' [Å]
92	750 ± 30	1260	4.2 ± 0.1	10.2 ± 0.3	2.3 ± 0.1
80	560 ± 60	1240	5.5 ± 0.6	12.8 ± 1.0	2.2 ± 0.1
62	530 ± 30	1190	5.6 ± 0.3	12.9 ± 0.6	2.5 ± 0.1
51	440 ± 20	1150	6.4 ± 0.3	14.4 ± 0.5	2.7 ± 0.1

Incorporation of carbonate entities into poly(propylene glycols) increases the chain rigidity as can be concluded from the T_g and E_a (Table 5.13 and 5.14). The entanglement density increases with the f_{carb} . This trend possibly can be attributed to intermolecular interactions of the polymer chains. Indeed, these observations are in agreement with earlier investigations that proposed discrete intermolecular interactions between carbonate and methylene groups of neighboring polymer chains.¹⁶⁵ As a consequence, the chains form a temporary network structure in melt state. The presence of such associative interactions is further verified in the molecular weight dependence of the zero-shear viscosities η_0 . The values for η_0 were extracted using the CARREAU-YASUDA model (Figure 5.43)

$$\eta(\omega) = \eta_\infty + (\eta_0 - \eta_\infty) \left[1 + (\lambda_0 \omega)^b \right]^{n/b} \quad (5.16)$$

with the infinite shear viscosity η_∞ , the longest relaxation time λ_0 and the slope in the power law region n . The parameter b accounts for the transition between zero-shear conditions and

the power law region. The fit parameters are displayed in Figure 5.44. The results obtained from the CARREAU-YASUDA model show an exponential dependence of the relaxation time λ_0 on M_w with values between 3.4 and 4.0. These values are in agreement (within experimental precision) with the reported behavior on entangle polymer melts.¹⁸⁰

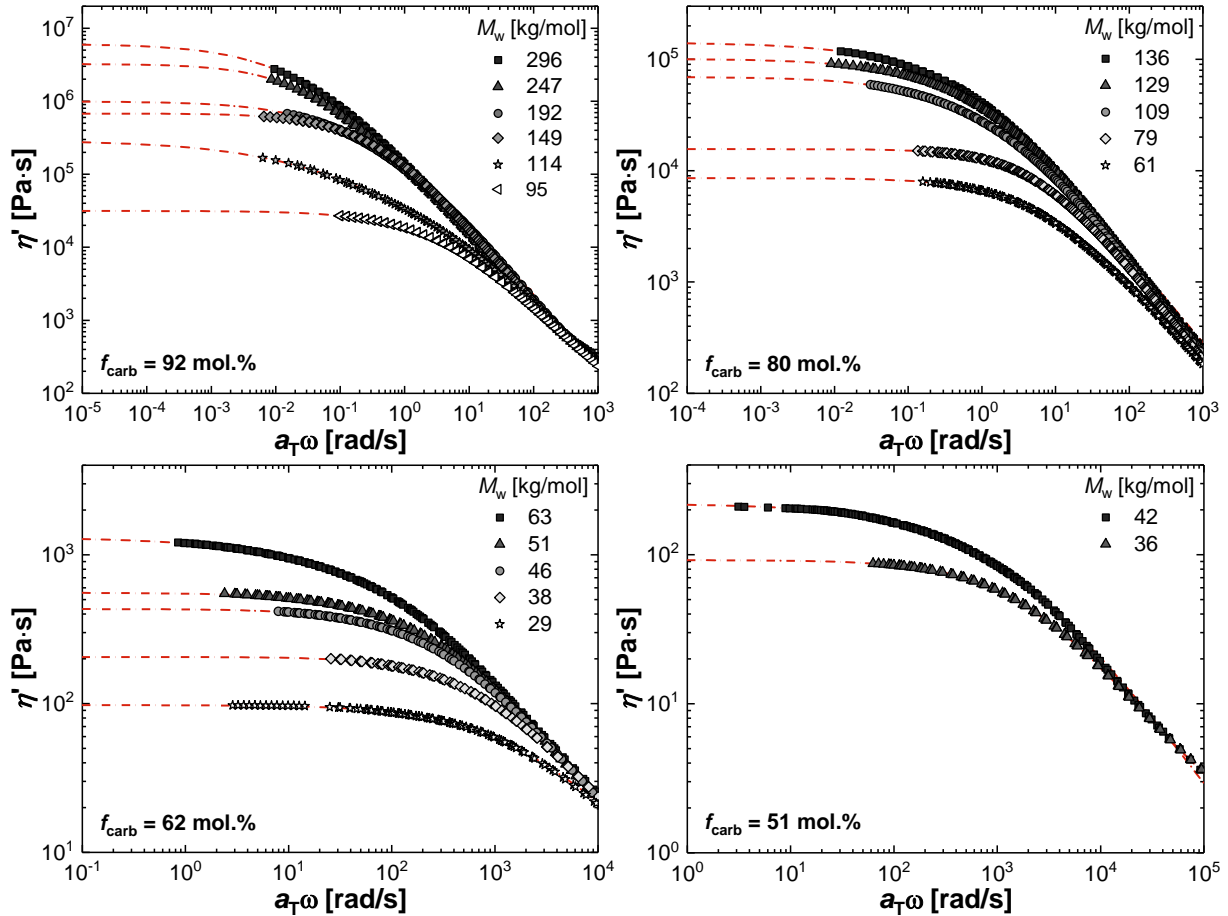


Figure 5.43 Dynamic viscosities η' for PPC with different f_{carb} and M_w . The dashed lines represent the fit of the viscosity according to CARREAU-YASUDA (Equation 5.16). $T_{\text{ref}} = 110$ °C.

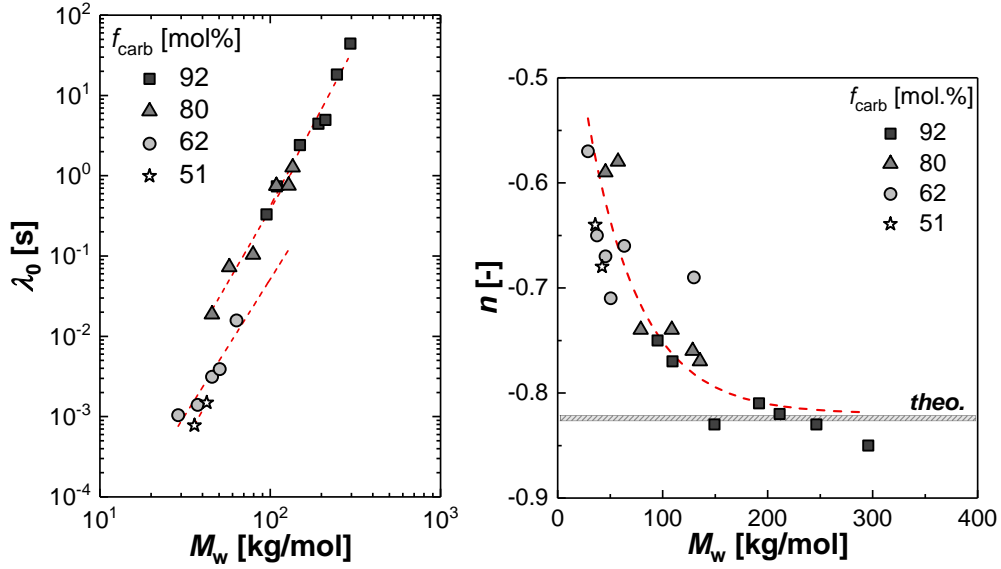


Figure 5.44 Left: Relaxation times λ_0 as a function of M_w . Right: Slope of the viscosity in the power-law region n as a function of the molecular weight. With increasing molecular weights n converges the theoretical value (for narrow-distributed polystyrene) of $n = -0.82$.¹⁸¹ the slope n is a measure for the disentangling of polymer chains and thus is depending on the polymer structure.

Figure 5.45 shows that the zero-shear viscosity increases with higher carbonate contents. The molecular weight dependence of η_0^* can be described by Equation 5.17.

$$\eta_0^* = K \cdot M_w^a \quad (5.17)$$

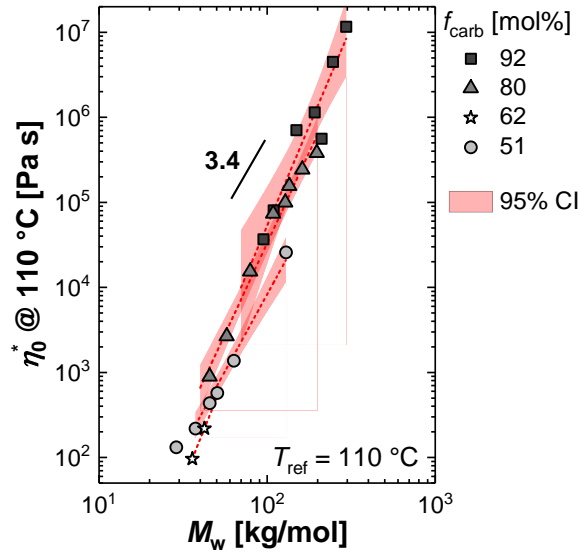


Figure 5.45 Molecular weight dependence of the zero-shear viscosity η_0^* of PPC with different compositions at $T_{\text{ref}} = 110$ °C.

Table 5.16 Slope a of the double-logarithmic plot of M_w vs η_0 @ 110 °C for PPC with different compositions and coefficient of determination for the fits according to Eq. 5.17.

f_{carb} [mol%]	a	R^2
92	4.7 ± 0.6	0.92
80	4.3 ± 0.2	0.98
62	3.6 ± 0.2	0.99
51	5.0	-

Melts of linear polymers usually show a value for the exponent a of about 3.4.¹⁸² This has also been explained in terms of reptation theory.^{183–185} The more accurate determination in this series shows in extension to the rather crude evaluation in Figure 5.35, that exponents of $a > 3.4$ are observed for all of the analyzed polymer melts (Figure 5.45; Table 5.16). It is, thus, hypothesized, that associative interactions exist between the chains at small strain amplitudes with a time domain larger than λ_0 . No significant change in a is observed with changing the composition from $f_{carb} = 51 - 92$ mol%.

5.4.2 Large amplitude oscillatory shear conditions

Most thermoplastic processing operations, *e.g.* film blowing or injection molding, are typically performed under large strain amplitudes and high frequencies that can exceed 10^6 s⁻¹.¹⁸⁶ Understanding the viscoelastic behavior of polymer melts under these process-relevant conditions is therefore crucial. The rheological behavior under large deformations requires especial attention as the elastic storage modulus G' and the viscous loss modulus G'' are becoming functions of the strain amplitude γ_0 . Concomitantly, the viscoelastic response of complex systems differs from the linear regime under SAOS conditions, giving rise to a non-sinusoidal stress response. The mathematical models applied in the SAOS region are, thus, no longer sufficient to describe complex fluids under medium and large strain amplitudes. However, the non-linear viscoelastic response under these conditions can be evaluated in other mathematical frameworks.¹⁰²

Plotting the linear moduli G' and G'' as a function of the strain amplitude according to HYUN allows to generalize four general types of LAOS behavior for complex fluids: strain-thinning (type I, G' and G'' decreasing), strain hardening (type II, G' and G'' increasing), weak strain overshoot (type III, G' decreasing, G'' increasing and subsequently decreasing) and strong strain overshoot (type IV, G' and G'' increasing and subsequently decreasing).¹⁰³ The investigated PPC melts show strain-softening behavior under large deformations (Figure 5.46), which intensifies at higher frequencies (*vide infra*). The decrease of G'_1 and G''_1 represents type I non-linear behavior according to HYUN¹⁰³ and originates from the orientation of the chains in flow direction, with analogy to shear-thinning. The onset of the strain-induced softening shifts

towards lower strains with increasing frequencies. Type I non-linear behavior is generally observed for thermo-rheological simple polymer systems.

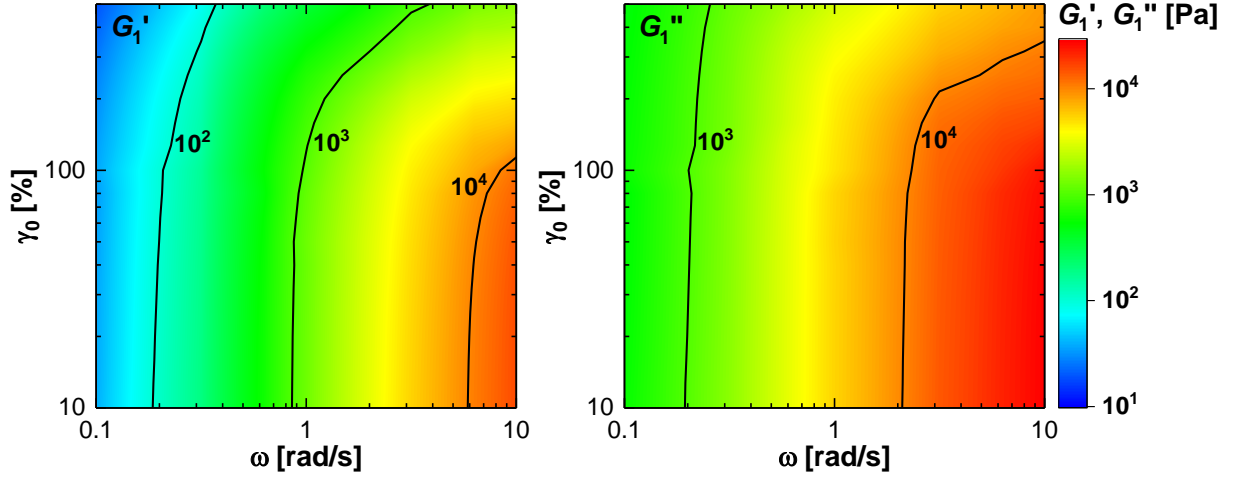


Figure 5.46 First-harmonic storage (left) G'_1 and loss moduli (right) G''_1 as function of the strain γ_0 and the excitation frequency ω . Upon increasing of the amplitude, G'_1 and G''_1 become strain-dependent. PPC with $f_{\text{carb}} = 92$ mol% and $M_w = 110$ kg/mol was measured.

To quantify the non-linear stress response the data can be displayed either in a time- or a deformation-domain. The former approach comprises the transformation of the stress function $\sigma(t)$ into a FOURIER series based on the higher harmonics of the excitation frequency ω . The second method uses orthogonal stress decomposition of the total stress into an elastic $\sigma'(\gamma(t))$ and a viscous $\sigma''(\dot{\gamma}(t))$ contribution.

FOURIER transformation rheology

The raw data was processed using the MITlaos software developed by EWOLDT, WINTER, and MCKINLEY.¹⁸⁷ The FT-rheology expresses the total stress response $\sigma(t, \omega, \gamma_0)$ as a FOURIER series with defined elastic and viscous FOURIER coefficients G'_n and G''_n according to Equation 5.18¹⁸⁸

$$\sigma(t, \omega, \gamma_0) = \gamma_0 \sum_{n, \text{odd}} \{G'_n(\sin n \cdot \omega t) + G''_n(\omega_1 \cdot \cos(n \cdot \omega t))\} \quad (5.18)$$

The FT spectrum shows the intensity I_1 of the excitation frequency as well as intensities of higher harmonics I_n , as expressed by Equation 5.19.

$$I_n = \sqrt{G'^2_n + G''^2_n} \quad (5.19)$$

Figure 5.47 shows the normalized FT spectra of a PPC melt ($M_w = 110$ kg/mol, $f_{\text{carb}} = 92$ mol%) at $\gamma_0 = 398$ % and $\omega = 6.31$ rad/s. The FT spectrum shows three significant higher harmonics ($I_{3/1}$, $I_{5/1}$ and $I_{7/1}$) displaying the deviation from ideal linear viscoelastic behavior. The FT spectra of the LAOS measurements were used to reconstruct a noise-reduced signal for the subsequent stress decomposition method. The distorted sinusoidal stress response displays forward tilted stress shape which is typical for linear polymer melts.

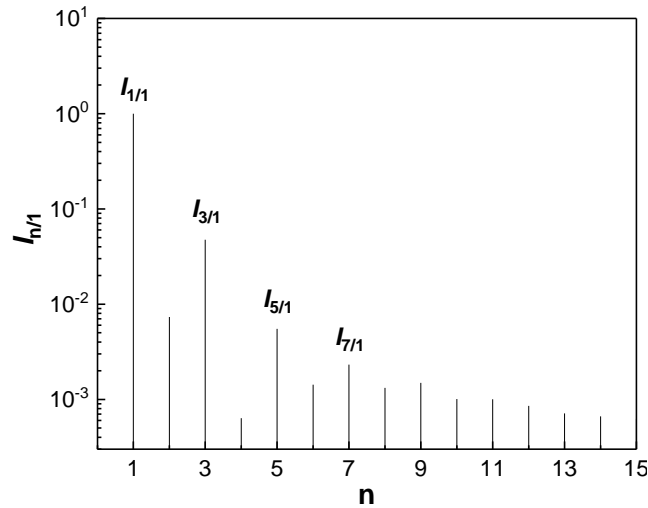


Figure 5.47 FOURIER transformation of the distorted non-sinusoidal stress response into a FOURIER spectrum showing the relative intensity $I_{n/1}$ of normalized harmonics ω/ω_1 . Excitation angular frequency $\omega_1 = 6.31$ rad/s, strain $\gamma_0 = 398$ %. PPC with $f_{\text{carb}} = 92$ mol% and $M_w = 110$ kg/mol was measured.

The degree of non-linearity can be expressed by the ratio of the third to the first harmonic $I_{3/1}$. Figure 5.48, left displays the non-linearity as a function of the strain amplitude at 1 rad/s. Under small strain amplitudes, no higher harmonics are observable in the FT spectra as the intensity ratio reaches the resolution limit. At intermediate strain amplitudes, a transition region between linear viscoelastic (small amplitude oscillatory shear, SAOS) and extensive non-linear behavior (large amplitude oscillatory shear, LAOS) is observed. This intermediate region under medium amplitude oscillatory shear (MAOS) conditions is characterized by the onset of non-linear effects. The intensity ratio $I_{3/1}$ typically scales with a factor of 2 with the deformation amplitude in the MAOS region.^{189–191} When further increasing the strain amplitude, the slope decreases slightly.¹⁹¹

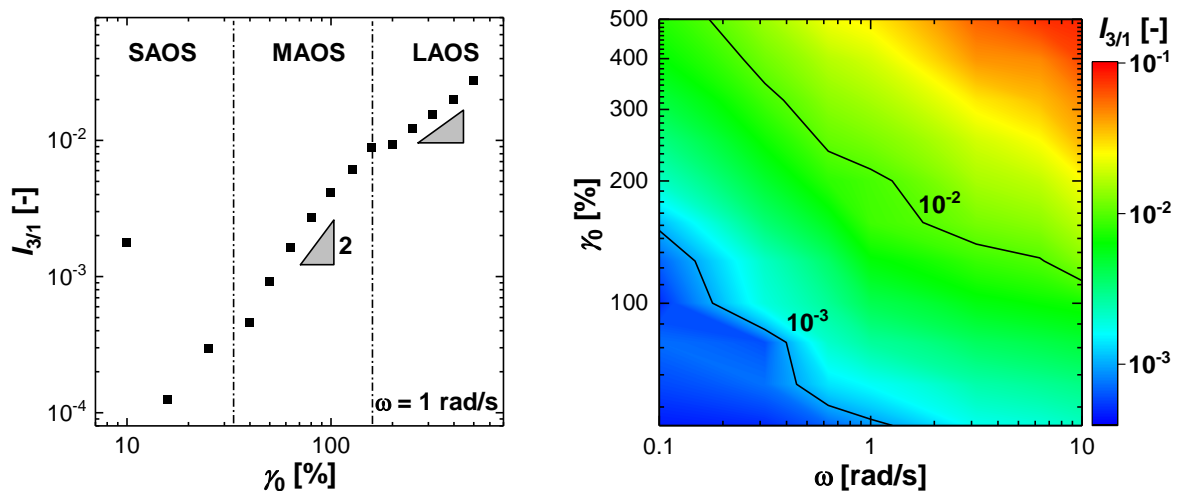


Figure 5.48 Left: Non-linear intensity ratio $I_{3/1}$ at $\omega = 1$ rad/s as a function of the strain amplitude. Right: Intensity ratio $I_{3/1}$ as a measure of the non-linearity in dependence on the strain amplitude γ_0 and the excitation angular frequency ω at $T = 140$ °C. PPC with $f_{\text{carb}} = 92$ mol% and $M_w = 110$ kg/mol was measured.

The non-linearity increases gradually with increasing deformations and frequencies (Figure 5.48, right). The increase in $I_{3/1}$ appears to correlate with the strain-softening at higher

strains and frequencies (Figure 5.47). The degree of non-linearity can also be expressed using the strain-independent zero-shear non-linearity 3Q_0 according to Equation 5.20

$${}^3Q_0 = \lim_{\gamma_0 \rightarrow 0} {}^3Q = \lim_{\gamma_0 \rightarrow 0} \frac{I_{3/1}}{\gamma_0^2} \quad (5.20)$$

with the intrinsic non-linearity 3Q . Figure 5.49 displays the impact of the molecular weight on the zero-shear non-linearity for PPC melts with $f_{\text{carb}} = 80$ and 92 mol%.

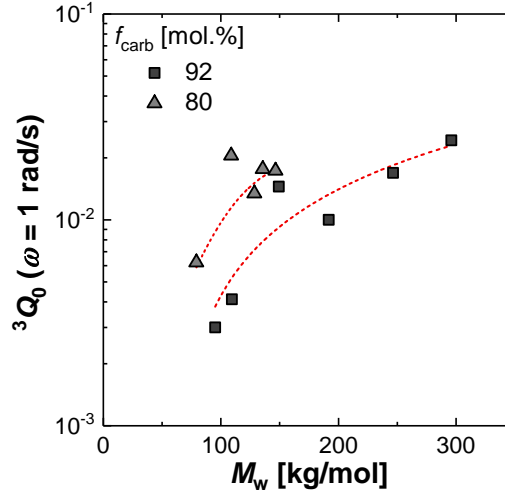


Figure 5.49 Zero-shear non-linearity 3Q_0 for PPC melts at $\omega = 1$ rad/s as a function of M_w for different carbonate contents ($T = 140$ °C).

PPC with $f_{\text{carb}} = 80$ mol% shows higher degrees of non-linearity at comparable molecular weights. The intrinsic non-linearity may arise from the associative interactions between the polymer chains as discussed above. When decreasing f_{carb} from 92 to 80 mol% the chain rigidity decreases due to the incorporation of more flexible ether linkages. It may be hypothesized, that this higher mobility in the melt state facilitates the alignment of the polymer chains under shearing conditions giving rise to higher values for 3Q_0 .

Orthogonal stress decomposition

To overcome the lack of a physical interpretation of G' and G'' in LAOS flow, a geometrical framework was constructed to allow a stress decomposition into $\sigma'(\gamma(t))$ and a viscous contributions $\sigma''(\dot{\gamma}(t))$ (Equation 5.21)¹⁰⁴

$$\sigma(t, \omega, \gamma_0) = \sigma'(\gamma(t)) + \sigma''(\dot{\gamma}(t)) \quad (5.21)$$

Following this approach, EWOLDT used CHEBYSHEV polynomials T_n as fundamental functions to decompose the viscoelastic response (Equation 5.22)

$$\sigma'(x) + \sigma''(y) = \gamma_0 \sum_{n, \text{odd}} e_n(\omega, \gamma_0) \cdot T_n(x) + \dot{\gamma}_0 \sum_{n, \text{odd}} v_n(\omega, \gamma_0) \cdot T_n(y) \quad (5.22)$$

with the elastic and viscous CHEBYSHEV coefficients e_n and v_n and $x = \gamma/\gamma_0$ and $y = \dot{\gamma}/\dot{\gamma}_0$ to provide the orthogonality. The corresponding CHEBYSHEV coefficients enable a quantification of the non-linearity.¹⁰⁵ Non-linear moduli G'_M and G'_L were introduced that are derived from the CHEBYSHEV coefficients as

$$G'_M \equiv \left. \frac{d\sigma}{d\gamma} \right|_{\gamma=0} \approx e_1 - 3e_3 + 5e_5 - 7e_7 + \dots \quad (5.23)$$

$$G'_L \equiv \left. \frac{d\sigma}{d\gamma} \right|_{\gamma=\pm\gamma_0} \approx e_1 + e_3 + e_5 + \dots \quad (5.24)$$

The moduli describe the elastic response at minimum ($\gamma = 0$) and maximum strain ($\gamma = \gamma_0$). In a similar manner, dynamic viscosities η'_M and η'_L can be obtained using the viscous CHEBYSHEV coefficients v_n . The graphical visualization of the total stress response as a function of the strain or the strain-rate are referred to as elastic and viscous LISSAJOUS-BOWDITCH figures, respectively (Figure 5.50). The minimum strain modulus and viscosity are obtained by the slope of the tangent at zero strain and strain-rate, respectively. In contrast, the large strain modulus and viscosity are defined by the slope of the secant at maximum strain and strain-rate, respectively.

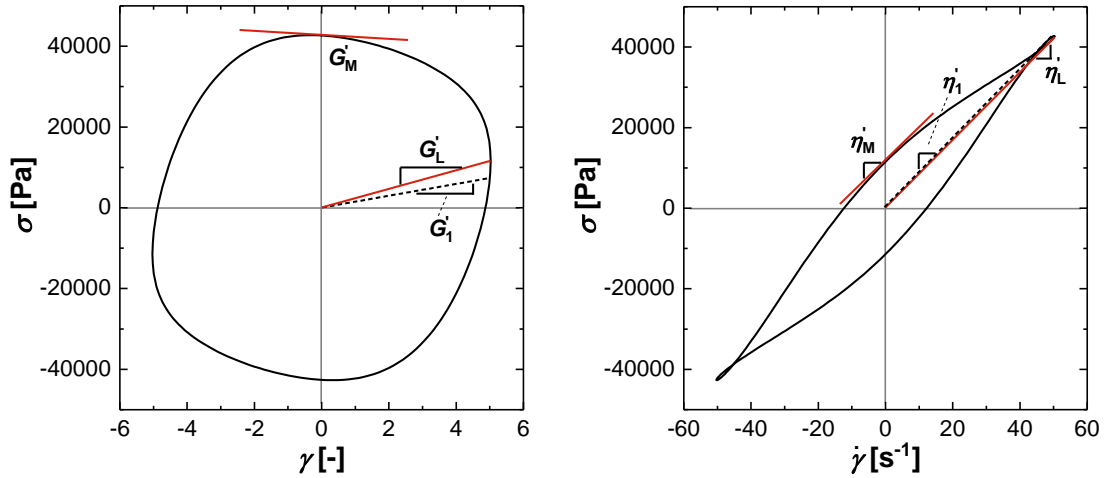


Figure 5.50 Elastic (left) and viscous LISSAJOUS-BOWDITCH plot (right) and geometrical definition of the non-linear moduli G'_M and G'_L and η'_M and η'_L ($T = 140$ °C, $\omega = 10$ rad/s, $\gamma_0 = 500$ %). G'_1 and η'_1 are defined as the first elastic modulus and the first dynamic viscosity. PPC with $f_{\text{carb}} = 92$ mol% and $M_w = 110$ kg/mol was measured.

Figure 5.51 displays the normalized elastic and viscous LISSAJOUS-BOWDITCH plots at different frequencies and strains. In agreement to the results of the FT-rheology, a significant deviation from the linear behavior is observed at increasing deformations as the curves of the total stress vs strain become increasingly rectangular. The rheological behavior is predominantly viscous in origin as the viscous stress contribution is close to the total stress response especially at low frequencies (Figure 5.51, right).

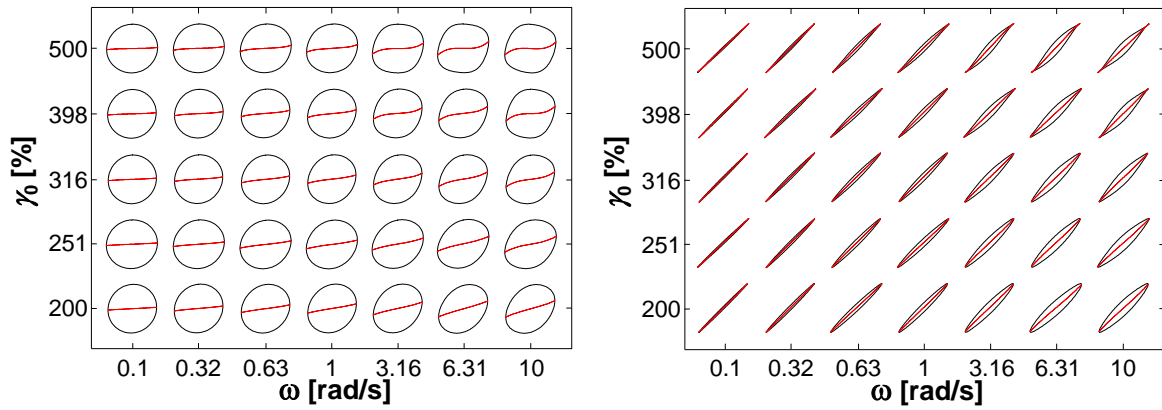


Figure 5.51 Normalized elastic (left) and viscous (right) LISSAJOUS-BOWDITCH figures for PPC melts ($M_w = 110$ kg/mol, $f_{\text{carb}} = 92$ mol%) in the $\{\omega\text{-}\gamma_0\}$ -PIPKIN space. $T = 140$ °C. The red lines correspond to the normalized elastic stress $\sigma'(t)/\sigma_{\text{max}}$ and normalized viscous stress $\sigma''(t)/\sigma_{\text{max}}$, respectively.

The non-linear moduli converge to their linear counterparts G'_1 and η'_1 from the SAOS regime at smaller strains. In contrast, intracycle strain-stiffening is observed at $\gamma > 200$ % as an upturn of the elastic stress in the LISSAJOUS-BOWDITCH plot (Figure 5.52).

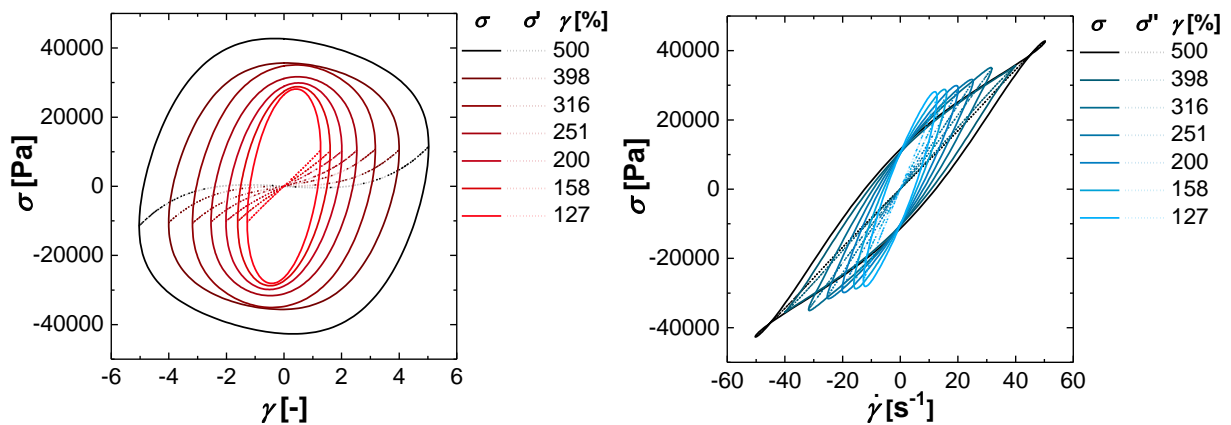


Figure 5.52 Left: LISSAJOUS-BOWDITCH curves for PPC melt ($M_w = 110$ kg/mol, $f_{\text{carb}} = 92$ mol%) with total (σ) and elastic stress (σ') as a function of the strain at various strain amplitudes from $\gamma_0 = 127 - 500$ %. Right: Total and viscous stress (σ'') as a function of the strain-rate at various strain amplitudes from $\gamma_0 = 127 - 500$ %. $T = 140$ °C, $\omega = 10$ rad/s.

The strain-stiffening becomes more pronounced at increasing molecular weights as the melts exhibit a stronger elastic response (Figure 5.53).

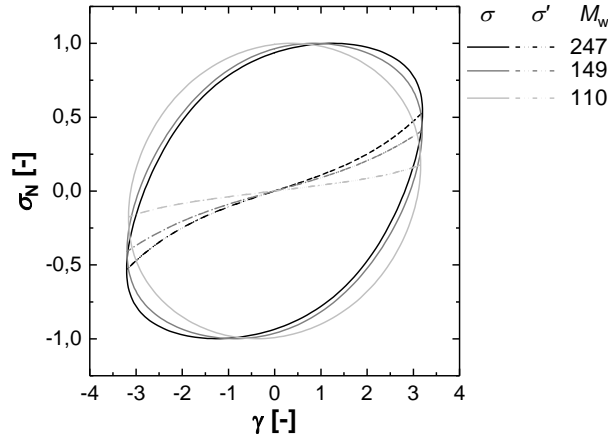


Figure 5.53 LISSAJOUS-BOWDITCH curves for PPC melts ($f_{\text{carb}} = 92$ mol%) with total (σ) and elastic stress (σ') as a function of M_w at a strain amplitude of $\gamma_0 = 316$ %.

The intracycle strain-stiffening results from a deviation of the slope of the secant at minimum strain and the tangent at maximum strain, *i.e.* the non-linear moduli G'_M and G'_L with increasing strain amplitude (Equation 5.25). To quantify this behavior a strain-stiffening ratio S was introduced that is defined as¹⁹²

$$S = \frac{G'_L - G'_M}{G'_L} \quad (5.25)$$

The strain-stiffening ratio S describes the relative increase of the elastic modulus between zero and maximum strain. The ratio S is higher at higher deformations and shows little to no dependence on the excitation frequency (Figure 5.54, left).

In analogy to the elastic moduli, the relative intracycle change of the dynamic viscosities may be quantified using the shear-thickening ratio T (Equation 5.26)

$$T = \frac{\eta'_L - \eta'_M}{\eta'_L} \quad (5.26)$$

The dynamic viscosities show shear-thinning at large deformations ($\gamma_0 > 500$ %) that is preceded by an intra-cycle shear-thickening at intermediate strains (Figure 5.54, right). The appearance of an intracycle shear-thickening prior to the strain-induced thinning is observed for all frequencies in the range of $\omega = 0.32 - 10$ rad/s. At frequencies of 0.1 rad/s no shear-thinning is observed. The measured values for T are higher at higher frequencies.

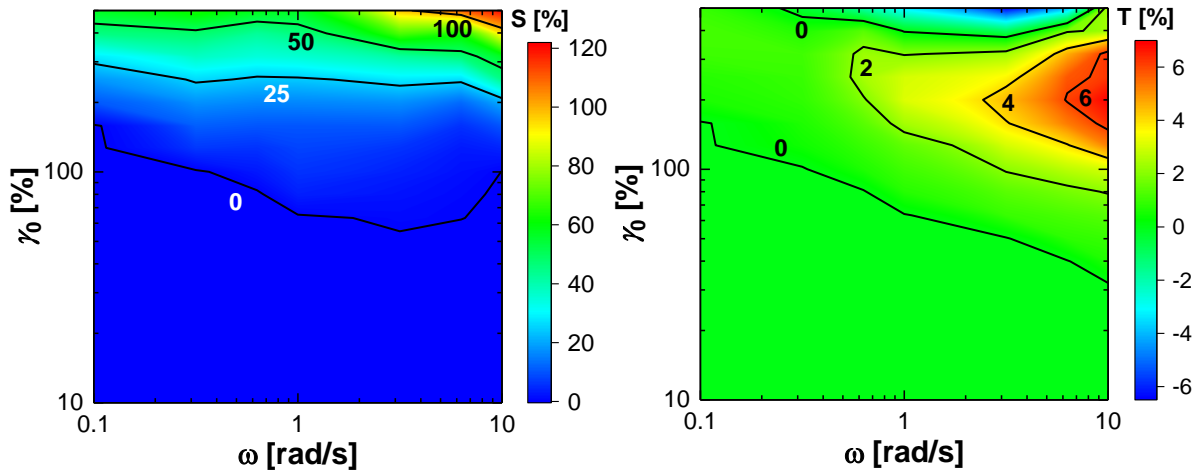


Figure 5.54 Contour plots of the strain-stiffening ratio S (left) and the shear-thickening ratio T (right) displayed in the $\{\omega, \gamma_0\}$ -PIPKIN space for PPC melt ($M_w = 110$ kg/mol, $f_{\text{carb}} = 92$ mol%) at 140 °C.

Polymer melts of similar M_w with a lower carbonate content ($f_{\text{carb}} = 80$ mol%) show a comparable strain dependence of S . The shear-thickening ratio T of melts with $f_{\text{carb}} = 80$ mol% shows an earlier onset of the intracycle shear-thickening with higher maximum values (Figure 5.55).

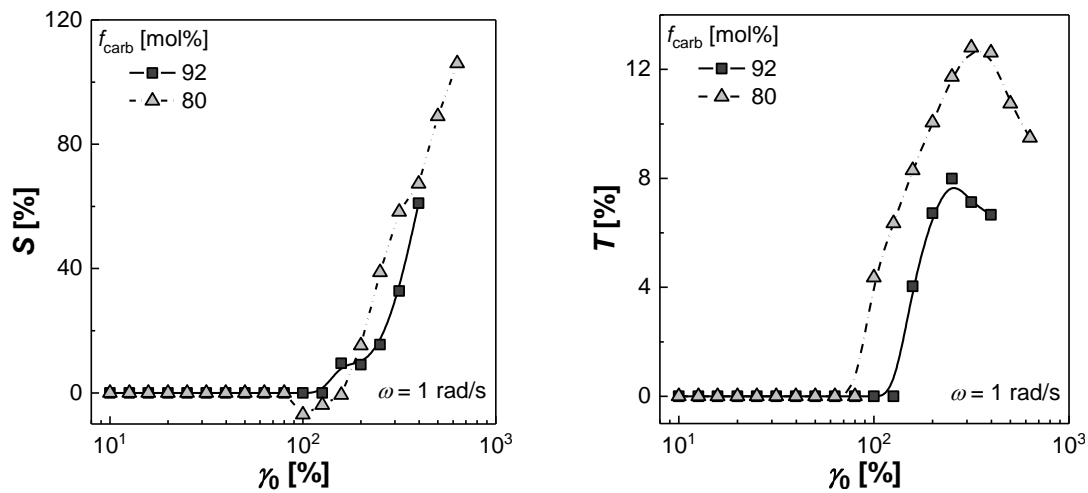


Figure 5.55 Strain-stiffening ratio S (left) and shear-thickening ratio T (right) for PPC melts ($M_w = 149$ and 147 kg/mol) with compositions of $f_{\text{carb}} = 92$ and 80 mol% as a function of the strain amplitude γ_0 .

Differences in the non-linear viscoelastic response of PPC melts in dependence on the polymer composition are not fully understood and require further investigations. The results indicate more/stronger associative interactions in case of PPC melts with $f_{\text{carb}} = 80$ mol%, compared with PPC with higher carbonate contents.

5.5 CO₂/epoxide cycloaddition using indium catalysts

The research for the following chapter was conducted within a DAAD funded short-term internship at the University of British Columbia in the group of Professor Parisa Mehrkhodavandi.

The utilization of CO₂ as a C₁-feedstock in chemical industry has gained increasing interest in the last decades as it is potentially abundant, non-toxic and renewable raw material.⁵ One possible use is the spontaneous reaction with epoxides. Depending on the catalytic system (and the reaction conditions), five-membered cyclic carbonates and/or aliphatic poly(carbonates) are formed. Transition metal complexes as catalysts have been studied in detail, in particular with chromium, cobalt and zinc ions. Reports on catalysts based on main group element complexes mostly concern aluminum compounds.^{193–196} Ga(salen)X (X = Cl or N₃) compounds are reported to be inactive for the reaction of cyclohexene oxide (CHO) with CO₂.¹⁹⁷ Studies on indium-based catalysts for the coupling of epoxides with CO₂ are scarce.^{198–201} Indium catalysts are known to be insensitive to air and moisture²⁰² and show a remarkable functional group tolerance, thus, allowing catalytic transformations even in aqueous media.²⁰³ Previous studies on a series of dinuclear indium complexes with half-salen^{204–209} and salen-type ligands²¹⁰ (Figure 5.56) revealed an unprecedented combination of high activity and stereoselectivity for the ring-opening polymerization of lactide and other cyclic esters. These results lead to the investigation of a series of indium complexes as potential catalysts for the coupling of epoxides with CO₂.

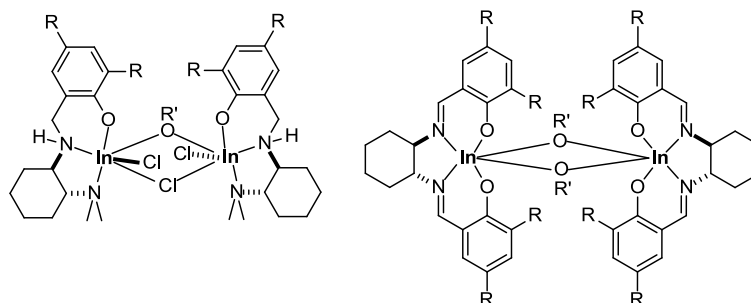


Figure 5.56 Dinuclear In(salen) catalysts for ROP of cyclic esters, *e.g.* lactide.

An initial catalyst screening was performed using PO as a model substrate. The investigated catalysts were synthesized according to literature procedures^{204,207,210,211} and range from indium halides (InX₃, X = Cl, Br or I) to a number of monomeric and dimeric indium complexes using various ligands (Figure 5.57). Bis(triphenylphosphine)iminium chloride (PPN-Cl) was utilized as co-catalyst. The results of the catalyst screening are displayed in Table 5.14. Indium halides are reported to be inactive for the cycloaddition of epoxides and CO₂, however, in combination with one equivalent of PPN-Cl conversions of 26 – 28 % were obtained (Table 5.14, entries 1 – 3). The type of indium halide does not seem to have a significant impact on the catalytic activity. The combination of both a LEWIS acid and PPN-Cl as co-catalyst, however, appears to be of importance, as the cycloaddition in the absence of either only results in low monomer conversion rates (Table 5.17, entry 16 and Table 5.18, entry 1).

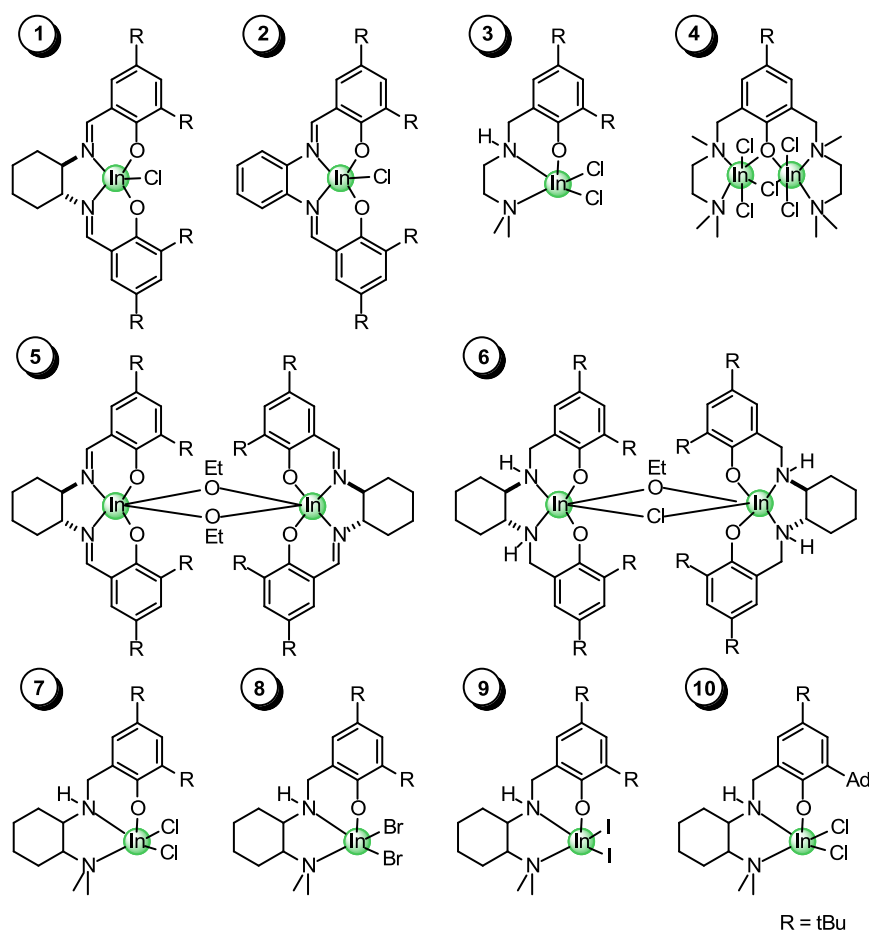


Figure 5.57 Catalyst screening for CO₂/epoxide coupling reaction.

Table 5.17 Catalytic cycloaddition of CO₂ and PO.

Entry	Catalyst	Yield ^b [%]	Entry	Catalyst	Yield ^b [%]
1	InCl ₃	26	9	6	59
2	InBr ₃	29	10	7	72
3	InI ₃	28	11 ^c	8	98
4	1	30	12 ^c	9	97
5	2	82	13	10	79
6	3	61	14 ^d	8	60
7	4	56	15 ^d	9	40
8	5	24	16	-	4

Experiments were performed using the protocol for cycloaddition of epoxides and CO₂. Reaction conditions: [PO] = 4 mol/L in toluene, [cat] = 0.1 mol%, [co-cat] = 0.1 mol%, *T* = 80 °C, *p* = 30 bar, *t* = 24 h. ^a For all catalysts the selectivity towards the cyclic carbonate was > 99 %, ^b isolated yield after purification, ^c *t* = 7 h, ^d [PO] = 1.0 mol/L in toluene, *t* = 7 h.

The mononuclear In(salphen)Cl (**2**) shows higher conversion rates than complex **1**, bearing a salen-backbone. This finding is in agreement with previous studies²¹² and may be attributed to the increased LEWIS acidity of the indium in **2**. The alkoxy-bridged dimers **5** and **6** show the same activity, possibly because of its dissociation in solution. Of all investigated catalytic systems, complexes **8** and **9** showed the highest activity, allowing complete conversion of PO

within 7 h to form the cyclic carbonate cPC selectively. Interestingly, further experiments revealed that contrasting to earlier observations, the nature of the halide affects the catalytic properties of the utilized indium catalyst. The activity increases in the order $\text{Cl}^- < \text{I}^- < \text{Br}^-$. The impact of different types of co-catalyst on the cycloaddition reaction was investigated showing the highest conversion rates with PPN-Cl as co-catalyst (Table 5.18). The impact of a co-catalyst in such binary catalyst-systems has been subject of previous investigations.^{124,213}

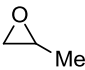
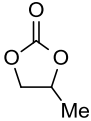
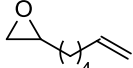
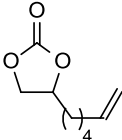
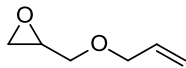
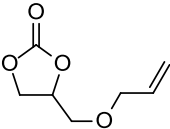
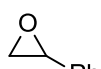
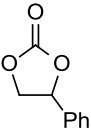
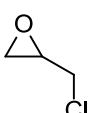
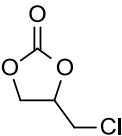
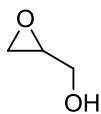
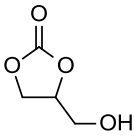

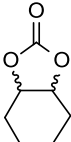
Table 5.18 Catalytic activity of 8 with various co-catalysts in the cycloaddition of CO_2 and PO.

Entry	Co-catalyst	[cat]/[co-cat]	Yield ^a [%]
1	-	-	0.5
2	PPN-Cl	1	60
3	TBAB	1	44
4	TBAI	1	43
5	TBAOAc	1	38

Experiments were performed using the protocol for cycloaddition of epoxides and CO_2 . Reaction conditions: [PO] = 1.0 mol/L in toluene, [cat] = 0.1 mol%, $T = 80\text{ }^\circ\text{C}$, $p = 30\text{ bar}$, $t = 7\text{ h}$. ^a Isolated yield.

The functional group tolerance of the used indium catalysts was screened for various epoxide substrates (Table 5.19). The cycloaddition of most mono-substituted epoxides with CO_2 can be performed with high yields of the expected products. The catalyst shows an excellent tolerance for functional groups such as olefins, halides and alcohols. The coupling reaction of 1,2-epoxy-7-octene and styrene oxide with CO_2 , however, only gave relatively low conversions, possibly due to the negative inductive effect of the phenyl substituent, contrary to the positive polarization induced by the other substituents. In addition to the mono-substituted epoxides, CHO was investigated as substrate. The coupling reaction showed a similar behavior as for other epoxides with sterically demanding substituents as only very low yields of the *meso*-cyclohexene carbonate as a main product were obtained. Similar behavior is observed in the literature for various types of metal-salen complexes.²¹²

Table 5.19 Yield for the cycloaddition of several epoxides with CO₂ using catalyst 8.

Epoxide	Product	Yield ^b [%]
		91
		70
		93
		21
		88
		81
		4

Experiments were performed using the protocol for cycloaddition of epoxides and CO₂. Reaction conditions: [PO] = 0.5 mol/L in toluene, [cat] = 0.2 mol%, $T = 80\text{ }^{\circ}\text{C}$, $p = 30\text{ bar}$, $t = 24\text{ h}$. ^a Determined by ¹H-NMR, ^b isolated yield.

All indium catalyst used in this study exhibit high selectivity for the formation of the cyclic carbonates as no side product formation, *i.e.* poly(ether) or poly(carbonate), is observed. This may be explained under the assumption of a rapid dissociation from the metal center followed by ring formation. This has been proposed for similar aluminum based salen-complexes.³⁵

5.6 Initially active double metal cyanide catalysts

Zinc dicarboxylates are considered as industrially viable catalysts for the copolymerization of CO₂ and epoxides. State-of-the-art are nanoscopic ZnGA catalysts prepared by the thermal decomposition of ZnGA-alkyl amine adducts.^{62,66,109} Nanoscopic amine-modified ZnGA exhibits remarkable activities compared with older zinc dicarboxylates.⁵⁹ In this chapter, the synthetic approach for the preparation of amine modified ZnGA catalysts is applied to another class of industrially relevant complexes for alkoxylation, double metal cyanides (DMC). Previous studies already had shown a proof of concept.^{214,215} Here, the synthetic procedures were further optimized and the obtained catalysts structurally characterized.

DMCs are a group of complexes that find application in catalytic conversions, *e.g.* as polymerization catalysts for polycondensation of diols and diacids²¹⁶, the ring-opening polymerization of epoxides as well as their co- and terpolymerization with other epoxides²¹⁷, with CO₂^{21,57,147,218–220} and with cyclic anhydrides^{221–223}. While showing in part excellent catalytic properties, one major drawback of DMC catalysts is that they generally feature an induction period of unknown length, ranging from several minutes up to hours, during which no substantial propagation is observed (Figure 5.58).^{158,160} The spontaneous initiation of an exothermic polyreaction with PO is accompanied with the development of considerable heat of reaction and therefore comprises a serious safety issue. In addition, the overall space-time-yield is reduced. The length of the induction period is affected by factors such as the procedure of catalyst preparation itself and the presence of water or other low molecular weight compounds like glycerol.^{224,225} Up to this date, no reliable model exists that allows to predict the length of this activation step. After the induction period, the catalyst is considered active and consequently the propagation rate accelerates.

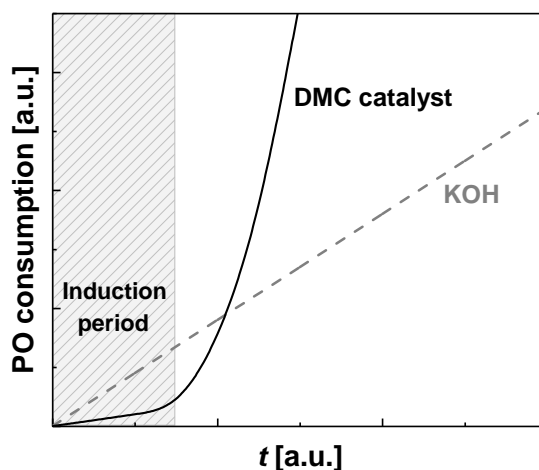


Figure 5.58 Exemplary comparison of conversion rates for DMC and KOH-catalyzed homopolymerization of PO. DMC catalysts typically show an induction period of several minutes up to hours during which only low monomer conversion is observed.

Another drawback of common DMC catalysts is that they typically exhibit low selectivities towards CO₂ incorporation upon copolymerization with epoxides, hence predominantly yielding poly(ether carbonates) with a large part of ether linkages.^{166,226}

In the following chapter an alternative synthetic pathway is offered that gives access to DMC catalysts that feature remarkable catalytic properties for epoxide homo- and copolymerization with CO₂. The synthesis and characterization of these DMC catalysts and their use as polymerization catalysts is presented. The impact of the synthetic procedure on the catalytic properties is investigated.

5.6.1 Synthesis of amine-modified double metal cyanide catalysts

The catalytic properties of DMCs are drastically affected by the preparation method as well as the type of starting materials.^{227–234} DMC based on Zn and Co catalysts are generally prepared by co-precipitation of an excess ZnCl₂ with K₃[Co(CN)₆] in the presence of complexing agents such as *tert*-BuOH.^{235–237} While Zn/Co-DMC catalysts are superior in their catalytic performance, a number of other metal cyanides can be utilized as well.^{58,219,220,232,238,239}

Here, the new preparative approach comprises a template-controlled synthesis using long-chain *n*-alkyl amines as surfactant/structure-directing agent and Zn(NO₃)₂ as a source for Zn²⁺. In a first step, the catalytic precursor is formed that yields the active catalytic species upon thermal treatment and partial removal of the amine (Figure 5.59).

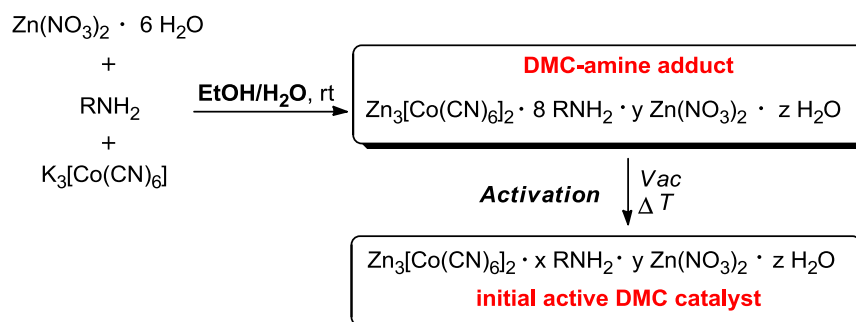


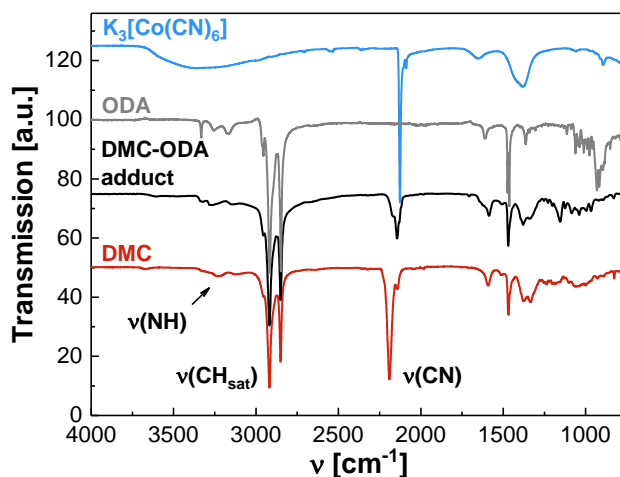
Figure 5.59 Scheme for the preparation of Co/Zn-DMC-alkyl amine catalysts.

The synthesis of catalytic precursors was performed by co-precipitation procedure using *n*-alkyl amines (C12 – C18). The synthesis of the catalyst precursors was carried out in different ethanol/water mixtures to overcome the poor miscibility of the amines with water. Precursors prepared from 14/86 (EtOH/H₂O, v/v) mixtures show superior activities after thermal treatment (Chapter 5.6.3 and 5.6.4). Moreover, thorough work-up of the catalytic precursor proved to be crucial, as traces of side products (mainly potassium nitrate) drastically decrease the catalytic activity (*vide infra*).²³⁴ The catalytic precursors were structurally characterized by means of elemental analysis (EA; Table 5.20), FTIR, XRD and SEM. According to EA, the catalytic precursors contain an excess of Zn over Co, *i.e.* 2.0 > Zn/Co > 1.5. Hence, the following structural formula is proposed for the DMC-amine adducts: Zn₃[Co(CN)₆]₂ · *a* NH₂(CH₂)_{*n*}CH₃ · *b* Zn(NO₃)₂ · *c* H₂O. All samples contain traces of KNO₃ as a main impurity.

Table 5.20 Elemental composition of Zn/Co-DMC-amine adducts. Values in parentheses are theoretical values calculated for $Zn_3[Co(CN)_6]_2 \cdot a NH_2(CH_2)_nCH_3 \cdot b Zn(NO_3)_2 \cdot c H_2O$ with $n = 12 - 18$.

Amine	[wt.%]							Zn/Co	<i>a</i> Amine	<i>b</i> Zn(NO ₃) ₂	<i>c</i> H ₂ O
	C	H	N	O	Zn	Co	K				
C12	58.4 (58.5)	9.9 (9.9)	13.4 (13.3)	2.6 (2.6)	10.3 (10.4)	5.3 (5.3)	0.08 (0.07)	1.76	8	0.49	0.5
C14	60.3 (60.5)	10.1 (10.3)	12.2 (12.0)	3.1 (3.1)	9.3 (9.2)	4.8 (4.8)	0.14 (0.14)	1.74	8	0.46	1.7
C16	62.8 (62.8)	10.6 (10.7)	10.9 (10.9)	2.7 (2.7)	8.4 (8.3)	4.4 (4.4)	0.19 (0.19)	1.70	8	0.38	1.9
C18	64.3 (63.8)	10.9 (10.8)	10.1 (10.2)	3.0 (3.0)	7.9 (8.1)	3.9 (4.0)	0.04 (0.04)	1.83	8	0.63	1.7

The amines are believed to be chemically integrated into the Zn/Co-complex as they are not removed during workup (washing) with ethanol. This is further verified by a shift of the N-H stretching vibrations in the FTIR spectra as result of the coordination of the amine-entities (Figure 5.60). The spectra show characteristic absorptions at 2916 and 2849 cm^{-1} and 1467 cm^{-1} that can be attributed to CH-stretching and CH-deformation vibrations, respectively. The CN-absorption at 2145 cm^{-1} is blue-shifted relative to the absorptions of $K_3[Co(CN)_6]$ as result of the complexation to Zn^{2+} . After the thermal treatment the CN-stretching vibration is further blue-shifted to 2189 cm^{-1} .

**Figure 5.60** FTIR spectra of $K_3[Co(CN)_6]$ (blue), octadecylamine (ODA) (grey), the DMC-ODA adduct (black) and of the activated catalyst (red).

The catalytic precursors and activated catalysts were further analyzed by means of powder XRD (Figure 5.61). The crystallinity was not quantified on account of missing data for the heat of fusion of Zn/Co-DMC complexes; the analysis thus is only qualitative. The DMC catalysts are semicrystalline/amorphous with neither the DMC-amine adduct, nor the activated DMC catalyst showing typical sharp reflexes for crystalline $Zn_3[Co(CN)_6]_2$ at $2\theta = 17.5^\circ$, 24.8° , 35.3° and 39.5° .²⁴⁰ The amine-adducts, however, show broad reflexes around 21.2° that appear to broaden with increasing amine chain length. The catalysts precursors show reflexes characteristic for layered structures, *i.e.* reflections of successive *d*-planes (Figure 5.61, left). The

corresponding d -spacings increase linearly with increasing chain lengths of the amine. These observations are reminiscent of comparable Zn-alkyl amine adducts, reported in the literature.^{67,241}

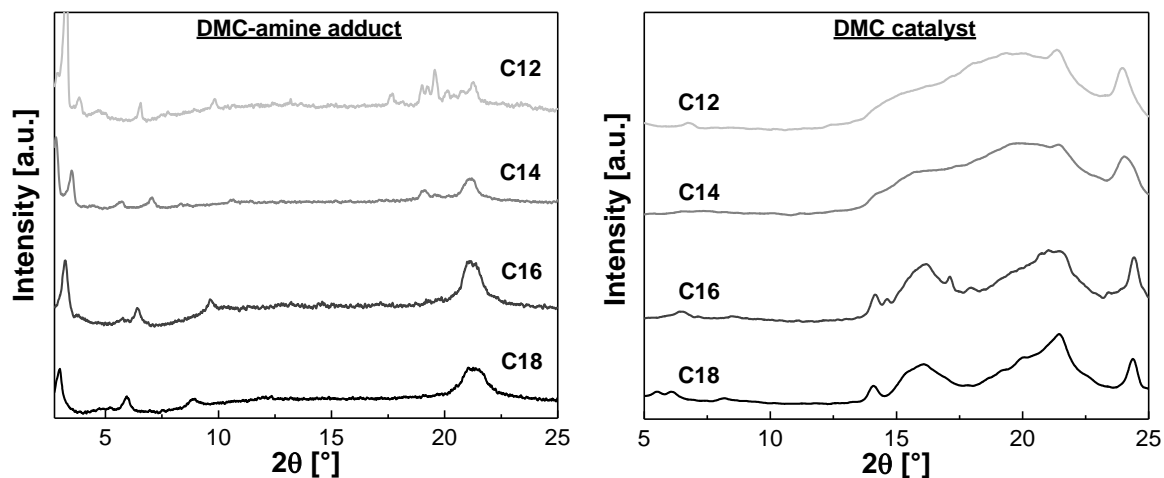


Figure 5.61 Left: X-ray powder diffractogram of the DMC-amine adducts with different chain lengths, prior to thermal treatment. Right: Diffractogram of the activated DMC catalysts modified with amine with chain lengths from C12 to C18.

After thermal treatment, the degree of crystallinity increases with the parent-amines chain length (Figure 5.61, right and 5.62). While the C12 and C14-amine containing samples show only broad melting peaks, the C16 and C18-amine based catalysts have multiple discrete melting peaks. This is opposed to the properties of the DMC-amine adducts before thermal treatment. It appears that less crystalline adducts are more easily transferred into (more crystalline) catalytic species in the transformation.

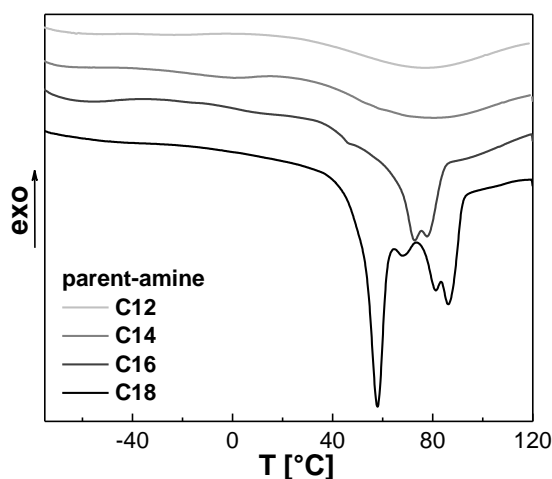


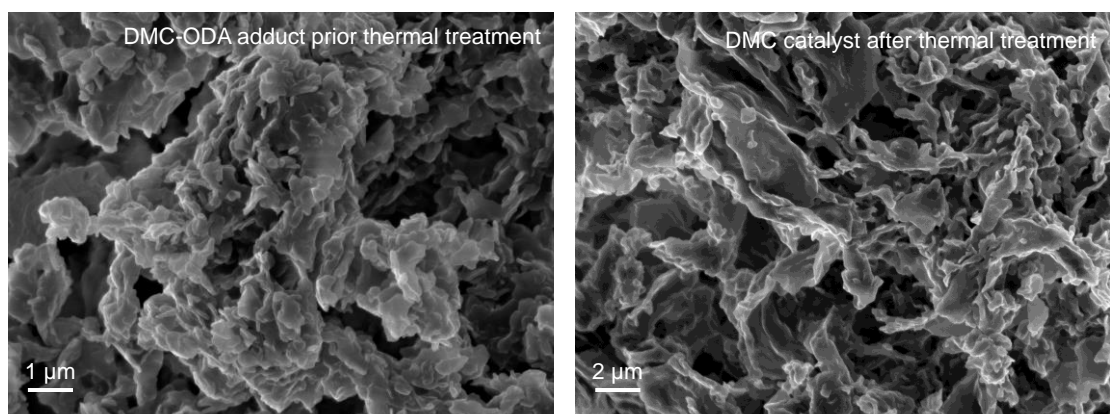
Figure 5.62 DSC trace of the thermally treated DMC catalysts with different amine chain lengths (N_2 , heating rate = 10 K/min).

The thermal treatment of the DMC-amine adducts can be understood as a conversion of the precursors followed by a distillative removal of parts of the amine. The amine is not removed entirely during this step even upon increasing the temperature. Instead, EA (Table 5.21) and FTIR (Figure 5.60) indicate residues of n -alkyl amines in the formed catalyst.

Table 5.21 Elemental composition of the thermally treated Zn/Co-DMCs. Values in parentheses are theoretical values calculated for $Zn_3[Co(CN)_6]_2 \cdot a NH_2(CH_2)_nCH_3 \cdot b Zn(NO_3)_2 \cdot c H_2O$.

Amine	[wt.%]							Zn/Co	<i>a</i> Amine	<i>b</i> Zn(NO ₃) ₂	<i>c</i> H ₂ O
	C	H	N	O	Zn	Co	K				
C12	43.0 (42.9)	6.2 (5.8)	18.1 (18.2)	4.0 (4.0)	19.0 (19.1)	9.8 (9.2)	0.09 (0.10)	1.76	2.58	0.49	0
C14	43.8 (44.3)	6.3 (6.3)	17.6 (17.1)	4.9 (4.8)	17.8 (17.8)	9.5 (9.5)	0.15 (0.13)	1.69	2.40	0.35	1.5
C16	43.8 (43.8)	6.0 (5.8)	17.7 (17.6)	3.7 (3.6)	18.7 (18.9)	9.8 (10.0)	0.34 (0.33)	1.71	1.95	0.4	0
C18	50.9 (50.2)	7.4 (7.5)	14.9 (14.6)	2.6 (4.5)	16.2 (15.6)	7.8 (7.5)	0.09 (0.07)	1.87	3.00	0.73	0

The catalysts form plate-shaped particles, which are found to build larger aggregates. The individual plates have varying sizes of several hundred nm. The resulting particle sizes are not significantly affected neither by the solvent composition during synthesis, nor by the thermal treatment (Figure 5.63).

**Figure 5.63** SEM image of DMC-ODA adduct prior to thermal treatment (left) and DMC catalyst after catalyst activation (right).

The synthetic pathway of preparing a catalyst-amine adduct in a first step and subsequently activating this precursor is a versatile procedure that can be expanded to other types of catalysts. Instead of $K_3[Co(CN)_6]$ other cyanide-containing precursors such as $K_3[Fe(CN)_6]$ and $K_4[Fe(CN)_6]^{214}$ and even dicarboxylic acids^{66,109} can be utilized as ligands giving access to Co-free catalysts.

5.6.2 *Online*-reaction monitoring and kinetic studies of DMC catalysts

The propoxylation experiments were *online*-monitored by means of *in-situ* FTIR-spectroscopy and *offline* analyzed by SEC. Purpose of the *online*-monitoring is to track the PO-concentration throughout the polymerization process. Accumulation of PO is highly undesired and needs to be prevented for safety reasons. Furthermore, the tracking of the instantaneous PO-conversion allows kinetic studies of the used catalyst. FTIR-monitoring requires the determination of a

suitable regression model. A correlation was obtained by dilution of the final product with PO, *i.e.* the autoclave was charged with the final product and PO was fed stepwise to simulate higher concentration of monomer that would be corresponding to decreasing conversions. The spectral changes of the entire spectral area upon PO-addition are displayed in Figure 5.64. At higher PO-concentrations, the absorption of the ring vibration of PO at 828 cm^{-1} increases whereas the C-O-stretching vibration of the PPG at 1100 cm^{-1} decreases.

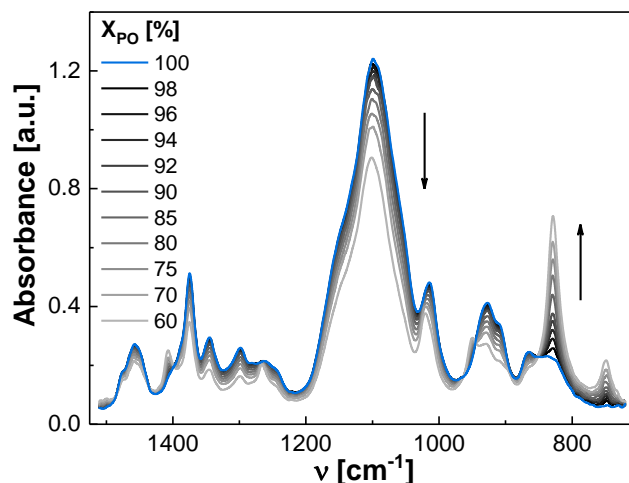


Figure 5.64 FTIR spectra of the reaction mixture at various conversions ($T = 125\text{ }^{\circ}\text{C}$).

A multivariate data analysis was performed using The Unscrambler® X to generate a PLS regression model from the spectra. The impact of different data pretreatment methods was studied by their root-mean squared errors (RMSE). The results reveal that a standard normal variate transformation (SNV) leads to the highest prediction accuracies (Table 5.22).

Table 5.22 RMSE for regression models using different data pretreatment options.

Data pretreatment	RMSE
-	0.69
Baseline	0.66
SNV	0.13
SNV + baseline	1.12

The model comprises two factors of which the first one (factor 1) covers 99 % of the spectral changes as a function of the conversion (Figure 5.65). A second factor was taken into the model to further improve the accuracy.

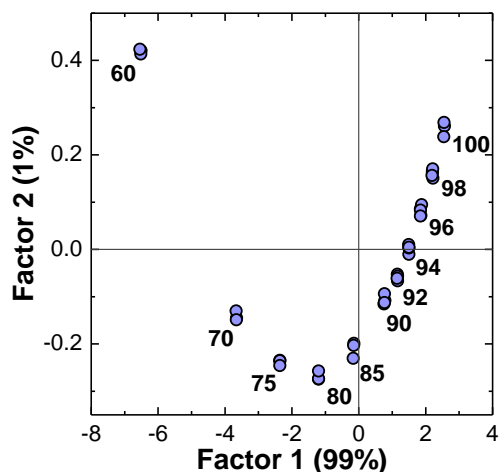


Figure 5.65 Scores-plot for two factors.

The regression model was validated by plotting the predicted against the actual conversion (Figure 5.66). The plot shows the excellent accuracy of the obtained PLS model ($R^2 > 0.999$), thus, allowing to track the instantaneous monomer conversion throughout the polymerization process.

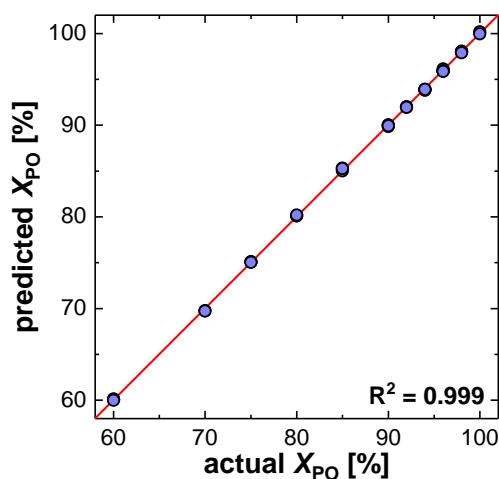


Figure 5.66 Predicted X_{PO} using the generated PLS model and actual X_{PO} ($R^2 > 0.999$).

The obtained calibration model was then used to monitor the propoxylation reactions. The FTIR-spectra for an exemplary polymerization are displayed in Figure 5.69 (Chapter 5.6.3). At initial stages, an increase in the absorption at 828 cm^{-1} is observed, followed by a rapid decrease. This corresponds to the addition of initial amount of PO and its subsequent consumption as the catalyst is activated. Following the catalysts activation, no further changes are observed in the FTIR-spectra. Using the PLS model, the monomer conversion was calculated. For all propoxylation reactions, conducted in a semi-batch mode, instantaneous conversions of $X_{PO} > 98 (\pm 2)\%$ were observed throughout the entire reaction, *i.e.* the monomer does not accumulate but is consumed instantaneously.

The chain growth of the propoxylation reaction can be described by the following equation



with the active growing chain P_n^* and the rate constant of propagation k_{pr} . The propagation rate r_{pr} thus can be expressed by the following rate law

$$r_{pr} = -\frac{d[PO]}{dt} = k' \cdot [PO] \quad \text{with } k' = k_{pr} \cdot [P^*] \quad (5.28)$$

with k' being the observed rate constant, defined as the product of the rate constant of propagation and the concentration of growing chain ends $[P^*]$ ($= [OH]$). The total number of chains is assumed to be constant. Integration of the rate law (Equation 5.28) yields an exponential dependence of the propoxylation reaction with time that may be linearized in form of Equation 5.29.

$$\ln[PO] = k' \cdot t + \ln[PO]_0 \quad (5.29)$$

Once the induction period is finished, *i.e.* the DMC catalyst is activated and the initial amount of PO is consumed, PO is fed stepwise into the reactor in pulses (feeding rate = 25 mL/min). The pulses need to be small compared to the overall volume to ensure about isothermal conditions. This method can also be used investigate the reaction kinetics as a function of the temperature using the ARRHENIUS approach, giving access to activation energies. The monomer depletion over time can be used to determine the rate constants according to Equation 5.29 (Figure 5.67).

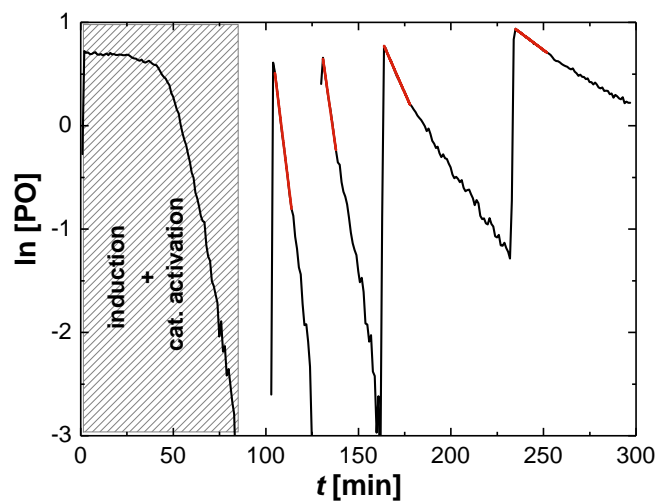


Figure 5.67 Determination of net rate constants from the PO conversion in time.

According to the model (Equation 5.28), the rate constants are a function of the concentration of the OH-groups $[OH]$. Latter need to be recalculated everytime a pulse of PO has been added. This method allows to rank the action of different DMC catalyst samples by their normalized net rate constants k_{pr} .

5.6.3 Homopolymerization of epoxides

The thermally activated DMCs were investigated regarding their catalytic properties for epoxide homopolymerizations. All catalysts proved to be active for propoxylation reactions (Table 5.23). The catalytic performance of the prepared catalysts was initially screened by batch polymerizations at low temperatures ($T = 70\text{ }^{\circ}\text{C}$). As displayed in Table 5.20, DMC18 (14/86), prepared from ODA in 14/86 ethanol/water mixture (v/v), shows the highest activity. Thorough purification of the DMC-ODA adducts proved to be crucial in order to remove traces of K^+ , which affect the catalytic properties of the final DMC complexes (Table 5.23 and 5.24).^{144,234} The polymerization experiments were monitored *in-situ* FTIR-spectroscopy and *offline* by means of SEC.

Thermal activation of the DMC-amine adducts yields DMC-type catalysts with unique properties. All amine-modified catalysts are initially active upon contact with PO (Figure 5.68) with one exception showing an induction time < 1 min. In contrast to what is typically observed for DMC catalysts, this new type of complexes does not show an induction period after addition of PO. Instead, the polymerization initiates spontaneously, even at temperatures as low as $70\text{ }^{\circ}\text{C}$. This unique feature represents a major improvement in terms of safety as the exothermic temperature peak caused by the initiation of the polyreaction can be controlled. The absence of an induction period furthermore improves the overall space-time-yields as the downtime of the reactor during the induction period is reduced. Several hypotheses may be built for the absence of an activation period. The induction period is commonly associated with reactions at the surface that lead to the coordination and thus with the activation of PO. In case of the amine-functionalized, chloride free DMC of this study, nucleophilic ring-opening of PO proceeds with a small activation energy. The underlying grounds may be related to the absence of coordination entities, like the commonly used *t*-Bu-OH or chloride, or the hydrophobicity of the alkyl amines or else. This needs detailed investigations that are not a topic in this work.

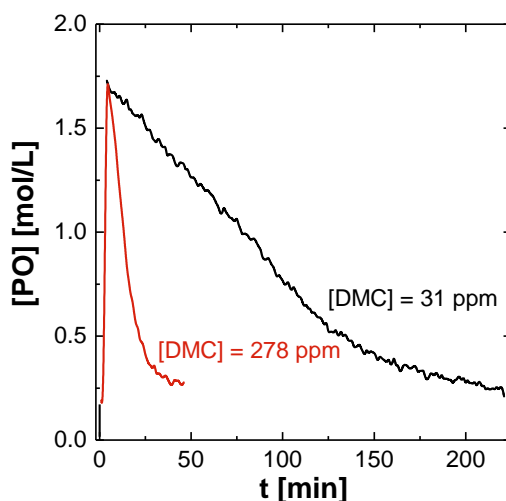


Figure 5.68 Free monomer concentration [PO] during a propoxylation reaction at $T = 120\text{ }^{\circ}\text{C}$ using DMC18 (14/86). The catalyst is suspended in PPG2000, subsequently a pulse of PO is added.

Table 5.23 Catalyst screening for the PO batch homopolymerization.

Entry	Catalyst ^a	EtOH/H ₂ O (v/v) work-up ^b	TOF ^c [h ⁻¹]	<i>t</i> _{induction} ^d [min]
1	DMC18 (100/0)	0/100	995	0
2	DMC18 (50/50)	0/100	1065	0
3	DMC18 (14/86)	0/100	1599	0
4	DMC18 (14/86)	14/86	1503	0
5	DMC18 (14/86)	33/67	1239	0
6	DMC18 (14/86)	50/50	1151	<1
7	DMC18 (0/100)	0/100	799	0

Experiments were performed using protocol for PO batch homopolymerizations. No CTA was utilized. Reaction conditions: $T = 70$ °C, $t = 4$ h, $V(\text{PO}) = 50$ mL, $m(\text{DMC}) = 25$ mg. ^a values in parentheses indicate ethanol/water ratio used for the preparation of the catalytic precursor, ^b ethanol/water ratio used for the work-up of the catalytic precursor, ^c in $[\text{g}_{\text{PPG}}/(\text{g}_{\text{Zn}} \cdot \text{h})]$, ^d determined from the temperature increase at the spontaneous onset of the exothermic polymerization.

The homopolymerization of PO was carried out in the presence of PPG ($M_n = 2$ kg/mol) as CTA. The DMC catalyst was charged to the autoclave and dried *in vacuo* at 100 °C. Subsequently, PO was added at a constant rate of 0.94 mL/min over a period of 18 h. The propoxylation was conducted in a starvation reaction mode, *i.e.* the instantaneous PO conversion X_{PO} was regularly at $98 \pm 2\%$ (Figure 5.69).

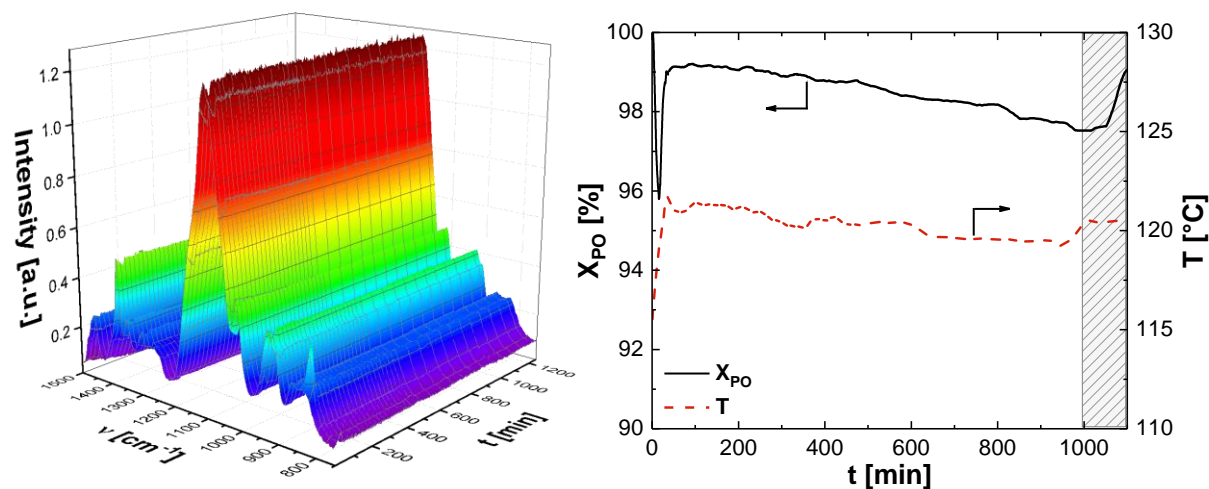


Figure 5.69 Left: *Online*-reaction monitoring of PO semi-batch homopolymerization using *in-situ* FTIR spectroscopy. Right: Instantaneous PO conversion X_{PO} and reaction temperature during the propoxylation reaction under continuous addition of PO. The initial drop in PO conversion is due to the build-up of the catalytic activity at early reaction stages. The instantaneous onset of the polymerization results in the increase in reaction temperature. The grey highlighted area marks the post-reaction where the monomer addition is finished, and residual PO is consumed.

SEC analysis of aliquots taken throughout the reaction allows to monitor the molecular weight development (Figure 5.70). The results show, that narrowly distributed polymers with $\text{PDI} \leq 1.2$ are obtained until a molecular weight of $M_n \approx 10$ kg/mol is reached. The molecular weight distributions show a shoulder at low molecular weights. The fact, that the shoulder is present from the early reaction stages and that its weight fraction is not changing regardless of the monomer conversion, indicate that it does not result from PO-isomerization and the

formation of unsaturated chain ends as typically observed for KOH catalysis¹⁶⁰. Instead, the appearance of the shoulder in the SEC may be attributed to further moieties that act as co-initiators. Such co-initiated poly(ether) polyols might be useful for certain applications, *e.g.* for foaming with non-chlorofluoro-carbons.²⁴²

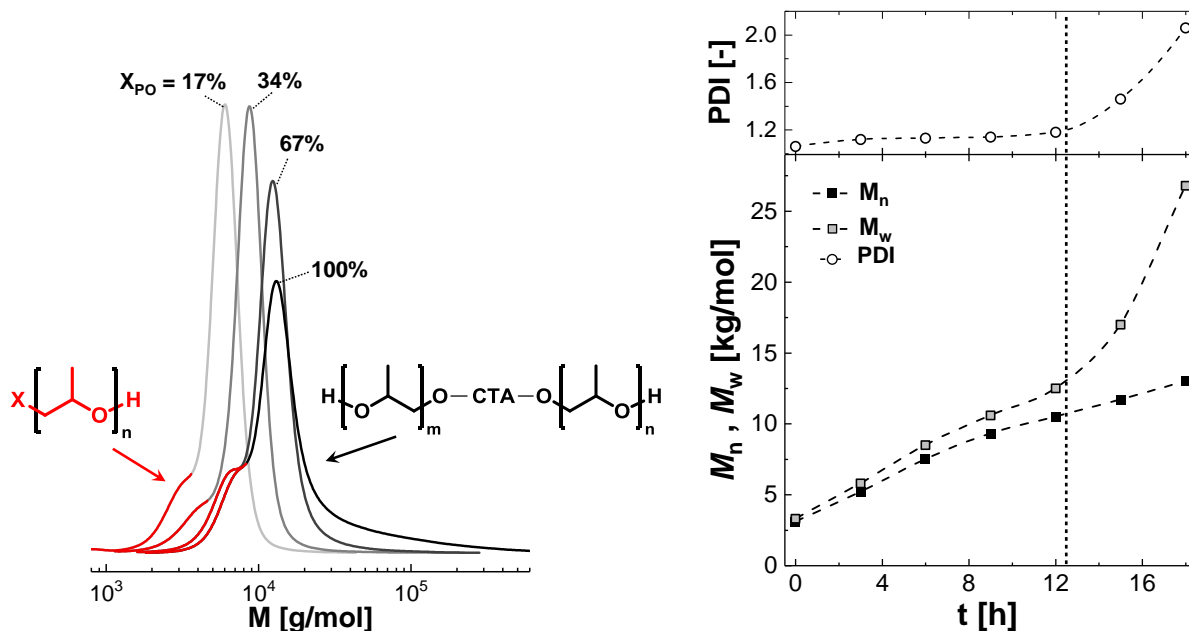


Figure 5.70 Left: Molecular weight distributions at different reaction stages. The values for X_{PO} displayed correlate to the total amount of PO that is fed during the entire reaction. Right: M_n , M_w and PDI as a function of the reaction time. PO was fed over 18 h at a constant rate (0.94 mL/min). The dashed line marks the onset of the broadening of the molecular weight distribution due to the formation of a high-molecular weight tail.

When continuing the addition of monomer at molecular weights of $M_n > 10$ kg/mol, a high molecular weight tail is formed (Figure 5.70). At early reaction stages, the ring-opening of PO appears to be rate-limiting, *i.e.* the chain transfer reaction is faster than the propoxylation reaction. Consequently, a narrow molecular weight distribution is observed. This observation is in agreement with kinetic experiments conducted by STAHL giving an apparent activation energy of $E_{a,app} \approx 79$ kJ/mol.²⁴³ $E_{a,app}$ was determined for the most active catalyst, DMC18 (14/86). The activation energy is in the range of a molecular reaction indicating that the ring-opening is indeed rate determining. At higher molecular weights however, the viscosity of the reaction medium increases as chains are starting to entangle. The diffusion of the growing chains becomes limited and thereby slower than the propoxylation reaction. In addition, the intermixing of the reaction medium, *i.e.* the dissolution of the fed PO, might be hampered leading to an increased formation of high-molecular weight species. The formation of the high-molecular weight tail thus appears to promote its own formation.

5.6.4 Copolymerization of PO and CO₂

The reaction of epoxides with CO₂ attracts increasing attention since the 1970s with regard to the on-going environmental pollution caused by humans. Indeed, recent products under the

trade name cardyon™ are commercially available after the pioneering work of PAC polymers (now empower materials with product name QPACs). Former products are copolymers of PO and CO₂ obtained under the action of DMC catalysts.²⁰ The selectivity of DMC catalysts towards CO₂-incorporation is usually limited giving access to poly(ether carbonates), rather than alternating poly(carbonates).

The amine-modified DMC catalysts were probed for the copolymerization of PO with CO₂. Interestingly, it was found, that the thermally activated amine-modified DMC catalysts show high CO₂ incorporation in comparison to the action of many reported DMCs. The CO₂ content of the obtained products with f_{carb} of about 88 mol% is a similar range as found for zinc dicarboxylates and represents one of the highest values reported for DMC-catalyzed PPC (Figure 5.71). The solvent composition during the preparation as well as the work-up of the catalytic precursor is significantly affecting the activity of the corresponding DMC catalyst (Table 5.24). It appears, that a certain amount of ethanol is required to sufficiently dissolve the alkyl amines during the catalytic precursor synthesis. In agreement with above mentioned results, thorough purification of the DMC-amine adducts is crucial to further improve the DMCs catalytic performance as traces of K⁺ are known to deactivate the catalyst.

Table 5.24 PO/CO₂ copolymerizations using DMC catalysts prepared from different EtOH/H₂O mixtures and purified using different solvent mixtures.

Entry	Catalyst ^b	EtOH/H ₂ O (v/v) work-up ^c	TOF ^d [h ⁻¹]	f_{carb} ^e [mol%]	f_{cPC} ^e [mol%]	M_n / M_w ^f [kg/mol]	PDI [-]
1	DMC18 (100/0)	0/100	279	75.0	6.1	n.d.	n.d.
2	DMC18 (50/50)	0/100	262	72.2	6.5	23/139	6.0
3	DMC18 (14/86)	0/100	772	83.9	8.0	40/97	2.4
4	DMC18 (14/86)	14/86	679	81.9	8.1	33/79	2.4
5	DMC18 (14/86)	33/67	486	80.4	6.8	27/68	2.5
7	DMC18 (0/100)	0/100	570	88.2	6.1	35/71	2.0
8	DMC18 (14/86) adduct ^a	0/100	100	51.2	5.7	3.6/29	8.1 ^g

Experiments were performed using the standard protocol for PO/CO₂ copolymerizations. Reaction conditions: $T = 60$ °C, $p = 30$ bar, $t = 4$ h, $V(\text{PO}) = 50$ mL, $m(\text{DMC}) = 50$ mg. ^a DMC-amine adduct prior to thermal activation, ^b values in parentheses indicate ethanol/water ratio used for the preparation of the catalytic precursor, ^c ethanol/water ratio used for the work-up of the catalytic precursor, ^d in $[\text{g}_{\text{PPC}}/(\text{g}_{\text{Zn}} \cdot \text{h})]$, ^e determined by ¹H-NMR from the crude product, ^f determined by SEC in THF against PS standards, ^g bimodal distribution.

The CO₂-selectivity increases with the length of the utilized parent amine with the ODA-modified DMC giving PPC with the highest f_{carb} . The parent-amine chain length effects the catalytic activity of the complexes (Table 5.25). The catalytic activity appears to correlate with the catalysts crystallinity and increases in the order DMC-C12 < DMC-C14 < DMC-C16 ≈ DMC-C18. While all catalysts are semicrystalline, it was observed higher crystallinities result in catalysts with higher activities. Consequently, increasing the amine chain length even further may be expected to yield more active catalysts. However, using C20 and longer amines is challenging as they become increasingly difficult to remove via distillation without decomposition and the formation of undesired side products. The impact of the crystallinity of the DMC complexes

on the catalytic activity was also observed for the action of DMCs in propoxylation reaction.^{231,233}

Table 5.25 PO/CO₂ copolymerization using DMC catalysts with different parent amines

Entry ^a	Parent-amine ^b	TOF ^c [h ⁻¹]	f_{carb} ^d [mol%]	f_{cPC} ^d [mol%]	M_n / M_w ^e [kg/mol]	PDI [-]
DMC12 (14/86)	C12	261	66.3	8.4	n.d.	n.d.
DMC14 (14/86)	C14	470	69.5	12.0	n.d.	n.d.
DMC16 (14/86)	C16	738	82.9	8.1	n.d.	n.d.
DMC18 (14/86)	C18	772	83.9	8.0	40/97	2.4

Experiments were performed using the standard protocol for PO/CO₂ copolymerizations. All catalyst precursors were purified using demineralized water only. Reaction conditions: $T = 60$ °C, $p = 30$ bar, $t = 4$ h, $V(\text{PO}) = 50$ mL, $m(\text{Cat}) = 50$ mg. ^a Values in parentheses indicate ethanol/water ratio used for the preparation of the catalytic precursor, ^b parent amine used for the synthesis of the catalytic precursor, ^c in $[\text{g}_{\text{PPC}}/(\text{g}_{\text{Zn}} \cdot \text{h})]$, ^d determined by ¹H-NMR from the crude product, ^e determined by SEC in THF against PS standards.

The PO/CO₂-copolymerization was also performed at varying CO₂-partial pressures (Table 5.22). The catalyst activity and the resulting product composition regarding carbonate vs ether linkages can be tailored by adjusting the reaction conditions. A similar behavior is observed for ZnGA (Chapter 5.1) and displays the importance of the feed.¹²⁷ This feature gives access to poly(carbonates) with tunable polymer composition and thus allows to tailor the resulting material properties as a function of f_{carb} .

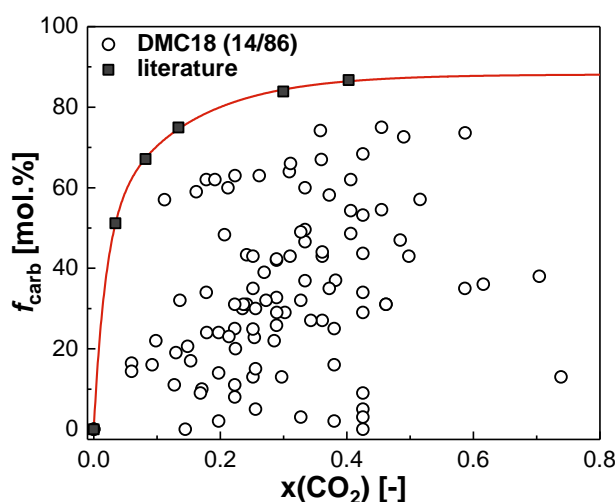


Figure 5.72 Copolymer composition f_{carb} for DMC18 (14/86) and other DMC catalysts reported in the literature^{54-58,143-147,166,218,220,226,234,244-246}. The composition of the feed $x(\text{CO}_2)$ was calculated from the solubility data of PO in CO₂ reported in literature.¹¹⁷

At early reaction stages, *i.e.* for low productivities, relatively broad molecular weight distributions are observed (PDI > 6.0; Table 5.24). However, the polydispersities of the final products are decreasing with higher conversions, approaching values of PDI = 2.

Table 5.26 PO/CO₂ copolymerization using DMC18 (14/86).

Entry	p [bar]	TOF ^a [h ⁻¹]	f_{carb} ^b [mol%]	f_{ePC} ^b [mol%]	M_n / M_w ^c [kg/mol]	PDI [-]
1	5	584	51.2	17.9	38/115	3.0
2	10	678	67.1	19.3	38/105	2.8
3	15	767	74.9	12.1	36/97	2.7
4	30	768	83.9	8.0	40/97	2.4
5	40	905	86.7	7.1	50/112	2.2

Experiments were performed using the standard protocol for PO/CO₂ copolymerizations. Reaction conditions: $T = 60$ °C, $t = 4$ h, $V(\text{PO}) = 50$ mL, $m(\text{Cat}) = 50$ mg. ^a in [g_{PPC}/(g_{Zn} · h)], ^b determined by ¹H-NMR spectroscopy, ^c determined by SEC in THF against PS standards.

The synthetic pathway of forming a DMC-amine adduct in a first step and subsequently activating the adduct by a reactive distillation procedure is a versatile tool for the preparation of heterogeneous catalysts for alkoxylation with PO. The preparation of amine-modified heterogeneous catalysts is considered a promising toolbox for the preparation of new classes of catalysts.

6 EXPERIMENTAL DETAILS

6.1 Materials

All moisture and air-sensitive materials were handled under inert atmosphere. The materials were used as received. 1,2-Epoxy-7-octene (97% purity, Sigma Aldrich), allyl glycidyl ether (>99% purity, Sigma Aldrich), epichlorohydrin (>99% purity, Sigma Aldrich), glycidol (96% purity, Sigma Aldrich), cyclohexene oxide (98% purity, Sigma Aldrich) and styrene oxide (97% purity, Sigma Aldrich) were distilled over CaH₂ prior to usage. Propylene oxide (99.9%, GHC Gerling, Holz & Co) and CO₂ (99.995%, Linde Gas) were used for the polymerizations as received. 2,2-bis(4-hydroxyphenyl) propane (BPA, 97%, Sigma Aldrich), 4,4'-sulfonyl diphenol (BPS, 99%, Abcr Chemicals), 2,2-bis(4-hydroxyphenyl) hexafluoro propane (BPAF, 99%, Abcr Chemicals), 4,4'-methylene bis(2,6-dimethylphenol) (MBDMP, 98%, Abcr Chemicals) were dried *in vacuo* prior to usage. 2-Phenoxyethanol (99%, Sigma Aldrich) was distilled and stored over molecular sieves (4 Å). ZnGA was synthesized as previously reported.¹²⁷ Alkoxylated BPA-derivates (HEBPA and HPBPA) and 4,4',4''-Trihydroxytriphenylmethane (THTPM) were synthesized according to the literature.²⁴⁷⁻²⁴⁹

6.2 Synthesis of amine-modified DMC catalysts

The synthesis of alkyl amine-modified Zn/Co-DMC catalysts was performed following an adapted literature procedure.²¹⁵ The synthesis of the DMC-amine-adducts was conducted in different ethanol/water-mixtures (Table 6.1).

Table 6.1 Reaction conditions for the synthesis of amine-modified DMC catalysts.

Catalyst	Parent amine	EtOH/H ₂ O (v/v) synthesis	EtOH/H ₂ O (v/v) work-up
DMC12 (14/86)	Dodecylamine (C12)	14/86	0/100
DMC14 (14/86)	Tetradecylamine (C14)	14/86	0/100
DMC16 (14/86)	Hexadecylamine (C16)	14/86	0/100
DMC18 (100/0)	Octadecylamine (C18)	100/0	0/100
DMC18 (50/50)	Octadecylamine (C18)	50/50	0/100
DMC18 (14/86)	Octadecylamine (C18)	14/86	14/86
	Octadecylamine (C18)	14/86	33/67
	Octadecylamine (C18)	14/86	50/50
	Octadecylamine (C18)	14/86	0/100
DMC18 (0/100)	Octadecylamine (C18)	0/100	0/100

In a 1-L-glass reactor equipped with a paravisc impeller, the corresponding alkyl amine (125 mmol) was slowly suspended in ethanol under vigorous stirring. After 30 min, distilled water was added dropwise over a period of 2 h. Subsequently, Zn(NO₃)₂ · 6 H₂O (16.8 g, 57 mmol) was added and the viscous suspension was stirred for 30 min. After the addition of

$K_3[Co(CN)_6]$ (11.9 g, 36 mmol), the reaction mixture was stirred for 20 h. The addition of the zinc and the cobalt salts are accompanied with a drastic increase in viscosity. Thorough stirring of the reaction mixture is crucial to obtain homogeneous products. The resulting suspension was centrifuged for 10 min at 10 °C (4000 rpm). The supernatant was discarded, and the residue washed with 1.5 L water and centrifuged three times. The residue was dried *in vacuo* to a constant weight to yield DMC-amine adduct (ca. **96 % yield**) as a white powder. The amine adduct was milled and the ODA was removed under reduced pressure (10^{-2} mbar) at 135 °C for 72 h to yield the active catalyst as an off-white to pale pink solid.

6.3 Synthesis of indium complexes

The ligands for complexes **1** – **4** and **7** (Chapter 5.5, Figure 5.57) as well as the corresponding indium halide complexes were prepared as previously reported.^{202,204,205,210,211,250–252}

Catalyst **2** was prepared according to the following procedure. A solution of *N,N'*-bis(3,5-di-*tert*-butylsalicylidene)-1,2-phenylene diamine (200 mg, 0.37 mmol) in toluene was added to a suspension of benzyl potassium (101 mg, 0.78 mmol) in toluene. The red suspension was stirred at room temperature overnight. The solvent was removed *in vacuo*. The residue was dissolved in THF and added to a suspension of $InCl_3$ (81.8 mg, 0.37 mmol) and stirred overnight. The reaction mixture was filtrated to remove solids and washed with cold hexane. The residue was dissolved in a minimal amount of toluene, filtered and dried *in vacuo* to yield complex **2** (Chapter 5.5, Figure 5.57) (149 mg, **59 %**) as an orange solid.

1H -NMR ($CDCl_3$, 25 °C, 400 MHz): δ [ppm] = 8.82 (s, 2H, $HC=N$), 7.76 – 7.69 (m, 2H, $C_{arom}-H$), 7.61 (d, $^4J_{HH} = 2.5$ Hz, 2H, $C_{arom}-H$), 7.48 – 7.42 (m, 2H, $C_{arom}-H$), 7.12 (d, 2H, $^4J_{HH} = 2.5$ Hz, $C_{arom}-H$), 1.55 (s, 18 H, $C(CH_3)_3$), 1.35 (s, 18 H, $C(CH_3)_3$)

6.4 Homopolymerization of PO

Batch polymerization

Polymerization experiments were carried out in 300 mL stainless steel autoclaves (Parr Instruments Company, Series 4560 Mini Reactors) equipped with 4-bladed propeller stirrers. The reactor was typically loaded with a 25 mg of DMC catalyst, sealed and evacuated to remove all volatiles. After pressurizing with 10 bars of argon, PO was added (50 mL, 0.71 mol) with an HPLC pump (Bischoff Chromatography, HPD Multitherm 200). Subsequently, the reactor was heated to 70 °C. Polymerization was terminated by cooling the reactor to room temperature, releasing the pressure and degassing to remove residual PO.

Semi-batch polymerization

A 2-L-stainless steel autoclave (Parr Instruments Company, Series 4520) was charged with the chain transfer agent and the DMC catalyst. The reactor was sealed, evacuated and heated up to 115 °C for 1 h. Subsequently, the autoclave was pressurized with 6 bar argon and 25 mL PO were added using a HPLC pump (0.83 mL/min). After several minutes, a rapid increase in temperature indicates the activation of the catalyst. After complete consumption of the initial

amount of monomer, the polymerization temperature was increased to 125 °C and the residual PO was added with the desired feeding rate. The monomer consumption was monitored using ReactIR™ 45 FTIR equipped with a flexible probe, having a diamond window. Spectra were recorded every 60 seconds in the range of $\nu = 650 - 2000 \text{ cm}^{-1}$ with a resolution of 4 cm^{-1} . After certain intervals aliquots were taken by means of a rising pipe. When the monomer addition was completed, the reaction mixture was stirred for 3 h at 125 °C to ensure the conversion of residual PO. The reactor was cooled to ambient temperature and depressurized. The crude PPG was dried *in vacuo* at 50 °C for 2 days.

Calibration of the ReactIR

The FTIR-probe was calibrated by dilution of the final product with monomer. A 2-L-stainless steel autoclave was charged with 250 g of PPG2000 and heated to 120 °C under vacuum for 1 h. Subsequently, the reactor was pressurized with 6 bar argon and five IR spectra were recorded. A defined amount of PO was added using a HPLC pump to simulate a decreased conversion. After 5 min of equilibration, again five IR spectra were recorded. The addition of PO and the sampling of the IR spectra were recorded until a theoretical conversion of 60 % was achieved (Table 6.2)

Table 6.2 Stepwise addition of PO to simulate decreasing conversions X_{PO} . $m(\text{PPG2000}) = 250 \text{ g}$.

V(PO) [mL]	X_{PO} [%]
0	100
6.2	98
12.6	96
19.3	94
26.3	92
33.6	90
53.3	85
75.5	80
100.7	75
129.4	70
162.6	60

6.5 Copolymerization of PO and CO₂

Standard protocol

Copolymerization experiments were carried out in 300 mL stainless steel autoclaves (Parr Instruments Company, Series 4560 Mini Reactors) equipped with 4-bladed propeller stirrers. The reactor was typically loaded with a defined amount of ZnGA or DMC catalyst (and a CTA), sealed and evacuated to remove all volatiles. After pressurizing with 10 bars of CO₂, PO was added (50 mL, 0.71 mol) with an HPLC pump (Bischoff Chromatography, HPD Multitherm 200). Subsequently, the reactor was heated to the desired temperature, and the pressure was adjusted to the target pressure. The pressure was kept constant with a feed of CO₂ gas, the

uptake was monitored by means of a mass flow controller. The copolymerization was terminated by cooling the reactor to room temperature, releasing the pressure and degassing to remove residual PO. The resulting crude product was dissolved in acetone and precipitated in water or methanol repeatedly, to remove cPC. Polymer samples were dried *in vacuo* at 50 °C to a constant weight.

Two stage copolymerization

Copolymerizations with two reaction stages were performed in a similar manner. After the first 4 h of reaction ($T = 60\text{ °C}$, $p = 30\text{ bar}$), the pressure was partially released and adjusted to the desired target pressure (2.5 to 10 bar). The reaction temperature was adjusted to 60 - 100 °C, respectively and kept at that level for 2 - 19 h. The copolymerization was terminated by cooling to room temperature, releasing the pressure and degassing to remove surplus PO. The resulting crude product was dissolved in acetone and precipitated repeatedly in methanol to remove the cyclic carbonate. The purified samples were dried in a dynamic vacuum to constant weight.

Online-monitoring

Experiments with *in-situ* FTIR-monitoring were performed in a 2 L stainless steel autoclave (Parr Instruments Company, Series 4520) equipped with an anchor agitator. The reactor was loaded with catalyst and the specific amount of CTA, evacuated and heated to the desired temperature. Subsequently, the reactor was pressurized with 30 bars of CO₂ and PO was added by means of an HPLC pump (Bischoff Chromatography, HPD Multitherm 200). The reaction progress was monitored using a ReactIR™ 45 FTIR equipped with a flexible probe having a diamond window. Spectra were recorded every 60 seconds in the range of $\nu = 650 - 2000\text{ cm}^{-1}$ with a resolution of 4 cm^{-1} .

6.6 Cycloaddition of epoxides and CO₂

The reactions were carried out in 25 mL and 75 mL stainless steel autoclaves (Parr Instrument Company) equipped with 4-bladed propeller stirrers. In a typical experiment, the reactor vessel was loaded with the catalyst, co-catalyst and the epoxide as well as toluene as solvent inside of a glove box. The reaction mixture was purged with CO₂ for 30 seconds and then pressurized with 15 bar of CO₂. The mixture was swiftly heated to the desired temperature, after which the pressure was adjusted to the target pressure. The experiments were terminated by cooling to room temperature, releasing the pressure and removing any volatiles. The crude product was analyzed by means of ¹H-NMR and FTIR spectroscopy. The products were dissolved in methanol and syringe-filtered. The final products were obtained by removing all volatiles in a dynamic vacuum.

6.7 Material characterization

¹H-NMR

Product distribution and polymer composition were determined from ¹H NMR spectra. The spectra were recorded on a Bruker Avance Ultrashield-400 spectrometer in CDCl₃ at room temperature using tetramethylsilane as a reference.

¹³C-NMR

The regioregularity of the polymers was determined from ¹³C-IGATED-NMR spectra (2 000 scans).

FTIR spectroscopy

FTIR spectra were collected on a Thermo Scientific Nicolet iS10 FT-IR spectrometer in a range from 400-4000 cm⁻¹ and a resolution of 0.5 cm⁻¹.

DSC

DSC measurements were conducted on a Mettler-Toledo DSC 1. Polymer samples were subjected to a temperature cycles from -80 °C to 120 °C under N₂ atmosphere (heating rate = 10 K/min). The glass transition temperature was determined from the second heating cycle. Catalyst samples were analyzed from -80 °C to 180 °C

SEM

Powder samples were coated with carbon and inspected with a LEO Gemini 1525 Scanning Electron Microscope operated at 5.0 kV.

XRD

Powder XRD measurements were conducted on a STOE Stadi P Diffractometer in a range of 2 – 90 ° using Cu K_α irradiation ($\lambda = 1.54 \text{ \AA}$).

Elemental Analysis

Carbon, Hydrogen, and Nitrogen contents were measured on a Euro EA elemental analyzer. Oxygen content was measured on a HEKAtech HT Oxygen Analyzer. The Combustions Gases were quantified by GC with a thermal conductivity detector

Thermal stability

For the investigation of the thermal depolymerization, the purified polymer was heated at 180 °C for 1 h under Ar atmosphere. The backbiting reaction was monitored using ¹H NMR spectroscopy.

SEC

Molecular weight distributions were obtained using SEC (Flom Intelligent pump AI12, Schambek SFD RI2012 detector and HP 1050 series UV/Vis detector ($\lambda = 256 \text{ nm}$), using a MZ-gel SDplus linear column (5 μm , 300 × 8 mm) with tetrahydrofuran as eluent. The values given are relative to monodisperse PS standards (Agilent).

Rheometry

Rheological experiments were performed on a DHR-2 combined motor-transducer rheometer (TA Instruments, New Castle, USA) using a plate-plate geometry (diameter = 8 mm, measuring gap = 1000 μm). Frequency sweeps were performed at $T = 30 - 150$ °C and angular frequencies of $\omega = 0.1 - 100$ rad/s. Experiments were performed within the linear viscoelastic regime, which was established in an amplitude sweep experiment. The dynamic viscosity as determined in shear experiments of the copolymers with molecular masses well-over entanglement molecular masses shows shear induced thinning. The frequency dependence of the viscosity was described using the CARREAU-YASUDA equation

$$\eta(\omega) = \eta_{\infty} + (\eta_0 - \eta_{\infty})[1 + (\lambda_0 \omega)^b]^{n/b} \quad (6.1)$$

with the infinite shear viscosity η_{∞} , the longest relaxation time λ_0 and the slope in the power law region n .²⁵³ The fit parameter b accounts for the transition between NEWTONian viscosity and the power law region. Prior to the experiments the thermal stability of the samples was verified by time sweeps at $T = 150$ °C and $\omega = 1$ rad/s for 30 min. Specimen for rheometry measurements were prepared by solution casting from acetone solutions of the polymers. The resulting films were conditioned at 50 °C *in vacuo* prior to the measurements and were essentially free from cPC and solvents.

LAOS measurements were conducted at temperatures of $T = 140$ °C and angular frequencies in the range of $\omega = 0.1 - 10$ rad/s. The experiments were performed using a plate-plate geometry (diameter = 25 mm, measuring gap = 1000 μm). The active deformation control (continuous oscillation mode) of the DHR-2 was used. The motor mode was set to stiff. The raw data was processed using the MITlaos software developed by EWOLDT, WINTER, and MCKINLEY.¹⁸⁷ For the determination of CHEBYSHEV and FOURIER coefficients, between two and three strain cycles were used with two previously applied conditioning cycles. The highest significant harmonic of the raw data was determined by discrete FT analysis and used to reconstruct a noise-reduced stress signal, which was used in the consecutive analysis.

Pycnometry

The density of polymer samples was measured using a pycnometer with a metered volume and water as filling medium. The density, *i.e.* more precisely the volume, of the samples was calculated from the liquid displacement upon addition of the samples. Demineralized water was used as a liquid medium ($T = 20$ °C, $\rho = 0.998$ g/cm³).

7 BIBLIOGRAPHY

- 1 www.plasticseurope.org, date accessed 01.02.2019.
- 2 E. Alper and O. Yuksel Orhan, *Petroleum*, 2017, **3**, 109–126.
- 3 J. Wilcox, *Carbon Capture*, Springer, 2012.
- 4 A. W. Kleij, M. North and A. Urakawa, *ChemSusChem*, 2017, **10**, 1036–1038.
- 5 T. Sakakura, J.-C. Choi and H. Yasuda, *Chem. Rev.*, 2007, **107**, 2365–2387.
- 6 M. Cokoja, C. Bruckmeier, B. Rieger, W. a. Herrmann and F. E. Kühn, *Angew. Chemie Int. Ed.*, 2011, **50**, 8510–8537.
- 7 M. Eriksen, L. C. M. Lebreton, H. S. Carson, M. Thiel, C. J. Moore, J. C. Borerro, F. Galgani, P. G. Ryan and J. Reisser, *PLoS One*, 2014, **9**, e111913.
- 8 H. Webb, J. Arnott, R. Crawford and E. Ivanova, *Polymers*, 2012, **5**, 1–18.
- 9 H. Hirai, H. Takada, Y. Ogata, R. Yamashita, K. Mizukawa, M. Saha, C. Kwan, C. Moore, H. Gray, D. Laursen, E. R. Zettler, J. W. Farrington, C. M. Reddy, E. E. Peacock and M. W. Ward, *Mar. Pollut. Bull.*, 2011, **62**, 1683–1692.
- 10 T. Artham and M. Doble, *Macromol. Biosci.*, 2008, **8**, 14–24.
- 11 Z. Yu, L. Xu, Y. Wei, Y. Wang, Y. He, Q. Xia, X. Zhang and Z. Liu, *Chem. Commun.*, 2009, 3934–3936.
- 12 www.arm-alysis.de, date accessed 31.01.2017.
- 13 G. A. Luinstra, *Polym. Rev.*, 2008, **48**, 192–219.
- 14 G. A. Luinstra and F. Molnar, *Macromol. Symp.*, 2007, **259**, 203–209.
- 15 Y. Qin and X. Wang, *Biotechnol. J.*, 2010, **5**, 1164–1180.
- 16 T. Dong, X. Yun, M. Li, W. Sun, Y. Duan and Y. Jin, *J. Appl. Polym. Sci.*, 2015, **132**, 41871.
- 17 F. Gao, Q. Zhou, Y. Dong, Y. Qin, X. Wang, Z. Xiaojiang and W. Fosong, *J. Polym. Res.*, 2012, **19**, 1–5.
- 18 www.empowermaterials.com, date accessed 15.03.2018.
- 19 www.novomer.com, date accessed 16.12.2016.
- 20 www.covestro.de, date accessed 18.09.2018.
- 21 J. Langanke, A. Wolf, J. Hofmann, K. Böhm, M. A. Subhani, T. E. Müller, W. Leitner and C. Gürtler, *Green Chem.*, 2014, **16**, 1865–1870.
- 22 J. Deng, Y. Wang, L. Zhou, M. Gou, N. Luo, H. Chen, A. Tong, C. You and G. Guo, *RSC Adv.*, 2015, **5**, 42943–42954.

- 23 G.-W. Chang, C.-L. Tseng, Y.-S. Tzeng, T.-M. Chen and H.-W. Fang, *J. Taiwan Inst. Chem. Eng.*, 2017, **80**, 813–819.
- 24 H. Li and Y. Niu, *Int. J. Polym. Mater. Polym. Biomater.*, 2018, **67**, 192–198.
- 25 A. Singh, in *Encyclopedia of Polymeric Nanomaterials*, eds. S. Kobayashi and K. Müllen, Springer, Berlin, 2014, pp. 1–5.
- 26 J. Feng, R. X. Zhuo and X. Z. Zhang, *Prog. Polym. Sci.*, 2012, **37**, 211–236.
- 27 S. Bian, C. Pagan, A. A. Andrianova and G. Du, *ACS Omega*, 2016, **1**, 1049–1057.
- 28 M. Tamura, K. Ito, M. Honda, Y. Nakagawa, H. Sugimoto and K. Tomishige, *Sci. Rep.*, 2016, **6**, 24038.
- 29 D. J. Darensbourg, A. I. Moncada, W. Choi and J. H. Reibenspies, *J. Am. Chem. Soc.*, 2008, **130**, 6523–6533.
- 30 D. J. Darensbourg, A. I. Moncada and S.-H. Wei, *Macromolecules*, 2011, **44**, 2568–2576.
- 31 G. W. Coates and D. R. Moore, *Angew. Chemie Int. Ed.*, 2004, **43**, 6618–6639.
- 32 D. J. Darensbourg, *Chem. Rev.*, 2007, **107**, 2388–2410.
- 33 D. J. Darensbourg and A. D. Yeung, *Polym. Chem.*, 2015, **6**, 1103–1117.
- 34 S. Inoue, H. Koinuma and T. Tsuruta, *Die Makromol. Chemie*, 1969, **130**, 210–220.
- 35 G. A. Luinstra, G. R. Haas, F. Molnar, V. Bernhart, R. Eberhardt and B. Rieger, *Chem. - A Eur. J.*, 2005, **11**, 6298–6314.
- 36 S. E. Schaus, B. D. Brandes, J. F. Larrow, M. Tokunaga, K. B. Hansen, A. E. Gould, M. E. Furrow and E. N. Jacobsen, *J. Am. Chem. Soc.*, 2002, **124**, 1307–1315.
- 37 L. P. C. Nielsen, C. P. Stevenson, D. G. Blackmond and E. N. Jacobsen, *J. Am. Chem. Soc.*, 2004, **126**, 1360–1362.
- 38 T. Aide and S. Inoue, *Acc. Chem. Res.*, 1996, **29**, 39–48.
- 39 D. R. Moore, M. Cheng, E. B. Lobkovsky and G. W. Coates, *J. Am. Chem. Soc.*, 2003, **125**, 11911–11924.
- 40 M. Cheng, D. R. Moore, J. J. Reczek, B. M. Chamberlain, E. B. Lobkovsky and G. W. Coates, *J. Am. Chem. Soc.*, 2001, **123**, 8738–8749.
- 41 N. York, J. Bastide, J. Hamelin, D. R. Moore, M. Cheng, E. B. Lobkovsky and G. W. Coates, *Angew. Chemie Int. Ed.*, 2005, **4**, 2599–2602.
- 42 W. C. Ellis, Y. Jung, M. Mulzer, R. Di Girolamo, E. B. Lobkovsky and G. W. Coates, *Chem. Sci.*, 2014, **5**, 4004.
- 43 B. Y. Lee, H. Y. Kwon, S. Y. Lee, S. J. Na, S.-I. Han, H. Yun, H. Lee and Y.-W. Park, *J. Am. Chem. Soc.*, 2005, **127**, 3031–3037.

- 44 T. Bok, H. Yun and B. Y. Lee, *Inorg. Chem.*, 2006, **45**, 4228–4237.
- 45 M. R. Kember, P. D. Knight, P. T. R. Reung and C. K. Williams, *Angew. Chemie Int. Ed.*, 2009, **48**, 931–933.
- 46 M. R. Kember, A. J. P. White and C. K. Williams, *Inorg. Chem.*, 2009, **48**, 9535–9542.
- 47 M. W. Lehenmeier, S. Kissling, P. T. Altenbuchner, C. Bruckmeier, P. Deglmann, A.-K. Brym and B. Rieger, *Angew. Chemie Int. Ed.*, 2013, **52**, 9821–6.
- 48 S. Kissling, M. W. Lehenmeier, P. T. Altenbuchner, A. Kronast, M. Reiter, P. Deglmann, U. B. Seemann and B. Rieger, *Chem. Commun.*, 2015, **51**, 4579–4582.
- 49 K. Nakano, T. Kamada and K. Nozaki, *Angew. Chemie Int. Ed.*, 2006, **45**, 7274–7277.
- 50 E. K. Noh, S. J. Na, S. Sujith, S.-W. Kim and B. Y. Lee, *J. Am. Chem. Soc.*, 2007, **129**, 8082–8083.
- 51 S. S, J. K. Min, J. E. Seong, S. J. Na and B. Y. Lee, *Angew. Chemie Int. Ed.*, 2008, **47**, 7306–7309.
- 52 S. J. Na, S. S, A. Cyriac, B. E. Kim, J. Yoo, Y. K. Kang, S. J. Han, C. Lee and B. Y. Lee, *Inorg. Chem.*, 2009, **48**, 10455–10465.
- 53 W. Kruper, D. Swart, *Carbon Dioxide Oxirane Copolymers Prepared Using Double Metal Cyanide Complexes*, US 4,500,704, 1985.
- 54 Z. Li, Y. Qin, X. Zhao, F. Wang, S. Zhang and X. Wang, *Eur. Polym. J.*, 2011, **47**, 2152–2157.
- 55 X.-H. Zhang, R.-J. Wei, X.-K. Sun, J.-F. Zhang, B.-Y. Du, Z.-Q. Fan and G.-R. Qi, *Polymer (Guildf.)*, 2011, **52**, 5494–5502.
- 56 Y. Gao, L. Gu, Y. Qin, X. Wang and F. Wang, *J. Polym. Sci. Part A Polym. Chem.*, 2012, **50**, 5177–5184.
- 57 M. A. Subhani, C. Gürtler, W. Leitner and T. E. Müller, *Eur. J. Inorg. Chem.*, 2016, **2016**, 1944–1949.
- 58 X. H. Zhang, S. Chen, X. M. Wu, X. K. Sun, F. Liu and G. R. Qi, *Chinese Chem. Lett.*, 2007, **18**, 887–890.
- 59 S. Klaus, M. W. Lehenmeier, E. Herdtweck, P. Deglmann, A. K. Ott and B. Rieger, *J. Am. Chem. Soc.*, 2011, **133**, 13151–13161.
- 60 M. Ree, J. Y. Bae, J. H. Jung and T. J. Shin, *J. Polym. Sci. Part A Polym. Chem.*, 1999, **37**, 1863–1876.
- 61 M. Ree, Y. Hwang, J.-S. Kim, H. Kim, G. Kim and H. Kim, *Catal. Today*, 2006, **115**, 134–145.
- 62 R. Korashvili, Dissertation, *Heterogen katalysierte Copolymerisation von Kohlenstoffdioxid und Propylenoxid*, Universität Hamburg, 2012.

- 63 A. Rahlf, Diploma thesis, *Kinetik der zinkglutarat-katalysierten Copolymerisation von Kohlenstoffdioxid und Propylenoxid*, Universität Hamburg, 2013.
- 64 Y. Z. Meng, L. C. Du, S. C. Tiong, Q. Zhu and A. S. Hay, *J. Polym. Sci. Part A Polym. Chem.*, 2002, **40**, 3579–3591.
- 65 J.-S. Kim, H. Kim, J. Yoon, K. Heo and M. Ree, *J. Polym. Sci. Part A Polym. Chem.*, 2005, **43**, 4079–4088.
- 66 A. Brym, J. Zubiller, G. Luinstra, R. Korashvili, *Verfahren zur Herstellung von Zinkdicarboxylat*, WO 2013/034489, 2013.
- 67 B. Nörnberg, Dissertation, *Aliphatic Polycarbonates from Epoxides and Carbon Dioxide: Synthesis, Properties and Their Application*, University of Hamburg, 2015.
- 68 J. Kim, H. Kim and M. Ree, *Chem. Mater.*, 2004, **16**, 2981–2983.
- 69 M. Scharfenberg, J. Hilf and H. Frey, *Adv. Funct. Mater.*, 2018, **28**, 1704302.
- 70 X.-H. Zhang, R.-J. Wei, Y. Zhang, B.-Y. Du and Z.-Q. Fan, *Macromolecules*, 2015, **48**, 536–544.
- 71 N. Kindermann, À. Cristòfol and A. W. Kleij, *ACS Catal.*, 2017, **7**, 3860–3863.
- 72 Y. Liu, W.-M. Ren, W.-P. Zhang, R.-R. Zhao and X.-B. Lu, *Nat. Commun.*, 2015, **6**, 8594.
- 73 O. Hauenstein, M. Reiter, S. Agarwal, B. Rieger and A. Greiner, *Green Chem.*, 2016, **18**, 760–770.
- 74 Y. Liu, W.-M. Ren, M. Wang, C. Liu and X.-B. Lu, *Angew. Chemie Int. Ed.*, 2015, **54**, 2241–2244.
- 75 D. J. Darensbourg and S. J. Wilson, *Macromolecules*, 2013, **46**, 5929–5934.
- 76 R. Arai, K. Seto, A. Bell and H. Sugimoto, *Polym. J.*, 2018.
- 77 G. A. Luinstra and E. Borchardt, *Adv. Polym. Sci.*, 2012, **245**, 29–48.
- 78 S. Peng, Y. An, C. Chen, B. Fei, Y. Zhuang and L. Dong, *Polym. Degrad. Stab.*, 2003, **80**, 141–147.
- 79 C. Barreto, E. Hansen and S. Fredriksen, *Polym. Degrad. Stab.*, 2012, **97**, 893–904.
- 80 J. K. Varghese, S. J. Na, J. H. Park, D. Woo, I. Yang and B. Y. Lee, *Polym. Degrad. Stab.*, 2010, **95**, 1039–1044.
- 81 J. An, Y. Ke, X. Cao, Y. Ma and F. Wang, *Polym. Chem.*, 2014, **5**, 4245–4250.
- 82 M. F. Lai, J. Li and J. J. Liu, *J. Therm. Anal. Calorim.*, 2005, **82**, 293–298.
- 83 L. Zhu, X. Wang, L. Wu, Y. Luo, Y. Zhu, Q. Lin and Z. Shi, *Mater. Lett.*, 2014, **128**, 396–399.
- 84 B. Bahramian, Y. Ma, R. Rohanizadeh, W. Chrzanowski and F. Dehghani, *Green Chem.*,

- 2016, **18**, 3740–3748.
- 85 Y. Tao, X. Wang, X. Zhao, J. Li and F. Wang, *Polymer (Guildf.)*, 2006, **47**, 7368–7373.
- 86 L. Shi, X. Lu, R. Zhang, X.-J. Peng, C. Zhang, J. Li and X. Peng, *Macromolecules*, 2006, **39**, 5679–5685.
- 87 L. J. Gao, M. Xiao, S. J. Wang and Y. Z. Meng, *J. Appl. Polym. Sci.*, 2008, **108**, 1037–1043.
- 88 J. E. Seong, S. J. Na, A. Cyriac, B. W. Kim and B. Y. Lee, *Macromolecules*, 2010, **43**, 903–908.
- 89 A. Okada, S. Kikuchi and T. Yamada, *Chem. Lett.*, 2011, **40**, 209–211.
- 90 G. P. Wu, P. X. Xu, Y. P. Zu, W. M. Ren and X. B. Lu, *J. Polym. Sci. Part A Polym. Chem.*, 2013, **51**, 874–879.
- 91 L. Gu, Y. Qin, Y. Gao, X. Wang and F. Wang, *J. Polym. Sci. Part A Polym. Chem.*, 2013, **51**, 2834–2840.
- 92 L. Gu, Y. Qin, Y. Gao, X. Wang and F. Wang, *Chinese J. Chem.*, 2012, **30**, 2121–2125.
- 93 Z. N. Nysenko, E. E. Said-Galiev, M. I. Buzin, Y. E. Belevtsev, M. M. Il'in, G. G. Nikiforova and A. M. Sakharov, *Mendeleev Commun.*, 2014, **24**, 236–238.
- 94 L. Tang, W. Luo, M. Xiao, S. Wang and Y. Meng, *J. Polym. Sci. Part A Polym. Chem.*, 2015, **53**, 1734–1741.
- 95 P. F. Song, M. Xiao, F. G. Du, S. J. Wang, L. Q. Gan, G. Q. Liu and Y. Z. Meng, *J. Appl. Polym. Sci.*, 2008, **109**, 4121–4129.
- 96 P. Song, S. Wang, M. Xiao, F. Du, L. Gan, G. Liu and Y. Meng, *J. Polym. Res.*, 2009, **16**, 91–97.
- 97 Z. Duan, X. Wang, Q. Gao, L. Zhang, B. Liu and I. Kim, *J. Polym. Sci. Part A Polym. Chem.*, 2014, **52**, 789–795.
- 98 Y. Liu, M. Xiao, S. Wang, L. Xia, D. Hang, G. Cui and Y. Meng, *RSC Adv.*, 2014, **4**, 9503–9508.
- 99 P. Song, X. Mao, X. Zhang, X. Zhu and R. Wang, *RSC Adv.*, 2014, **4**, 15602–15605.
- 100 W.-M. Kulicke, in *Broschüre zur Dozententagung*, University of Hamburg, 2006.
- 101 A. C. Pipkin, in *Applied mathematical sciences*, Applied mathematical sciences, New York, 1972.
- 102 K. Hyun, M. Wilhelm, C. O. Klein, K. S. Cho, J. G. Nam, K. H. Ahn, S. J. Lee, R. H. Ewoldt and G. H. McKinley, *Prog. Polym. Sci.*, 2011, **36**, 1697–1753.
- 103 K. Hyun, S. H. Kim, K. H. Ahn and S. J. Lee, *J. Nonnewton. Fluid Mech.*, 2002, **107**, 51–65.
- 104 K. S. Cho, K. Hyun, K. H. Ahn and S. J. Lee, *J. Rheol.*, 2005, **49**, 747–758.

- 105 R. H. Ewoldt, A. E. Hosoi and G. H. McKinley, *J. Rheol.*, 2008, **52**, 1427–1458.
- 106 M. Wilhelm, *Macromol. Mater. Eng.*, 2002, **287**, 83–105.
- 107 K. Hyun and M. Wilhelm, *Macromolecules*, 2009, **42**, 411–422.
- 108 D. Weipert, H. D. Tscheuschner and E. Windhab, *Rheologie der Lebensmittel*, 1993.
- 109 R. Korashvili, B. Nörnberg, N. Bornholdt, E. Borchardt and G. A. Luinstra, *Chemie Ing. Tech.*, 2013, **85**, 437–446.
- 110 C. Tan and T. Hsu, *Macromolecules*, 1997, **30**, 3147–3150.
- 111 K. Soga, K. Hyakkoku, K. Izumi and S. Ikeda, *J. Polym. Sci. Polym. Chem. Ed.*, 1978, **16**, 2383–2392.
- 112 A. M. Sakharov, V. V. Il'in, V. V. Rusak, Z. N. Nysenko and S. A. Klimov, *Russ. Chem. Bull.*, 2002, **51**, 1451–1454.
- 113 D. J. Darensbourg, N. W. Stafford and T. Katsurao, *J. Mol. Catal. A Chem.*, 1995, **104**, L1–L4.
- 114 T. V. Rakhimov, E. E. Said-Galiev, V. V. Il'in, Z. N. Nysenko and A. M. Sakharov, *Russ. Khimicheskii Zhurnal*, 2004, **48**, 124–128.
- 115 T. V. Rakhimov, E. E. Said-Galiev, R. A. Vinokur, L. N. Nikitin, A. R. Khokhlov, V. V. Il'in, Z. N. Nysenko, A. M. Sakharov and K. Schaumburg, *Polym. Sci. Ser. B*, 2004, **46**, 61–65.
- 116 D. Jintang, W. Jiajun, F. Lianfang, W. Long and G. Xueping, *J. Appl. Polym. Sci.*, 2010, **118**, 366–371.
- 117 J.-J. Wang, J.-T. Duan, L. Wang, X.-P. Gu and L.-F. Feng, *J. Chem. Eng. Data*, 2010, **55**, 3379–3382.
- 118 B. Nörnberg, C. Spottog, A. Rahlf, R. Korashvili, C. Berlin and G. A. Luinstra, *Macromol. Symp.*, 2013, **333**, 190–196.
- 119 D.-Y. Peng and D. B. Robinson, *Ind. Eng. Chem. Fundam.*, 1976, **15**, 59–64.
- 120 T. R. Bott and H. N. Sadler, *J. Chem. Eng. Data*, 1966, **11**, 25–25.
- 121 L. Base, R. L. Paddock and S. T. Nguyen, *Macromolecules*, 2005, **38**, 6251–6253.
- 122 T. Aida, M. Ishikawa and S. Inoue, *Macromolecules*, 1986, **19**, 8–13.
- 123 C. T. Cohen, C. T. Cohen, T. Chu, T. Chu, G. W. Coates and G. W. Coates, *J. Am. Chem. Soc.*, 2005, **127**, 10869–78.
- 124 X. B. Lu, L. Shi, Y. M. Wang, R. Zhang, Y. J. Zhang, X. J. Peng, Z. C. Zhang and B. Li, *J. Am. Chem. Soc.*, 2006, **128**, 1664–1674.
- 125 S. Lin, W. Yu, X. Wang and C. Zhou, *Ind. Eng. Chem. Res.*, 2014, **53**, 18411–18419.

- 126 C. T. Cohen and G. W. Coates, in *Journal of Polymer Science, Part A: Polymer Chemistry*, 2006, vol. 44, pp. 5182–5191.
- 127 J. Marbach, B. Nörnberg, A. F. Rahlf and G. A. Luinstra, *Catal. Sci. Technol.*, 2017, **7**, 2897–2905.
- 128 S. Motika, T. Pickering, A. Rockicki, *Catalyst for the Copolymerization of Epoxides with CO₂*, US 5,026,676, 1991.
- 129 R. Eberhardt, M. Allmendinger and B. Rieger, *Macromol. Rapid Commun.*, 2003, **24**, 194–196.
- 130 D. J. Darensbourg, R. M. Mackiewicz and D. R. Billodeaux, *Organometallics*, 2005, **24**, 144–148.
- 131 J. Hofmann, U. Rauwald, M. Wohak, N. Nefzger, N. Welsch, A. Wolf, M. Traving, L. Krüger, *Verfahren zur Herstellung von Polyethercarbonatpolyolen*, EP3260483 A1, 2016.
- 132 L. Ma, L. Song, F. Li, H. Wang and B. Liu, *Colloid Polym. Sci.*, 2017, **295**, 2299–2307.
- 133 M. Scharfenberg, S. Wald, F. R. Wurm and H. Frey, *Polymers*, 2017, **9**, 422.
- 134 T. Müller, C. Gürtler, M. Wohak, J. Hofmann, M. Subhani, W. Leitner, I. Peckermann, A. Wolf, *Polyether carbonate polyol production method*, WO2014/033070A1, 2014.
- 135 J. Courtois, M. Schneelee, W. Riegel, A. Brym, H. Görtz, *Verfahren zur Herstellung von niedermolekularem Polyalkylencarbonat*, EP 2 557 104, 2012.
- 136 W. Luo, J. Qin, M. Xiao, D. Han, S. Wang and Y. Meng, *ACS Omega*, 2017, **2**, 3205–3213.
- 137 S. Inoue, *J. Polym. Sci. Part A Polym. Chem.*, 2000, **38**, 2861–2871.
- 138 S. Asano, T. Aida and S. Inoue, *J. Chem. Soc., Chem. Commun.*, 1985, 1148–1149.
- 139 K. Soga, K. Hyakkoku and S. Ikeda, *Die Makromol. Chemie*, 1978, **179**, 2837–2843.
- 140 S. Allen, G. Coates, A. Cherian, C. Simoneau, A. Gridnev, J. Farmer, *Polycarbonat polyol compositions and methods*, WO 2010/028362, 2010.
- 141 A. Cyriac, S. H. Lee, J. K. Varghese, E. S. Park, J. H. Park and B. Y. Lee, *Macromolecules*, 2010, **43**, 7398–7401.
- 142 S. H. Lee, A. Cyriac, J. Y. Jeon and B. Y. Lee, *Polym. Chem.*, 2012, **3**, 1215.
- 143 Y. Gao, Y. Qin, X. Zhao, F. Wang and X. Wang, *J. Polym. Res.*, 2012, **19**, 9878.
- 144 J. K. Varghese, D. S. Park, J. Y. Jeon and B. Y. Lee, *J. Polym. Sci. Part A Polym. Chem.*, 2013, **51**, 4811–4818.
- 145 S. Liu, Y. Qin, X. Chen, X. Wang and F. Wang, *Polym. Chem.*, 2014, **5**, 6171–6179.
- 146 S. Liu, Y. Miao, L. Qiao, Y. Qin, X. Wang, X. Chen and F. Wang, *Polym. Chem.*, 2015, **6**, 7580–7585.

- 147 K. Ma, Q. Bai, L. Zhang and B. Liu, *RSC Adv.*, 2016, **6**, 48405–48410.
- 148 S. Liu, Y. Qin, H. Guo, X. Wang and F. Wang, *Sci. China Chem.*, 2016, **59**, 1369–1375.
- 149 S. Liu, Y. Qin, L. Qiao, Y. Miao, X. Wang and F. Wang, *Polym. Chem.*, 2016, **7**, 146–152.
- 150 A. Rokicki, *Making Poly(alkylene carbonates) of controlled molecular weight*, US 4943677, 1990.
- 151 X. Yun, X. Zhang, Y. Jin, J. Yang, G. Zhang and T. Dong, *J. Macromol. Sci. Part B*, 2015, **54**, 275–285.
- 152 M. H. Chisholm, D. Navarro-Llobet and Z. Zhou, *Macromolecules*, 2002, **35**, 6494–6504.
- 153 J. Kim, M. Ree, S. Lee, W. Oh, S. Baek, B. Lee, T. Shin, K. Kim, B. Kim and J. Lünig, *J. Catal.*, 2003, **218**, 386–395.
- 154 D. Hölting, Dissertation, *Kohlenstoffdioxid sowie 2,3-Butylenoxid-Derivate als Polymerbausteine - Synthese und Charakterisierung von Polyolen und ungesättigten Polyestern als Komponente für die Herstellung von Polyurethane und UP-Harze*, University of Hamburg, 2012.
- 155 E. Borchardt, Dissertation, *Zur Rheologie und Lichtstreuung von Poly(propylencarbonat)*, Universität Hamburg, 2014.
- 156 D. J. Darensbourg and S.-H. Wei, *Macromolecules*, 2012, **45**, 5916–5922.
- 157 X. Sheng, W. Wu, Y. Qin, X. Wang and F. Wang, *Polym. Chem.*, 2015, **6**, 4719–4724.
- 158 L. Wu, A. Yu, M. Zhang, B. Liu and L. Chen, *J. Appl. Polym. Sci.*, 2004, **92**, 1302–1309.
- 159 S. H. Lee, I. K. Lee, J. Y. Ha, J. K. Jo, I. Park, C.-S. Ha, H. Suh and I. Kim, *Ind. Eng. Chem. Res.*, 2010, **49**, 4107–4116.
- 160 M. Ionescu, *Chemistry and Technology of Polyols for Polyurethane*, 2008.
- 161 J. M. S. Fonseca, R. Dohrn, A. Wolf and R. Bachmann, *Fluid Phase Equilib.*, 2012, **318**, 83–88.
- 162 T. W. Coffindaffer, I. P. Rothwell and J. C. Huffman, *Inorg. Chem.*, 1983, **22**, 2906–2910.
- 163 J. Reese, K. McDaniel, R. Lenahan, R. Gastinger and M. Morrison, in *IMPACT™ Technology A Greener Polyether Process*.
- 164 J. Pazos and E. Browne, in *Equivalent Weight in the Polymerization of Alkylene Oxides by Double Metal Cyanide Catalysts*, 2008, pp. 434–435.
- 165 M. Pohl, E. Danieli, M. Leven, W. Leitner, B. Blümich and T. E. Müller, *Macromolecules*, 2016, **49**, 8995–9003.
- 166 J. K. Varghese, A. Cyriac and B. Y. Lee, *Polyhedron*, 2012, **32**, 90–95.
- 167 N. Almora-Barrios, S. Pogodin, L. Bellarosa, M. García-Melchor, G. Revilla-López, M. García-Ratés, A. B. Vázquez-García, P. Hernández-Ariznavarreta and N. López,

- ChemCatChem*, 2015, **7**, 928–935.
- 168 T. G. Fox and P. J. Flory, *J. Appl. Phys.*, 1950, **21**, 581–591.
- 169 X. L. Lu, Q. Zhu and Y. Z. Meng, *Polym. Degrad. Stab.*, 2005, **89**, 282–288.
- 170 S. Wang, Y. Huang and G. Cong, *Chin. J. Appl. Chem.*, 1995, **12**, 96–98.
- 171 X. H. Li, Y. Z. Meng, G. Q. Chen and R. K. Y. Li, *J. Appl. Polym. Sci.*, 2004, **94**, 711–716.
- 172 M. Yao, H. Deng, F. Mai, K. Wang, Q. Zhang, F. Chen and Q. Fu, *Express Polym. Lett.*, 2011, **5**, 937–949.
- 173 D. Wu, W. Li, Y. Zhao, Y. Deng, H. Zhang, H. Zhang and L. Dong, *Chinese J. Polym. Sci.*, 2015, **33**, 444–455.
- 174 Y. Hao, H. Yang, G. Zhang, H. Zhang, G. Gao and L. Dong, *Chinese J. Polym. Sci.*, 2015, **33**, 1702–1712.
- 175 Z. Wang, M. Zhang, Z. Liu, S. Zhang, Z. Cao, W. Yang and M. Yang, *J. Appl. Polym. Sci.*, 2017, **46009**, 46009.
- 176 T. A. Osswald, *Polymer processing fundamentals*, Munich, 1998.
- 177 M. L. Williams, R. F. Landel and J. D. Ferry, *J. Am. Chem. Soc.*, 1955, **77**, 3701–3707.
- 178 P. Lomellini and A. G. Rossi, *Die Makromol. Chemie*, 1990, **191**, 1729–1737.
- 179 L. J. Fetters, D. J. Lohse, S. T. Milner and W. W. Graessley, *Macromolecules*, 1999, **32**, 6847–6851.
- 180 R. W. Rendell, K. L. Ngai and G. B. McKenna, *Macromolecules*, 1987, **20**, 2250–2256.
- 181 W. W. Graessley, *Adv. Polym. Sci.*, 1974, **16**, 1–179.
- 182 G. C. Berry and T. G. Fox, *Adv. Polym. Sci.*, 1968, **5**, 261–357.
- 183 M. Doi and S. F. Edwards, *J. Chem. Soc., Faraday Trans. 2*, 1978, **74**, 1789–1801.
- 184 M. Doi, *J. Polym. Sci. Polym. Lett. Ed.*, 1981, **19**, 265–273.
- 185 M. Doi, *J. Polym. Sci. Polym. Phys. Ed.*, 1983, **21**, 667–684.
- 186 W. Friesenbichler, I. Duretek, J. RAJGANESH and S. R. KUMAR, *Polimery*, 2011, **56**, 58–62.
- 187 R. H. Ewoldt, Dissertation, *Nonlinear viscoelastic materials: bioinspired applications and new characterization measures*, Massachusetts Institute of Technology, 2009.
- 188 J. M. Dealy and K. F. Wissbrun, *Melt Rheology and Its Role in Plastics Processing: Theory and Applications*, Van Nostrand Reinhold, New York, 1990.
- 189 E. Helfand and D. S. Pearson, *J. Polym. Sci. Polym. Phys. Ed.*, 1982, **20**, 1249–1258.
- 190 D. S. Pearson and W. E. Rochefort, *J. Polym. Sci. Polym. Phys. Ed.*, 1982, **20**, 83–98.

- 191 M. A. Cziep, M. Abbasi, M. Heck, L. Arens and M. Wilhelm, *Macromolecules*, 2016, **49**, 3566–3579.
- 192 R. H. Ewoldt, P. Winter, J. Maxey and G. H. McKinley, *Rheol. Acta*, 2010, **49**, 191–212.
- 193 M. R. Kember, A. Buchard and C. K. Williams, *Chem. Commun.*, 2011, **47**, 141–163.
- 194 C. Maeda, Y. Miyazaki and T. Ema, *Catal. Sci. Technol.*, 2014, **4**, 1482–1497.
- 195 G. Trott, P. K. Saini and C. K. Williams, *Philos. Trans. R. Soc. A Math. Phys. Eng. Sci.*, 2016, **374**, 20150085.
- 196 C. M. Kozak, K. Ambrose and T. S. Anderson, *Coord. Chem. Rev.*, 2018, **376**, 565–587.
- 197 D. J. Darensbourg and D. R. Billodeaux, *Comptes Rendus Chim.*, 2004, **7**, 755–761.
- 198 I. Shibata, I. Mitani, A. Imakuni and A. Baba, *Tetrahedron Lett.*, 2011, **52**, 721–723.
- 199 L. Xu, M.-K. Zhai, X.-C. Lu and H.-B. Du, *Dalt. Trans.*, 2016, **45**, 18730–18736.
- 200 Y.-H. Li, S.-L. Wang, Y.-C. Su, B.-T. Ko, C.-Y. Tsai and C.-H. Lin, *Dalt. Trans.*, 2018, **47**, 9474–9481.
- 201 A. Thevenon, A. Cyriac, D. Myers, A. J. P. White, C. B. Durr and C. K. Williams, *J. Am. Chem. Soc.*, 2018, **140**, 6893–6903.
- 202 T. Ebrahimi, D. C. Aluthge, B. O. Patrick, S. G. Hatzikiriakos and P. Mehrkhodavandi, *ACS Catal.*, 2017, **7**, 6413–6418.
- 203 Y.-S. Yang, S.-W. Wang and Y. Long, *Curr. Org. Chem.*, 2016, **20**, 2865–2880.
- 204 A. F. Douglas, B. O. Patrick and P. Mehrkhodavandi, *Angew. Chemie - Int. Ed.*, 2008, **47**, 2290–2293.
- 205 I. Yu, A. Acosta-Ramírez and P. Mehrkhodavandi, *J. Am. Chem. Soc.*, 2012, **134**, 12758–12773.
- 206 K. M. Osten, D. C. Aluthge, B. O. Patrick and P. Mehrkhodavandi, *Inorg. Chem.*, 2014, **53**, 9897–9906.
- 207 K. M. Osten, D. C. Aluthge and P. Mehrkhodavandi, *Dalt. Trans.*, 2015, **44**, 6126–6139.
- 208 D. C. Aluthge, C. Xu, N. Othman, N. Noroozi, S. G. Hatzikiriakos and P. Mehrkhodavandi, *Macromolecules*, 2013, **46**, 3965–3974.
- 209 I. Yu, T. Ebrahimi, S. G. Hatzikiriakos and P. Mehrkhodavandi, *Dalt. Trans.*, 2015, **44**, 14248–14254.
- 210 D. C. Aluthge, B. O. Patrick and P. Mehrkhodavandi, *Chem. Commun.*, 2013, **49**, 4295–4297.
- 211 A. B. Kremer, K. M. Osten, I. Yu, T. Ebrahimi, D. C. Aluthge and P. Mehrkhodavandi, *Inorg. Chem.*, 2016, **55**, 5365–5374.

- 212 A. Decortes, M. Martínez Belmonte, J. Benet-Buchholz and A. W. Kleij, *Chem. Commun. (Camb.)*, 2010, **46**, 4580–4582.
- 213 D. J. Darensbourg and R. M. Mackiewicz, *J. Am. Chem. Soc.*, 2005, **127**, 14026–14038.
- 214 K.-J. Kurth, Research report, *Darstellung und Charakterisierung von Dimetallcyanid-Katalysatoren für die Herstellung von Propylenoxid-basierten Polymeren*, University of Hamburg, 2014.
- 215 G. Luinstra, B. Nörnberg, *Process for preparing double metal cyanide catalysts and their use in polymerization reactions*, WO 2016/202838, 2016.
- 216 J. Sebastian and D. Srinivas, *Chem. Commun.*, 2011, **47**, 10449–10451.
- 217 Y. J. Huang, G. R. Qi and G. X. Chen, *Chinese J. Polym. Sci.*, 2002, **20**, 453–459.
- 218 I. Kim, M. J. Yi, K. J. Lee, D. W. Park, B. U. Kim and C. S. Ha, *Catal. Today*, 2006, **111**, 292–296.
- 219 Z. Guo, Q. Lin, X. Wang, C. Yu, J. Zhao, Y. Shao and T. Peng, *Mater. Lett.*, 2014, **124**, 184–187.
- 220 J. Shi, Z. Shi, H. Yan, X. Wang, X. Zhang, Q. Lin and L. Zhu, *RSC Adv.*, 2018, **8**, 6565–6571.
- 221 Z. Hua, G. Qi and S. Chen, *J. Appl. Polym. Sci.*, 2004, **93**, 1788–1792.
- 222 H. S. Suh, J. Y. Ha, J. H. Yoon, C. S. Ha, H. Suh and I. Kim, *React. Funct. Polym.*, 2010, **70**, 288–293.
- 223 M. A. Subhani, B. Köhler, C. Gürtler, W. Leitner and T. E. Müller, *Angew. Chemie Int. Ed.*, 2016, **55**, 5591–5596.
- 224 J. Hayes, L. Langsdorf, B. Isaacs, F. Armellini, *Process for rapid activation of double metal cyanide catalysts*, US 5,844,070, 1998.
- 225 J. O'Connor, D. Lickei, R. Grieve, *Preparing polyether polyols with DMC catalysts*, US 6,359,101, 2002.
- 226 Q. Meng, R. Cheng, J. Li, T. Wang and B. Liu, *J. CO2 Util.*, 2016, **16**, 86–96.
- 227 J. Kuyper and G. Boxhoorn, *J. Catal.*, 1987, **105**, 163–174.
- 228 Y. J. Huang, G. R. Qi and L. S. Chen, *Appl. Catal. A Gen.*, 2003, **240**, 263–271.
- 229 I. Kim, J. T. Ahn, C. S. Ha, C. S. Yang and I. Park, *Polymer (Guildf.)*, 2003, **44**, 3417–3428.
- 230 I. Kim, S. H. Byun and C. S. Ha, *J. Polym. Sci. Part A Polym. Chem.*, 2005, **43**, 4393–4404.
- 231 X.-H. Zhang, Z.-J. Hua, S. Chen, F. Liu, X.-K. Sun and G.-R. Qi, *Appl. Catal. A Gen.*, 2007, **325**, 91–98.
- 232 W. Zhang, L. Lu, Y. Cheng, N. Xu, L. Pan, Q. Lin and Y. Wang, *Green Chem.*, 2011, **13**, 2701–2703.
















- 233 J. Sebastian and D. Srinivas, *Appl. Catal. A Gen.*, 2014, **482**, 300–308.
- 234 M. Zhang, Y. Yang and L. Chen, *Chinese J. Catal.*, 2015, **36**, 1304–1311.
- 235 S. Chen, Q. I. Guo-Rong, Z. J. Hua and H. Q. Yan, *J. Polym. Sci. Part A Polym. Chem.*, 2004, **42**, 5284–5291.
- 236 I. Kim, K. Anas, S. Lee, C. S. Ha and D. W. Park, *Catal. Today*, 2008, **131**, 541–547.
- 237 Y.-J. Huang, X.-H. Zhang, Z.-J. Hua, S.-L. Chen and G.-R. Qi, *Macromol. Chem. Phys.*, 2010, **211**, 1229–1237.
- 238 S. J. Yu, Y. Liu, S. J. Byeon, D. W. Park and I. Kim, *Catal. Today*, 2014, **232**, 75–81.
- 239 J. Sebastian and D. Srinivas, *Appl. Catal. A Gen.*, 2013, **464–465**, 51–60.
- 240 B. Le-Khac, *Improved double metal cyanide complex catalsts*, EP0654302, 1995.
- 241 V. Salerno, E. Landi and M. Vacatello, *Thermochim. Acta*, 1977, **20**, 407–415.
- 242 S. Schilling, H. Doerge, L. Hanusa, *Amine-initiated polyether polyols and a process for their production*, US 5786405, 1998.
- 243 S.-F. Stahl, Dissertation in preparation, University of Hamburg.
- 244 Y. Dong, X. Wang, X. Zhao and F. Wang, *J. Polym. Sci. Part A Polym. Chem.*, 2012, **50**, 362–370.
- 245 N. J. Robertson, Z. Qin, G. C. Dallinger, E. B. Lobkovsky, S. Lee and G. W. Coates, *Dalt. Trans.*, 2006, 5390–5395.
- 246 I. Kim, M. J. Yi, S. H. Byun, D. W. Park, B. U. Kim and C. S. Ha, *Macromol. Symp.*, 2005, **224**, 181–191.
- 247 D.-J. Liaw and P.-S. Chen, *J. Polym. Sci. Part A Polym. Chem.*, 1996, **34**, 885–891.
- 248 D. Liaw and W. Shen, *Angew. Makromol. Chemie*, 1992, **199**, 171–190.
- 249 L. Luo, Y. Meng, T. Qiu and X. Li, *J. Appl. Polym. Sci.*, 2013, **130**, 1064–1073.
- 250 G. Labourdette, D. J. Lee, B. O. Patrick, M. B. Ezhova and P. Mehrkhodavandi, *Organometallics*, 2009, **28**, 1309–1319.
- 251 A. Acosta-Ramírez, A. F. Douglas, I. Yu, B. O. Patrick, P. L. Diaconescu and P. Mehrkhodavandi, *Inorg. Chem.*, 2010, **49**, 5444–5452.
- 252 S. M. Kirk, G. Kociok-Köhn and M. D. Jones, *Organometallics*, 2016, **35**, 3837–3843.
- 253 K. Yasuda, R. C. Armstrong and R. E. Cohen, *Rheol. Acta*, 1981, **20**, 163–178.

APPENDIX








































A1 Hazardous materials

All hazardous waste was disposed in compliance with legal requirements. Table A.1 displays all utilized chemicals and the corresponding hazard and precautionary statements.

Table A.1 Utilized chemicals and corresponding hazard and precautionary statements.

Substance	Hazard pictograms	Hazard statements	state-	Precautionary Statements
Acetic acid		226-314		210-260-280-303+361+353-305+351+338-370+378
Acetone		225-319-336		210-305+351+338-370+378-403+235
Acetonitrile		225-302+312+332-319		210-280-305+351+338
Bisphenol A		317-318-335-361f-411		280-305+351+338+310
Bisphenol AF		315-319-335		261-305+351+338
Bisphenol S	-	-		-
Bis(triphenylphosphine)iminium chloride		315-319-332-335		261-305+351+338
Calcium hydride		260		223-231+232-370+378
Carbon dioxide		280		403
Cyclohexene oxide		226-302-311+331-314		261-280-305+351+338-310
Dichloromethane		315-319-335-336-351-371		260-280-305+351+338
Diethyl ether		224-302-336		210-261
Di-tert-butyl dicarbonate		226-315-317-318-330-335		210-260-280-304+340+310-305+351+338+310-370+378
2,4-Di-tert-butyl-phenol		315-318-410		280-305+351+338+310
Dodecylamine		304-314-335-373-410		261-273-280-301+310-305+351+338-310
Ethanol		225-319		210-305+351+338-370 +378-403+235

Appendix

Ethylene carbonate	 	302-319-373	260-301+312+330-305+ 351+338
Formaldehyde (aq.)	  	301+311+331-314-317-335-341	201-280-303+361+353-304+340+310-305+351+338-308+311
Glutaric acid		319	305+351+338
Hexane	   	225-304-315-336-361f-373-411	201-210-273-301+310-308+313-331
Hexadecylamine	 	314-400	273-280-305+351+338-310
Hydrochloric acid (aq.)	 	290-314-335	260-280-303+361+353-304+340+310-305+351+338+310
2-Hydroxybenzaldehyde	  	302-315-319-341-411	201-273-305+351+338-308+313-391-501
4-Hydroxybenzaldehyde	-	-	-
Indium(III) bromide		315-319-335	261-305+351+338
Indium(III) chloride	 	302-314	280-305+351+338-310
Indium(III) iodide	 	317-361	280
Magnesium chloride	-	-	-
Magnesium sulfate	-	-	-
Methanol	  	225-301+311+331-370	210-280-302+352+312-304+340+312-370+ 378-403+235
Octadecylamine	  	304-315-318-373-410	273-280-301+310-305+351+338-310-331-501
Paraformaldehyde	   	228-302+332-315-317-318-335-351	210-261-280-301+312+330-305+351+338-310-370+378
Phenol	   	301+311+331-314-341-373-411	201-261-280-301+310+330-303+361+353-305+351+338
2-Phenoxyethanol		302-319	301+312+330-305+351+338
Potassium <i>tert</i> -butoxide	 	228-260-314	210-231+232-280-305+351+338-370+378-402+404

Appendix

Propylene carbonate		319	305+351+338
Propylene oxide		224-302+312-315-319-331-335-340-350	201-210-280-308+313-370+378-403+235
Sodium carbonate		319	305+351+338
Sodium cyanoborohydride		228-300+310+330-314-410	210-280-303+361+353-304+340+310-305+351+338
Sodium ethoxide		228-251-314	210-235+410-280-303+361+353-304+340+310-305+351+338
Sodium hydroxide (aq.)		290-314	280-301+330+331-305+351+338-308+310
Tetradecylamine		315-319-335-400	261-273-305+351+338
Tetrahydrofurane		225-302-319-335-351	210-280-301+312+330-305+351+338-370+378-403+235
Toluene		225-304-315-336-361d-373	210-260-280-301+310-370+378-403+235
4-Toluenesulfonic acid		290-314-335	260-280-303+361+353-304+340+310-305+351+338
Triethylamine		225-302-311+331-314-335	210-261-280-303+361+353-305+351+338-370+378
Zinc nitrate hexahydrate		272-302-315-319-335	220-261-305+351+338

A2 Utilized CMR chemicals

Table A.2 displays all utilized CMR chemicals and the number of experiments.

Table A.2 Utilized CMR chemicals and number of experiments.

CAS-Nr	Compound name and Cat.	Procedure and utilized amount	Nr of experiments
75-56-9	1,2-Epoxypropane (1B)	Polymerization, 40 L	375
106-89-8	1-Chloro-2,3-epoxypropane (1B)	Polymerization, 0.5 L	10
106-91-2	2,3-Epoxy methacrylate (1B)	Polymerization, 0.5 L	10
50-00-0	Formaldehyde (1B)	Synthesis, 0.05 L	3

A3 Statutory Declaration

I hereby declare on oath, that the present thesis was written by me and that I used no source, materials and aids other than those I stipulated. I assure, that this thesis was not submitted for a previous doctorate examination procedure.

Bergisch Gladbach, 11.01.2020

A4 Declaration of my share in the included publications

J. Marbach, B. Nörnberg, A. F. Rahlf and G. A. Luinstra, *Zinc glutarate-mediated copolymerization of CO₂ and PO – parameter studies using design of experiments*, Catal. Sci. Technol., **2017**, 7, 2897 – 2905.

I declare that I am the first author of this publication. I had the main responsibility for the design and realization of the research project. This included the determination of the objectives, planning of the experiments, the evaluation of the analyses, the interpretation of the results and the writing of the manuscript (Total share: **80 %**).

J. Marbach, Th. Höfer, N. Bornholdt, G. A. Luinstra, *Catalytic Chain Transfer Copolymerization of Propylene Oxide and CO₂ using Zinc Glutarate Catalyst*, ChemistryOpen, **2019**, 8, 1-13.

I declare that I am the first author of this publication. I had the main responsibility for the design and realization of the research project. This included the determination of the objectives, planning of the experiments, the evaluation of the analyses, the interpretation of the results and the writing of the manuscript (Total share: **75 %**).